Universitat
de les Illes Balears

DOCTORAL THESIS
2021

3D NUMERICAL SIMULATIONS OF OSCILLATIONS IN SOLAR PROMINENCES AND GRAVITATIONAL INSTABILITY IN THREADS

Andrés Adrover González

Universitat
de les Illes Balears

DOCTORAL THESIS
2021

Doctoral Programme of Physics

3D NUMERICAL SIMULATIONS OF OSCILLATIONS IN SOLAR PROMINENCES AND GRAVITATIONAL INSTABILITY IN THREADS

Andrés Adrover González

Thesis supervisor: Jaume Terradas Calafell
Thesis tutor: Alicia Magdalena Sintes Olives

Doctor by the Universitat de les Illes Balears

Universitat de les Illes Balears

El Dr. Jaume Terradas Calafell, de la Universitat de les Illes Balears

DECLARA:

Que la tesi doctoral que porta per títol '3D numerical simulations of oscillations in solar prominences and gravitational instabilities in threads', presentada per Andrés Adrover González per a l'obtenció del títol de doctor, ha estat dirigida sota la meva supervisió.

I perquè quedi constància d'això signo aquest document.

Signatura,

Director: Jaume Terradas Calafell

Doctorand: Andrés Adrover González

Palma de Mallorca.

Als meus pares i germans

Table of contents

Summary

Solar promineces are plasma structures that can raise up to 100 Mm above the solar surface. Prominences are about 100-fold denser and cooler than the surrounding solar corona and they are seen as bright cloud-like structures beyond the solar limb or as dark filamentous bodies laying on the solar disk. To be suspended in the tenuous corona, prominences are supported against the gravity force mainly by magnetic fields. Over the years, these spectacular structures have awaken the curiosity of many observers and theorists who carried out a tremendous progress in understanding the highly dynamic nature of prominences. However, several outstanding issues still require an answer.

In this Thesis we focus our attention on the study of oscillations in solar prominences and on the investigation of their gravitational stability. For example, a full understanding of the mechanisms that drive the oscillations and their attenuation has not been reached yet. In this Thesis we propose a completely new analysis in the stability of dense plasma based on the balance between pressure gradients and gravity force.

By means of numerical simulations we carried out a study of vertical, transverse and longitudinal oscillations by solving the ideal magnetohydrodynamic (MHD) equations for a wide range of parameters. We studied the periodicity and attenuation of the induced oscillations for a curtain-shaped model of a prominence permeated by an unsheared magnetic arcade with dips. It is shown that longitudinal oscillations can be fit with the pendulum model, whose restoring force is the field-aligned component of gravity, but other mechanisms such as pressure gradients may contribute to the movement. On the other hand, transverse oscillations are mostly subject to magnetic forces. The attenuation of transverse oscillations was investigated by analysing the velocity distribution and computing the Alfvén continuum modes. We conclude that resonant absorption is the main cause. Damping of longitudinal oscillations is due to some kind of shear numerical viscosity.

We extended the simulations of our initial prominence model by including a strong shear in the magnetic arcade. The redistribution of the magnetic dips due to shear makes the prominence unstable to displacements along the magnetic field lines. We investigated other types of magnetic structures but we found that might be unstable. For this reason, we decided to investigate the gravitational instability of prominences using a basic model.

We analysed the stability of individual plasma threads in a very simple configuration. First, we considered a circular magnetic flux tube where no magnetic dips exist and only gas pressure gradient provides the restoring force against gravity. We derived analytical expressions for the different feasible equilibria and the corresponding frequencies of oscillation. It is

found that prominences may have diverse stable or unstable equilibrium states subject to the initial position of the thread, its density contrast and length, and the total length of the magnetic field lines. The transition between the two types of solutions is produced at specific bifurcation points that have been determined analytically in some particular cases.

Finally, the effect of magnetic dips at the curved magnetic structure is incorporated into the analytical expressions. In a well formed prominence where the cold plasma is hosted by the magnetic dip, the system develops a stable solution at the bottom of the dip plus two pairs of stable/unstable fixed points at the lateral edges of the tube. In this sense, two qualitative different stable states coexist, namely the central solution, stable to relatively small perturbations, and the most external lateral fixed points. On the other hand, prominences initially located around short and shallow dips develop a central unstable equilibrium point that makes the prominence to fall down when it is laterally displaced.

Resum

Les protuberàncies solars són estructures de plasma que s'enlairen fins a uns 100 Mm sobre la superfície del Sol. Les protuberàncies són 100 vegades més denses i fredes que la corona solar que les envolta i s'observen sobre el limbe com a estructures brillants en forma de núvol o sobre el disc solar com a cossos obscurs filamentosos. Per mantenir-se suspeses a la tènue corona, les protuberàncies se sostenen sobretot pels camps magnètics que contraresten la força de la gravetat. Al llarg dels anys, aquestes espectaculars estructures han despertat la curiositat de molts observadors i teòrics que han portat a terme un enorme avanç en la comprensió de la natura altament dinàmica de les protuberàncies. Emperò, diverses qüestions segueixen pendents de resposta.

En aquesta Tesi centram la nostra atenció en l'estudi de les oscil·lacions en protuberàncies solars i en la investigació de la seva estabilitat gravitatòria. Per exemple, encara no s'ha arribat a una comprensió completa dels mecanismes que impulsen les oscil·lacions i la seva atenuació. En aquesta tesi suggerim una anàlisi completament nova de l'estabilitat dels plasmes densos basada en el balanç entre els gradients de pressió i la força de la gravetat.

Mitjançant simulacions numèriques realitzam un estudi d'oscil·lacions verticals, transversals i longitudinals resolent les equacions ideals de la magnetohidrodinàmica (MHD) per un ampli rang de paràmetres. Estudiam la periodicitat i l'atenuació de les oscil·lacions induïdes per un model de protuberància en forma de cortina en un camp magnètic en forma d'arcada sense cisalla i amb depressió magnètica. Es mostra que les oscil·lacions longitudinals s'ajusten al model de pèndol, la força restauradora del qual és la força de la gravetat projectada sobre la línia de camp, maldament altres mecanismes com per exemple gradients de pressió poden contribuir en el moviment. D'altra banda, les oscil·lacions transversals estan sotmeses principalment a forces magnètiques. L'esmorteïment de les oscil·lacions transversal s'investiga per mitjà de l'anàlisi de la distribució de velocitats i del càlcul dels modes continus d'Alfvén. S'arriba a la conclusió de què l'absorció ressonant és la principal causa. L'esmorteïment de les oscil·lacions longitudinals es deu a algun tipus de viscositat numèrica per cisalla.

Les simulacions per al nostre model de protuberància s'estén amb la incorporació d'una forta cisalla a l'arcada magnètica. La redistribució de les depressions magnètiques deguda a la cisalla fa que la protuberància sigui inestable a desplaçaments al llarg de les línies de camp magnètic. Investigàrem altres tipus d'estructures magnètiques, però trobàrem que podien esser inestables. Per aquest motiu, es va decidir investigar la inestabilitat gravitatòria de les protuberàncies per un model senzill.

Analitzam la inestabilitat per a fils individuals de plasma en una configuració molt simplificada. Primer es considera un tub de flux magnètic circular sense depressió magnètica de manera que només el gradient de pressió exerceix de força restauradora contra la gravetat. Es deriven expressions analítiques per a diferents possibles equilibris i les seves corresponents freqüències d'oscil·lació. Es troba que les protuberàncies poden tenir diversos equilibris estables o inestables sotmesos a la posició inicial del fil, la seva densitat i longitud i a la longitud total de la línia de camp magnètic. La transició entre els dos tipus de solucions es produeix en els punts de bifurcació que es determinen analíticament per alguns casos en particular.

Finalment, l'efecte de les depressions magnètiques en l'estructura magnètica corba s'incorpora a les expressions analítiques. Per a una protuberància ben formada on el plasma fred s'allotja

en la depressió magnètica, el sistema desenvolupa una solució estable a la part inferior de la depressió, més dos parells de punts fixos estables i inestables en els caires laterals del tub. Amb aquest sentit, dos estats estables qualitativament diferents coexisteixen, específicament la solució del centre, estable per pertorbacions relativament petites, i els punts fixos més externs dels laterals. Altrament, les protuberàncies inicialment col·locades al voltant de depressions curtes i poc profundes desenvolupen un punt d'equilibri central inestable que fa que la protuberància caigui quan es desplaça lateralment.

Resumen

Las protuberancias solares son estructuras de plasma que se elevan hasta unos 100 Mm sobre la superficie del Sol. Las protuberancias son 100 veces más densas y frías que la corona solar que las rodea y se observan sobre el limbo del Sol como estructuras brillantes en forma de nube o sobre el disco solar como cuerpos oscuros filamentosos. Para mantenerse suspendidas en la tenue corona, las protuberancias se sostienen mayormente por los campos magnéticos que contrarrestan la fuerza de la gravedad. A lo largo de los años, estas espectaculares estructuras han despertado la curiosidad de de muchos observadores y teóricos que han llevado a cabo un enorme avance en la comprensión de naturaleza altamente dinámica de las protuberancias. Sin embargo, varias cuestiones pendientes aún requieren una respuesta.

En esta Tesis centramos nuestra atención en el estudio de oscilaciones en protuberancias solares y en la investigación de su estabilidad gravitatoria. Por ejemplo, aún no se ha alcanzado una comprensión completa de los mecanismos que impulsan las oscilaciones y su atenuación. Por otro lado, en esta Tesis proponemos un análisis completamente nuevo de la estabilidad de los plasmas densos basado en el balance entre los gradiente de presión y la fuerza de la gravedad.

Mediante simulaciones numéricas realizamos un estudio de oscilaciones verticales, transversales y longitudinales resolviendo las ecuaciones ideales de la magnetohidrodinámica (MHD) para un amplio rango de parámetros. Estudiamos la periodicidad y atenuación de las oscilaciones provocadas para un modelo de protuberancia en forma de cortina en un campo magnético en forma de arco sin cizalladura y con depresión magnética. Se muestra que las oscilaciones longitudinales se ajustan al modelo de péndulo, cuya fuerza restauradora es la fuerza de la gravedad proyectada sobre la líneas de campo, aunque otros mecanismos como por ejemplo gradientes de presión pueden contribuir al movimiento. Por otro lado, las oscilaciones transversales están sujetas principalmente a fuerzas magnéticas. La atenuación de las oscilaciones transversales se investiga mediante el análisis de la distribución de velocidades y el cálculo de los modos continuos de Alfvén. Se llega a la conclusión de que la absorción resonante es la principal causa. La atenuación de las oscilaciones longitudinales se debe a algún tipo de viscosidad numérica por cizalladura.

Las simulaciones para nuestro modelo de protuberancia se extienden con la incorporación de una fuerte cizalladura en la arcada magnética. La redistribución de las depresiones magnéticas debida a la cizalladura hace que la protuberancia sea inestable para desplazamientos a lo largo de las líneas de campo magnético. Investigamos otros tipos de estructuras magnéticas, pero se encontró que podían ser inestables. Por este motivo, se decidió investigar la inestabilidad gravitatoria de las protuberancias para un modelo sencillo.

Analizamos la inestabilidad para hilos individuales de plasma en una configuración muy simplificada. Primero se considera un tubo de flujo magnético circular sin depresión magnética de modo que sólo el gradiente de presión ejerce de fuerza restauradora contra la gravedad. Se derivan expresiones analíticas para los diferentes posibles equilibrios y sus correspondientes frecuencias de oscilación. Se encuentra que las protuberancias pueden tener diversos equilibrios estables o inestables sujetos a la posición inicial del hilo, su densidad y longitud y a la longitud total de las líneas de campo magnético. La transición entre los dos tipos de soluciones se produce en los puntos de bifurcación que se determinan analíticamente para

algunos casos en particular.

Finalmente, el efecto de las depresiones magnéticas en la estructura magnética curva se incorpora a las expresiones analíticas. Para una protuberancia bien formada donde el plasma frío se aloja en la depresión magnética, el sistema desarrolla una solución estable en la parte inferior de la depresión, más dos pares de puntos fijos estables e inestables en los bordes laterales del tubo. En este sentido, dos estados estables cualitativamente diferentes coexisten, específicamente la solución del centro, estable para perturbaciones relativamente pequeñas, y los puntos fijos más externos de los laterales. Por otro lado, las protuberancias inicialmente colocadas alrededor de depresiones cortas y poco profundas desarrollan un punto de equilibrio central inestable que hace que la protuberancia caiga cuando se desplaza lateralmente.

Acknowledgments

The present Thesis is the result of almost five years of work and it would not have been possible without the support of quite a large number of people.

First of all, I would like to especially thank my supervisor Dr. Jaume Terradas Calafell for his constant and continuous guidance, support and patience. His extensive knowledge in the field of solar physics has been essential for the development of this Thesis. I wish to show my gratitude to Isabell Piantschitsch for her admirable assistance, I am indebted to her. I would also like to thank my tutor, Dr. Alicia Sintes for her valuable supervision.

Secondly, I want to express my gratitude to all the members of the Solar Physics Group of the Universitat de les Illes Balears for giving me the possibility to be a member of this friendly fellowship. I wish to thank in particular Jaume Terradas, José Luís Ballester, Ramón Oliver, Marc Carbonell, Roberto Soler, Elie Soubrié, Manuel Luna, Nabil Freij, Isabell Piantschitsch, David Martínez, Sergio Díaz, Matheus Aguiar-Kriginsky, Llorenç Melis, Biel Castell, and Adel Boul'harrak.

I acknowledge the financial support from the Spanish 'Ministerio de Economía, Industria y Competitividad' for the 'Ayuda para contratos predoctorales' grant. I also thank the 'Institute of Applied Computing & Community Code (IAC^3)' for its support.

I welcome this opportunity to thank my friends Ángel Amores, Diego Carrió, David Martínez, Guillermo Olivares, and Sebastià Barceló who have always encouraged me to carry out this rewarding but challenging task. Moreover, I am grateful to my colleagues Belén Martí, Shoukai Xu, Miguel Bezáres, Maria Cardell, Moner Al Chawa, Borja Miñano, Fabio Galán, Hector Estellés, Cecilio García, Daniele Viganò, Francesc Bonnín, María Montes, and many more for their company along these years.

And last but not least, I am eternally grateful to my parents Andreu and Paula, and my siblings Alicia and Sergi, to be part of my life throughout this journey.

List of publications

Andrés Adrover-González and Jaume Terradas; 2020, *3D numerical simulations of oscillations in solar prominences*, Astronomy & Astrophysics, 633, A113.

Andrés Adrover-González, Jaume Terradas, Ramón Oliver, and Marc Carbonell; 2021, *Gravitational instability of solar prominence threads: I. Curved magnetic fields without dips*, Astronomy & Astrophysics, accepted for publication.

Chapter 1

Introduction

1.1 Solar prominences

Solar prominences are impressive plasma structures abounding in the solar atmosphere. They can be observed as bright cloud-like objects above the solar limb (see Figure 1.1) or as dark filament structures on the solar disk. These features consist of dense and cool plasma that is suspended in the solar corona at heights up to 100 Mm above the solar surface. Typically, these plasma clouds are hundred times cooler and denser than the surrounding material, hence, their presence can only be explained by the existence of an external force that counteracts the gravity and provides thermal isolation. This counteracting force is the magnetic force. Thanks to the tremendous improvement of observation techniques as well as the development of theoretical models and numerical simulations, comprehensive knowledge regarding the physics of solar prominences has been generated. However, there are still several open issues that deserve to be addressed.

1.1.1 Historical background

The first systematic observations of solar prominences date back to the second half of the 19th century (see Tandberg-Hanssen 1995). Even much earlier than that, some observations had reported the rare occurrences of total solar eclipses. The first description of a prominence seems to have been made by Muratori during the eclipse of 1239 (see Secchi 1875; Bhatnagar & Livingston 2005) in which he described a 'burning hole' in the corona. In the 18th century only a few events were studied by Vassenius in 1733 and by Ulloa in 1778, but here the observed figures were described as clouds or holes on the Moon.

The speculative observations stopped during the eclipse of 1860 with the emergence of photography and since that time, prominences have been identified as solar features. Photography helped to classify the morphology, the distribution, and the motion of prominences in different categories. A second important advance in the study of prominences was the development of spectroscopy which allowed the analysis of the composition of these structures. Important parameters such as the temperature or the density can be derived from spectroscopic data. This new observation technique was introduced for the first time during the eclipse of 1868 and it entailed the discovery of a new element never observed on

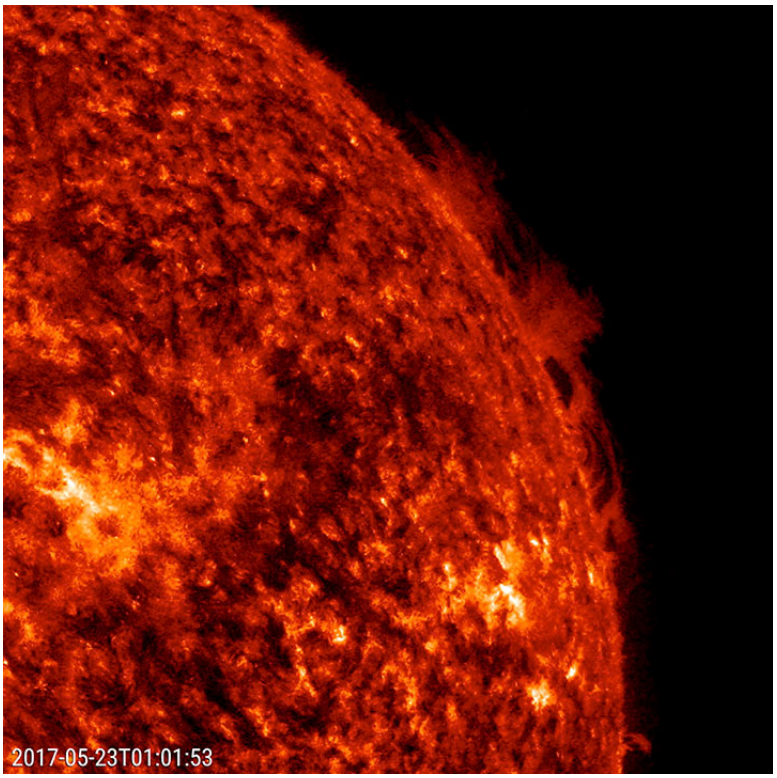

Figure 1.1: A solar hedgerow prominence at the sun's edge. Credit: Solar Dynamics Observatory, NASA.

Earth, namely Helium (Lockyer 1868). Spectroscopy also made it possible to observe the Sun without eclipses (Janssen 1869), and therefore allowed more regular observations. Observers could identify motions and eruptions of prominences and even their threaded fine structure, or the correlation between the number of prominences with the solar activity or sunspots. However, all those studies were made in prominences located above the solar limb. With the invention of the spectroheliograph in 1890 it was possible to study the solar corona on the disk in particular spectral lines (H_α line of hydrogen at 6563 Å or the K lines of ionised calcium). Since then, the bright features observed in emission at the solar limb, called filaments, can be seen in absorption as dark structures on the solar disk. Prominences and filaments denote the same phenomenon and both terms are used interchangeably. The observation of dark filaments as a function of latitude provided an accurate proof of the solar differential rotation. Years after, in 1931, the coronagraph was introduced by Bernard Lyot in order to study the whole corona outside of a total eclipse, ignoring the strong emission of the solar disk (Lyot 1930, 1939).

The epoch from 1860 to 1960 was considered by Tandberg-Hanssen (1995) as the spectrograph period, whereas the time after 1960 was described as the polarimetric period. The magnetic character of solar structures such as sunspots, studied for the first time by Hale (1908), anticipated the importance of measurements of the magnetic fields. The starting point of the polarimetric period is the study of Zirin & Severny (1961) who measured the magnetic field of a prominence with a magnetograph derived from the Zeeman splitting effect. When technology allowed regular observations without the use of eclipses, the ground-based

solar optical facilities expanded throughout the Globe. The vast range of locations of solar observatories allow twentyfour hours a day solar tracking, however, their instruments are limited by the atmospheric absorption. Space missions, such as the Solar and Heliospheric Observatory (SOHO) launched on 1995, the Japanese mission HINODE or the Solar Dynamics Observatory (SDO), daily send spectacular high resolution images of the plasma motions or the fine structure of prominences that allow their study (see Vial 2015, for a detailed historical background).

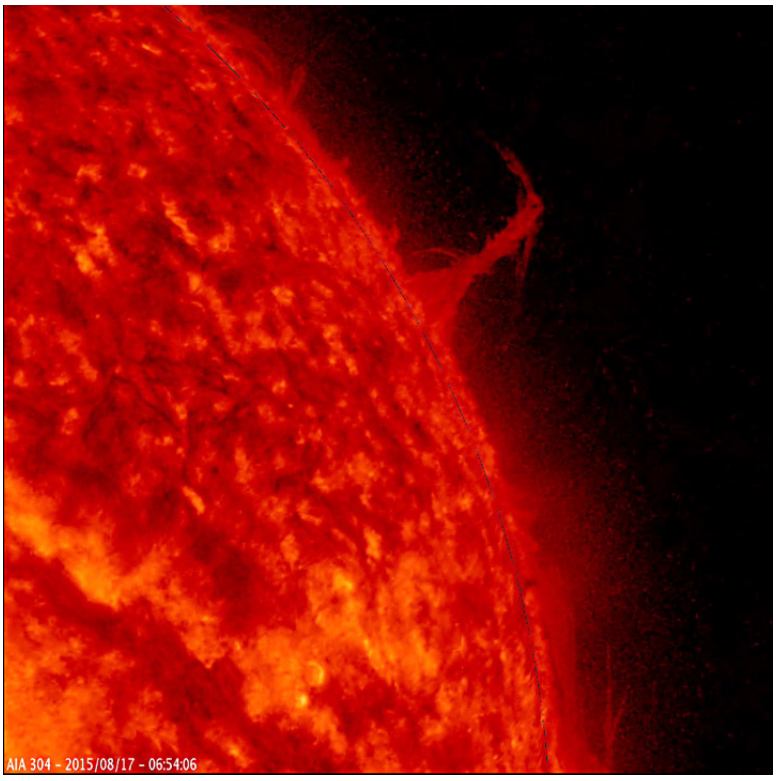

Figure 1.2: Single plume of plasma. Credit: Solar Dynamics Observatory, NASA.

1.1.2 Basic properties of prominences

Observations of solar prominences made over the years have shown their heterogeneous properties. They vary in shape, size, location, lifetime, and dynamics which complicates their categorisation. Moreover, when the observations started being more systematic, it was observed that the number of filaments varied with the solar activity that involves the existence of a connection between prominences and magnetic fields. Some examples of solar prominences are shown in Figures 1.1 and 1.2. Figure 1.1 shows a solar prominence at the Sun's edge. This type of filament is named hedgerow prominence because it looks somewhat like a hedge of bushes. It is characterised by a few points of contact with the surface. Another type of prominence is shown in Figure 1.2. In this case the prominence consists of a single plume. It rises up from the Sun and reaches the size of many Earth diameters. Other types of observed prominences are arch, pillar, or pyramid-shaped plasma structures.

In order to understand the nature of solar prominences, different classifications have been proposed and are still in general use. An extensive pioneering classification was carried out

by Secchi (1875), who divided simple forms from compound forms into different blocks and included detached and eruptive (or short-lived) prominences as a different group. As the observations improved, the connection between prominences and sunspots gained importance (Pettit 1932; Newton 1935). Jones (1958) reviewed the classification of solar prominences made by Menzel & Evans (1953). In their study the motion of the material within the prominences or the relationship with sunspots together with their characteristic form were taken into account.

Nowadays, prominences are in general divided into three different groups: quiescent, active and intermediate prominences. For this organization the magnetic character of the location of the filaments is more important than the shape of the plasma. Since the magnetic field strength turns out to be the dominant force of the prominence environment, it is feasible that the magnetic fields control the prominence structure and dynamics. The first group includes prominences observed in areas distant from strong magnetic fields, known as the quiet Sun (about 10 G), that is typically located at high latitude regions. In their global appearance they are stable structures and have life-times of weeks up to months. Their density ranges between $10^9 - 10^{11}$ cm^{-3} (e.g. Hirayama 1971, 1986; Bommier et al. 1986; Li et al. 1998) and their core temperature lies between 6,000 K to 10,000 K (Stellmacher et al. 2003; Parenti et al. 2005). The dimensions of the filament range from 60 Mm to 600 Mm in length, from 15 Mm to 100 Mm in height and from 5 Mm to 15 Mm in thickness, although these values may vary depending on the author. The main prominence plasma parameters are summarised in Table 1.1. With the aim of providing a statistical analysis, various automated detection procedures, classification, and tracking of solar filaments have been elaborated (Bernasconi et al. 2005; Wang et al. 2010). Active prominences are located in the active regions of the Sun characterised by strong magnetic fields (about 100 G) and adjacent to sunspots. In contrast to quiescent prominences, active filaments are dynamic structures and may last from only minutes to hours. Their temperature and density are higher than those of the quiescent prominences, but they have smaller dimensions (see Priest 1989). The intermediate group is located at the border of active regions, with one end close to the active region and the other one far from there. In Figure 1.3 the three types of filaments are marked by coloured arrows.

Physical parameters		
Electron Density (cm^{-3})	$10^9 - 10^{11}$	Adapted from Labrosse et al. (2010).
Temperature (K)	6,000-10,000	
Gas pressure (dyn cm^{-2})	$\sim 0.02 - 1$	
Hydrogen ionization ratio	$0.2 - 0.9$	
Length (Mm)	60-600	Adapted from Tandberg-Hanssen (1995).
Width (Mm)	5-15	
Height (Mm)	15-100	

Table 1.1: Main prominence plasma parameters in the cool core of quiescent prominences.

The structure of filaments consists of three different components: spine, two extreme ends, and barbs. The spine is the longitudinal axis of the plasma that runs horizontally along the axis of the structure and ends in the extreme legs of the prominence. The spine is clearly

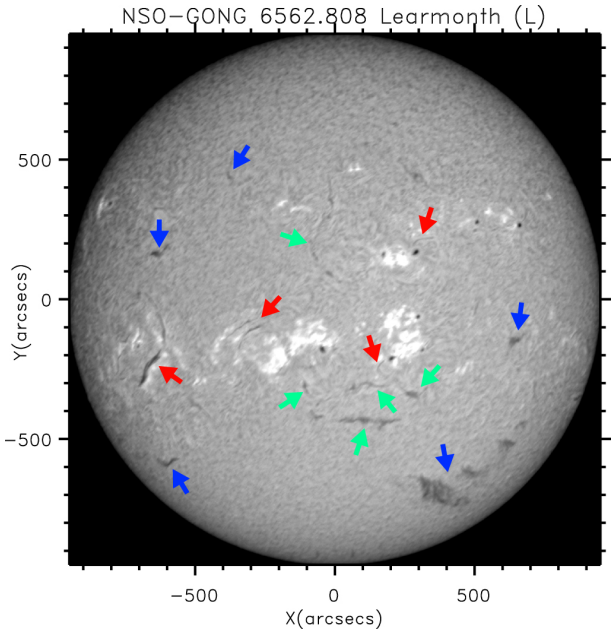

Figure 1.3: Illustration of the three types of filaments, which are seen as dark structures against the bright chromosphere. The red arrows point to active region filaments; the green arrows point to intermediate filaments; and the blue arrows point to quiescent filaments. Adapted from Luna et al. (2018).

discernible when it is seen against the solar disk in absorption, however at the limb it is less conspicuous. The third component are the filament barbs that emerge from the sides of the filament and extend down from the spine to the chromosphere tracing an acute angle with respect to the long axis of the filament. The high resolution observations show that these structures are formed by individual thin thread-like plasma structures that trace the local magnetic field. One can observe fine structures with widths down to the resolution limit (around 0.1 Mm). Prominence threads are dynamic structures and have a lifetime of only a few minutes which is a shorter lifetime than the one of the whole structure. These fine threads can be observed horizontally oriented or as quasi vertical bright threads. Observations show that in these thin threads the plasma flows with velocities of about $10\,\mathrm{km\,s^{-1}}$.

The cool core of prominences joins with the hot corona by means of a very thin interface (of the order of a few hundred km) called prominence-corona transition region (PCTR). This thin layer is characterised by a strong temperature gradient. The optically thin emission of prominence plasma mostly comes from the PCTR (Parenti 2015). This external envelope has been studied in detail through observations of UV-EUV lines. This inhomogeneous layer also plays an important role in the explanation of the damping of transverse prominence oscillations which is resonant absorption (Okamoto et al. 2015; Antolin et al. 2015).

1.1.3 Magnetic structure

Prominences are supported against gravity by the magnetic environment. The structures that provide this magnetic support are the filament channels. This channels are regions in the chromosphere that surround neutral lines which divide extended areas of magnetic

fields of opposite polarity. These lines are called Polarity Inversion Lines (PILs). Filament channels tend to stand in the chromosphere for long periods of time and a sole channel can conceive many successive filaments. In the chromosphere the magnetic field of the filament channel is predominantly horizontal and pointing in the same directions on the two sides of the channel. Moreover, this magnetic field expands into the corona in the form of magnetic arcades that are anchored in the opposite polarity regions on either side of the channel. The magnetic arcades have a strongly sheared magnetic component along the inversion line. The prominence plasma is embedded in this magnetic field. The filament spine does not tend to be aligned with the magnetic component and the angle between both deviates about 25^{o} each other. To counteract the gravity force that pushes the plasma downwards, the z-component of the Lorentz force must be positive, so that the field lines have to describe a concave upwards curvature called magnetic dip. Dips can be created by the weight of prominence plasma that bends the field lines so that the shape of the dipped lines is determined by the balance between magnetic and gravitational forces. Another possibility is that the dips exist in force-free magnetic configurations in absence of prominence plasma. In this second case, the filament plasma is likely to be located near the dips of the field lines.

In the past, various models for prominence magnetic structures have been proposed (See Tandberg-Hanssen 1995; Mackay et al. 2010). The earliest models (Menzel 1951, Dungey 1953 and Kippenhahn and Schluter 1957) obtained solutions for the support of quiescent prominences in a magnetohydrostatic equilibrium. They considered an isothermal gas threaded by a magnetic field described by a flux function and assuming that the magnetic component along the prominence is null. These pioneering studies have been re-investigated by many authors. Malherbe & Priest (1983) obtained a 2D prominence model as a current sheet of finite vertical extension with complex-variable functions which allow a discontinuity of the vertical field component at the location of the prominence. Hood & Anzer (1990) generalised Menzel's model by including a non-isothermal internal structure of the prominence and allowing the third component of the magnetic field that is crucial to obtain the magnetic shear. The models mentioned in the previous paragraph contain normal polarity fields. This means that the apparent polarity of the field across the prominence sheet is the same as the polarity of the underlying photospheric field. On the other hand, many authors have proposed inverse polarity field models. In these cases, the polarity is the opposite as in the underlying photosphere and a neutral point ($B = 0$) is present in the magnetic structure between the photosphere and the filament. The typical inverse polarity model was described by Kuperus & Raadu (1974). This model is characterised by a low pressure corona permeated by a magnetic field whose field lines connect to the photosphere and a filament region where the field lines are closed, taking the form of a magnetic-flux rope. Other examples of inverse polarity models are van Tend & Kuperus (1978), Demoulin & Priest (1993), or Titov & Démoulin (1999).

1.1.4 Other remarks

Several prominence formation processes have been proposed to explain how the prominence plasma rises up to the corona (see Karpen 2015). In the Menzel and Evans prominence classification (1953), they had already distinguished between objects forming from above and objects forming from below. In addition, these models must take observational constraints

into account, such as the enormous range in space and time that prominences cover, their highly dynamic properties and fine structure, or the barbs behaviour. The main models are injection, evaporation-condensation, levitation, and magneto-thermal convection. The models agree on the fact that the mass must come from the chromosphere. In the injection models, the cool plasma is propelled upwards in filament channel flux tubes with sufficient force to reach the observed heights of prominence plasma. Most injection models assert that the force that forces this upward jets is the magnetic reconnection at the feet of the flux tubes in the low atmosphere. In the evaporation-condensation models, localised heating above the flux tube footpoints produces evaporation of the chromospheric plasma, which condenses in the coronal part of the magnetic flux tube (e.g., Luna et al. 2012b). Levitation models propose that cool plasma is lifted by rising magnetic fields at the PIL and transported transverse to the magnetic field. In the magneto-thermal convection, twisted magnetic flux emerges from the solar interior into the chromosphere beneath prominences, forming magnetic bubbles.

1.2 Oscillations in prominences

Solar prominence oscillations have been the subject of a large number of studies and they have been a rich source of information to perform prominence seismology and to understand the theoretical models. Many authors establish the first systematic investigation of prominence oscillations on the basis of the study of Ramsey & Smith (1966). However, as the study itself indicates, filament oscillations had been reported by other authors some years before, for example Dodson (1949), Ohman (1953), or Dodson & Hedeman (1964) (see Hyder 1966, for an historical review). Ramsey & Smith (1966) reported the motion of eleven filaments triggered by a wave emanating from a flare. They used images from three different wavelengths: centre H_α, $H_\alpha - 0.5$Å (blue wing), and $H_\alpha + 0.5$Å (red wing). They observed that the filaments alternately appear and disappear between the red and the blue wings due to the Doppler effect. This type of oscillation is called winking filament. The bottom panels of Figure 1.4 show the filament disappearance (see circles) of a winking filament. An important result was that these eleven filaments, analysed in detail by Hyder (1966), did not exhibit any correlation between the period and the size of the flare, the distance to the perturbation, or the dimensions of the filament. Furthermore, they found that one of the filaments oscillated with the same frequency and damping time in four different oscillatory events. As a consequence, it was suggested that prominences oscillate at their own characteristic frequency in agreement with theoretical models. This result is the basis of prominence seismology. The periodicity of the oscillations and their driving mechanisms are going to be addressed in Chapter 2.

1.2.1 Large amplitude oscillations

Among all the different measurable quantities, the velocity amplitude was selected as the classification parameter and distinguishes prominence oscillations into small and large amplitude events (Oliver 1999). Small amplitude oscillations (SAO) are, in general, not related to flare activity and only affect a small volume of the prominence. In addition, oscillatory amplitudes are usually smaller than $10\,\mathrm{km\,s^{-1}}$. These periodic motions are mostly interpreted as

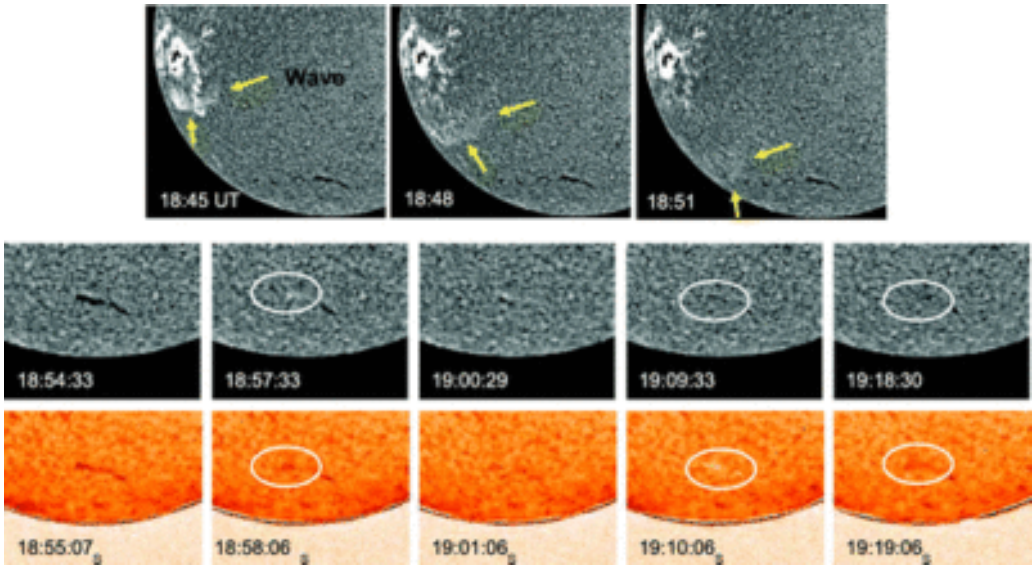

Figure 1.4: Top panel: Propagating wave observed in H_α data. Middle panel: Initial stages of a winking filament response to the passing wave in H_α. Bottom panel: Same as in the middle panel but in He I (λ10830) intensity. Adapted from Gilbert et al. (2008).

magnetohydrodynamic (MHD) waves. To comprehend the nature of the oscillatory modes, the dispersion relation of ideal MHD equations has been derived for different models. Joarder & Roberts (1992a,b, 1993) investigated in a set of three articles the normal oscillation modes of a 3D plasma slab embedded in an uniform longitudinal, transverse, and skewed magnetic field in the absence of gravity. The gravitational term was considered in Oliver et al. (1993). In a more complex configuration, Díaz et al. (2001) examined the MHD waves of a single prominence fibril surrounded by coronal medium. From these articles a wide range of oscillatory modes were obtained and the oscillatory period of the prominences was estimated (see Arregui et al. 2018, for a detailed review of SAO).

In this Thesis we are more interested in large amplitude oscillations (LAO) which are usually triggered by the interaction between the filament and an energetic external phenomenon that shakes the entire prominence (or a large part of it). Some trigger mechanisms are solar flares (Jing et al. 2003; Li & Zhang 2012), Moreton waves (Eto et al. 2002; Gilbert et al. 2008), Extreme ultraviolet Imaging Telescope (EIT) waves (Okamoto et al. 2004), or coronal shock waves (Hershaw et al. 2011; Shen et al. 2014b). Top panel of Figure 1.4 shows the propagation of a wave front (see arrows) that activates oscillations in a filament located at a large distance from the origin of the associated flare. In some cases the oscillations are associated to eruptive filaments. The velocity amplitudes associated with LAO are of the order of 20 km s^{-1} or higher. After the first time LAO have been reported by Ramsey & Smith (1966), scarce events were observed until the 2000s (Vrsnak 1984; Vrsnak et al. 1990). From 2002 onwards, the number of observational studies began to increase. In general, LAOs have been considered as a rare phenomenon, but Luna et al. (2018) have catalogued 196 filament oscillations in a period of six months (January to June 2014). Ninety of these events have been classified as LAOs. This indicates that LAOs are a frequent phenomenon.

Since the development of observation techniques and the implementation of an extensive network of sophisticated ground- and space-based observatories, a huge number of oscillatory events in prominences have been reported in detail. Different methods have been used to analyse the periodicity and the damping time of the oscillations. When the prominence is seen on the solar disk and it oscillates vertically (along the line of sight (LOS)), no horizontal motions can be detected. In these cases, to study the filament movement, the time sequence of different wavelength H_α images has to been analysed. The filament appears and disappears from one H_α wing to another one due to the Doppler shift, indicating the vertical oscillatory motions. Thus, the intensity contrasts as a function of time for different H_α wavelengths describe an oscillatory curve from which it is easy to obtain the parameters of the oscillation by fitting an exponentially decayed sine function (see Shen et al. 2014a) or a Bessel curve Knizhnik et al. (2014). When the motion of the filament is horizontal with respect to the LOS, to analyse the oscillation parameters, it is possible to study the time distance diagrams obtained by placing slits along the direction of movement and measuring the intensity along each slit as a function of time. Then, the position of the centre of mass of the thread is identified by finding the intensity minimum along the slit. Finally, these points are fitted to a curve that gives the period and damping time of the oscillation (see Figure 1.5). Selecting the best direction of each slit is not trivial (Knizhnik et al. 2014), so that a good criterion must be followed. It is important to keep in mind that if the oscillations are seen without gaps, where the oscillation amplitude is maximum, whether there is a clear transition from dark to bright regions, or the maximum number of cycles. Luna et al. (2014) have shown time–distance diagrams of an oscillatory event for three slits centred at the same position, differing only in the angle between the slit and the main direction of the filament (see Figure 1.6). They found that the oscillatory pattern in the time–distance diagrams depends strongly on this angle. Another point is that many oscillations do not follow straight trajectories so that straight slits cannot be used (Bi et al. 2014). Luna et al. (2018) generated artificial curved slits to match them with the trajectory of the cool plasma. An alternative method is to simply trace the trajectory of the position of the mass in subsequent images (see Jing et al. 2003, 2006; Vršnak et al. 2007). A more sophisticated data analysis technique is the wavelet analysis. From the wavelet spectrum, Pintér et al. (2008) investigated the temporal and spatial variations of an oscillating filament to find the period more accurately. Another point to keep in mind is the effect of the solar rotation. When the filament is observed on the disk, the rotation makes the impression that the prominence is moving upwards (downwards) when it is placed at the West (East) so that the H_α images are shifted to red- (blue-) wavelength wings. In addition, when the prominence is located at the solar limb, it is necessary to determine the apparent height above the limb.

Eto et al. (2002) observed vertical oscillations in a winking filament activated by a distant Moreton wave. In some cases the disturbing wave is too weak to be visible so that the interaction between the filament and the wave allows to infer the wave speed by studying the filament response (Gilbert et al. 2008; Shen et al. 2014a). In other cases a single wave can simultaneously activate oscillations in more than one filament (Okamoto et al. 2004; Shen et al. 2014a,b), but it is also possible that the same disturbance that produces oscillations in one filament is not able to induce oscillations in a neighbour filament. Another feature is that the same prominence can oscillate with diverse characteristic frequencies at different parts of the body. Li & Zhang (2012) presented observations of large amplitude oscillations in the

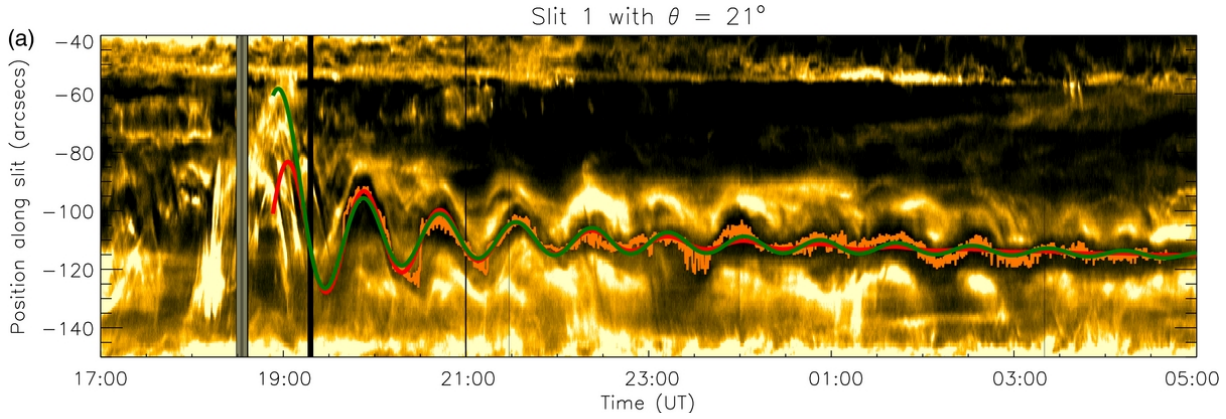

Figure 1.5: Time–distance diagrams from SDO/AIA 171 Å images. The data of the positions of the centre of the dark band are plotted as orange points. The fitted functions are plotted as red and green lines corresponding to the exponentially decaying sine and the Bessel functions, respectively. Adapted from Luna et al. (2014).

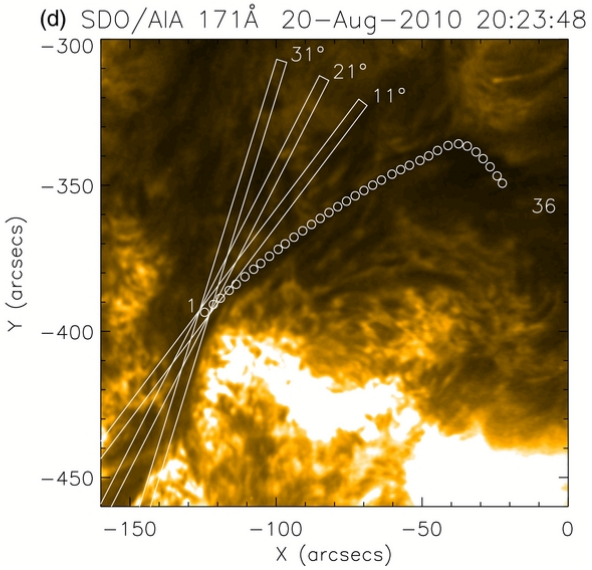

Figure 1.6: 171 Å images of a filament that oscillates. The three white rectangles are the three slits used to analysed the oscillations. The slits are centred at the same position, differing only in the angle between the slit and the main direction of the filament. Adapted from Luna et al. (2014).

southern and northern parts of a solar filament. At the same time they divided the southern part into two different axis. They found that the two southern segments oscillated out of phase with different periods and velocity amplitudes, and independently of the northern part that oscillated at its own frequency. Luna et al. (2014), to analyse the motion of the entire body of a prominence, placed 36 different slits along the filament axis at the optimal angle with respect to it. They found that the filament only oscillates at the southern part and at some northern points, but in this case similar values for the oscillation period along each slit were obtained. Shen et al. (2014a) also found the same periodicity at different

positions along the axis of a filament. When the prominence is observed above the solar limb, it is possible to study the oscillation period as a function of height by placing various slits at different heights. Hershaw et al. (2011) obtained that the prominence oscillates as a collection of separate but interacting filamentary threads, however, Shen et al. (2014b) suggested that the prominence oscillated like a vertical linear rigid body with its one end anchored on the solar surface.

Among LAO, we can distinguish the different oscillatory events according to the polarisation of the oscillatory motion relative to the axial magnetic field. Motions are classified as transverse, both vertical and horizontal, or longitudinal oscillations. In general, vertical oscillations are associated with winking filaments. Vertical oscillations can be triggered by fast-mode MHD shock waves originated from distant flares, for example Moreton waves or coronal EUV waves. Since the speed of fast waves is faster in the corona than in the chromosphere (Uchida 1968), the normal vector of the wave front points downwards as the wave travels from the flare site, pushing the prominence downwards. The transverse oscillations are motions predominantly perpendicular to the filament axis. Isobe & Tripathi (2006) reported transverse oscillations triggered by a jet-like phenomenon. The oscillatory motion was seen only in a part of the filament that erupted after few cycles. The same event was studied in detail by Isobe et al. (2007) and Pintér et al. (2008). Other transverse oscillatory events were studied by Hershaw et al. (2011), Liu et al. (2012), Xue et al. (2014), and Pant et al. (2015). Longitudinal oscillations are periodic motions along the longitudinal filament axis. A first large amplitude longitudinal oscillation was reported by Jing et al. (2003). The movement was initiated by a subflare that occurred near its footpoint. After this first detection, many observations of longitudinal oscillations have been reported (Jing et al. 2006; Vršnak et al. 2007; Zhang et al. 2012; Li & Zhang 2012; Zhang et al. 2013; Knizhnik et al. 2014; Zhang et al. 2017, 2020). A summary of the observed prominence oscillation parameters reported in some papers mentioned in this work is listed in Table 1.2. The studies are very diverse and must be analysed on a case-by-case basis. Some authors analyse a single filament, others a few number of prominences oscillating during the same event, and Luna et al. (2018) catalogue 196 different filament oscillations. Furthermore, there are many authors that extract more than one value for the same event depending on the position of the slit they use. These facts make that the values in Table 1.2 are expressed as a range of values. In general we have that transverse oscillations have shorter periods than longitudinal oscillations but it is difficult to define a range of values due to the diversity of results. It stands out the study of Hershaw et al. (2011) who observed long period transverse oscillations. The damping time per period (t_d/P) also shows a wide range of results but most events are strongly damped ($t_d/P < 3$). Low values of t_d/P mean strong damping and high t_d/P corresponds to undamped oscillations. On the other hand, negative values of t_d/P mean that the amplitude of oscillation grows with time. The other two parameters listed in Table 1.2 are the maximum displacement of the filament mass with respect to the equilibrium position (A) and the velocity amplitude (v). Luna et al. (2018) found that for SAO ($v < 10\,\mathrm{km\,s^{-1}}$) $A < 5\,\mathrm{Mm}$ in most of cases. In the catalogue the authors also found that periods tend to increase with the filament width in quiescent prominences, that larger velocity amplitudes are positively correlated with stronger damping, that for longitudinal oscillations the displacement is larger, or that longitudinal oscillations are more frequent than transverse oscillations (only one event of vertical oscillations have been reported in the

last years).

Prominence oscillation parameters					
Polarisation	P (min)	t_d/P	A (Mm)	v ($km\,s^{-1}$)	Reference
Longitudinal	34-73	1.2-1.8	1.3-30	3.5-52.4	Zhang et al. (2020)
Longitudinal	30-110	-6.2-9	$<$ 1-47	1-54.6	Luna et al. (2018)
Horizontal transverse	30-80	-4-6.2	$<$ 1-13	1-22.9	
Longitudinal	52.7-73.2	-24.2-104.5	$\sim$ 10	$<$ 1-30	Zhang et al. (2017)
Horizontal transverse	61–67	1.5-1.9	8-13	12-22	Pant et al. (2015)
Horizontal transverse	13.5	2.3-4	$\sim$ 10	65.3-89.6	Shen et al. (2014b)
Longitudinal	80.3	-	-	26.8	
Vertical transverse	11-22	1.3-3.8	-	6-14	Shen et al. (2014a)
Longitudinal	42-51.6	1.3-2.8	17-40	17-47	Luna et al. (2014)
Longitudinal	44-67	-	$\sim$ 25	30-60	Li & Zhang (2012)
Horizontal Transverse	27.2-28	3.3-5	2.2-2.5	8.3-9.4	Liu et al. (2012)
Horizontal transverse	85.9-138	0.9-4.3	3.9-40.1	4.9-41.5	Hershaw et al. (2011)

Table 1.2: Prominence oscillation parameters.

To explain the different oscillations, various models have been proposed. Hyder (1966) considered the movement as a damped harmonic oscillator embedded in a viscous fluid and in a uniform gravitational field, whose restoring force is the magnetic tension. Kleczek & Kuperus (1969) studied horizontal transverse oscillations as a damped free oscillator with the magnetic tension as the restoring force, and radiation of acoustic waves as the attenuation mechanism. Using these assumptions, they found that the oscillation period (P) for horizontal transverse oscillations is

$$P = 4\pi L B^{-1} \sqrt{\pi \rho_p}, \tag{1.1}$$

where $2L$ is the length of the prominence, B is the magnetic field strength, and ρ_p is the prominence density. Later, Jing et al. (2003) proposed different mechanisms to explain the physics of an oscillatory motion along a filament observed on October 24th 2001. Firstly, they suggested as the driving mechanism the gravitational force when a concave upwards magnetic flux tube is considered as the main configuration of the cool filament thread. The second possibility they proposed to explain the oscillations was a pressure imbalance that drives plasma motions along field lines. Finally, they suggested as a restoring force the magnetic tension for motions perpendicular to the local magnetic field. Furthermore, Vršnak et al. (2007) detected oscillations along a filament on January 23rd 2002 and proposed that the restoring force of the motion was caused by the magnetic pressure gradient along the filament axis, and Li & Zhang (2012), who studied longitudinal oscillations in a solar filament on April 7th 2012, suggested that the restoring force was the coupling between the magnetic tension and the gravity. Finally, Luna & Karpen (2012) proposed that the main restoring force is the projected gravity along the magnetic field. They found that the periodicity of longitudinal oscillations depends on the radius of the curvature of the magnetic dip as

$$P = 2\pi \sqrt{R/g}\ , \tag{1.2}$$

where g is the solar gravity acceleration. This model is called the pendulum model.

An important characteristic of the reported events is that in most cases the amplitude of the oscillations attenuates. In the first study, Ramsey & Smith (1966) already mentioned that the observed winking filaments rapidly damped and only few oscillations were visible, between one and a half and four cycles. On one side, Hyder (1966), who listed the characteristic decay constant of the 11 filaments studied by Ramsey & Smith (1966), suggested that the attenuation was caused by viscosity in the corona. On the other hand, Kleczek & Kuperus (1969) assumed that transverse oscillations are damped by the emission of acoustic waves from the prominence. In more recent studies, other mechanisms have been proposed to explain the observed damping, for example thermal damping such as radiative cooling (Terradas et al. 2001) and heat conduction (Soler et al. 2007), ion-neutral collisions in partially ionised plasmas (Forteza et al. 2007), mass flows (Ruderman & Luna 2016; Soler et al. 2008), wave leakage (Schutgens & Tóth 1999), or resonant absorption (Goossens et al. 2002). The most accepted damping mechanism in transverse oscillations seems to be the resonant absorption (see Section 1.3.1). It appears in the prominence-corona transition region, where the global oscillation of the whole prominence is transferred to Alfvén continuous modes whose amplitude grows with time until all the energy of the global mode has been transferred and phase mixing develops (Arregui et al. 2018). By contrast, Luna et al. (2014) proposed that longitudinal oscillations are damped by continuous mass accretion onto the filament threads. However, Zhang et al. (2012) obtained that in order to explain the decay of the observed longitudinal oscillations, a combination of radiation and heat conduction plus wave leakage and mass accretion must be considered. Damping mechanisms for oscillations in solar prominences are reviewed by Arregui & Ballester (2011). The damping of transverse oscillations is going to be addressed in Chapter 2.

1.2.2 Prominence seismology

From the properties of the oscillations such as their periodicity, damping time, or polarization, and the characteristics of the filament body, it is possible to derive the physical conditions of a medium. This process is called prominence seismology (Ballester 2014, 2015). Traditionally, we separate the seismology methods by using LAO from SAO. The models that explain LAO are based on linear oscillators whose restoring forces are magnetic tension, magnetic pressure gradient or projected gravity. In the case of SAO, the oscillations are interpreted in terms of MHD waves in idealised prominence models, such as prominence slabs (Joarder & Roberts 1992a,b, 1993; Oliver et al. 1992, 1993; Oliver & Ballester 1995; Díaz et al. 2001, 2003) or cylindrical flux tubes (Goossens et al. 1992; Díaz et al. 2010; Soler et al. 2010), that provide a variety of MHD modes with their own characteristic frequency.

The first attempt to measure magnetic fields from the parameters of LAO (see Oliver 2009; Arregui et al. 2018, for reviews on prominence seismology using SAO) was made by Hyder (1966). Based on his damped harmonic oscillator model, he calculated the radial component of the filament magnetic field and the coronal effective viscosity coefficients. This method was also utilised in transverse oscillations by Shen et al. (2014b). According to the model of Kleczek & Kuperus (1969) (see Equation (1.1)), Isobe & Tripathi (2006) estimated the Alfvén velocity and the magnetic field that causes the restoring force of a transverse horizontal oscillation. They assumed a filament density of $\rho = 10^{-13}$ g cm^{-3} and from the measured

values of $L = 100\,\mathrm{Mm}$ and $P = 120\,\mathrm{min}$ they obtained the reasonable values $v_\mathrm{A} = 87\,\mathrm{km\,s^{-1}}$ and $B = 9.8\,\mathrm{G}$. In a similar analysis, Gilbert et al. (2008) inferred a magnetic field of $B = 30\,\mathrm{G}$. They suggested that the large inferred field strength is consistent with the relatively smaller size and height of their filament. Luna et al. (2018) also used the Kleczek and Kuperus equation to estimate the magnetic field strength of 33 transverse oscillatory events. It is important to mention that Luna et al. (2018) did not distinguish between LAO and SAO for seismology purposes. It does not seem strange that for LAO some authors utilise seismology methods associated to SAO or vice versa. For example, Pant et al. (2015) made MHD seismology of a loop-like filament tube by observing transverse large amplitude oscillations. They used the thin tube thin boundary approximations (see Goossens et al. 2008) to estimate the magnetic field and the thickness of the non-uniform layer of the tube (see Equation (1.54)). Mazumder et al. (2020) also studied large amplitude transverse oscillations applying MHD models based on the studies of Díaz et al. (2002) and Dymova & Ruderman (2005). Getting back to the oscillator models, it is worth to mention that while Isobe & Tripathi (2006) used the Kleczek and Kuperus equation to estimate the magnetic field strength of a transverse oscillation, for the same oscillatory event, Pintér et al. (2008) calculated the poloidal and axial component of the magnetic field by using the same method as Vršnak et al. (2007) utilised for seismology purposes in large amplitude longitudinal oscillations. Vršnak et al. (2007) considered longitudinal oscillations to be a simple harmonic motion so that they developed a simple model to obtain the poloidal and axial component of the magnetic field. This method was also utilised in longitudinal oscillations by Shen et al. (2014b). However, the most widely used seismology method in longitudinal oscillations is based on the pendulum model. Several authors estimated the curvature radius of magnetic dips from Equation (1.2) for their reported longitudinal oscillations (Luna et al. 2014; Knizhnik et al. 2014; Bi et al. 2014; Zhang et al. 2017; Luna et al. 2018; Zhang et al. 2020). Specifically, Luna et al. (2018) obtained that the curvature radius ranges from $R = 25\,\mathrm{Mm}$ to $R = 300\,\mathrm{Mm}$ with a mean value of $R = 89\,\mathrm{Mm}$. Furthermore, based on the pendulum model it is possible to estimate the minimum field strength as a function of the thread oscillation period (Luna & Karpen 2012),

$$B \geq \sqrt{\frac{{g_0}^2\, m\, n}{4\,\pi^2}}\, P, \tag{1.3}$$

being n the particle number density in the thread, m the mean particle mass, and g_0 the gravitational acceleration at the solar surface. From Equation (1.3), Luna et al. (2018) found that the magnetic field ranges from $B = 9\,\mathrm{G}$ to $B = 48\,\mathrm{G}$.

1.3 Basic equations

The Sun is made of plasma which is an electrically conducting fluid and therefore it interacts with magnetic fields. To describe its dynamics, it is necessary to solve a simplified form of Maxwell's equations (Faraday's, Ampere's, and Gauss's laws, and the solenoidal condition) simultaneously together with the fundamental equations of fluid dynamics. The mathematical model that merges both formalisms is Magnetohydrodynamics. MHD was introduced for the first time by Hannes Alfvén in 1942 (Alfvén 1942). The basic equations of MHD are derived in detail in Chapter 2 of Priest (2014). As a first approximation, MHD neglects

relativistic effects, since the characteristic electromagnetic or plasma speeds are all assumed to be much smaller than the speed of light (c). This assumption implies that local accumulations in time of charge (displacement current, $\frac{1}{c^2}\frac{\partial E}{\partial t}$) are negligible in the Ampere's law, or that electric currents flow in closed circuits ($\nabla \cdot \mathbf{j} = 0$). A second assumption is that plasma in solar atmosphere is electrically neutral. This neutralization effectively takes place over a distance of a few Debye shielding lengths ($\lambda_{\rm D}$) (Goossens 2003), which is a measure of the distance over which electrons can deviate appreciably from positive ions (Coulomb interactions). If the length scales of the dynamics of plasma are near or less than $\lambda_{\rm D}$, then the approximation breaks down and significant deviations from quasi-neutrality occur.

A third assumption is the treatment of the plasma as a continuous fluid assuming that it is in thermodynamic equilibrium. The continuum assumption is valid for lengths and time scales of global motions that are considered much larger than the spatial scales (mean-free path, $\lambda_{\rm mfp}$) and shorter than temporal scales (collision time, $\tau_{\rm n}$) that characterise the microscopic processes that couple the particles. Furthermore, the charged particles are tied to the magnetic field lines. The charged particles move in circles (cyclotron motions) of radius $r_{\rm L}$ around the magnetic field lines at a frequency $\Omega_{\rm L}$. $r_{\rm L}$ and $\Omega_{\rm L}$ are the Larmor radius and frequency, respectively. In this context, the MHD approximation is valid when the global length and time scales are larger than the Larmor parameters. In the solar corona (where $T = 10^6\,{\rm K}$, $B = 10\,{\rm G}$, and the ion number density $n_{\rm i} = 10^{13}\,{\rm m}^{-3}$) we have that $\lambda_{\rm L} \sim 0.02\,{\rm m}$, $\lambda_{\rm mfp} \sim 1\,{\rm Mm}$, $\tau_{\rm n} \sim 2\times10^{20}\,{\rm s}$; and $\Omega_{\rm L}^{-1} \sim 5.7\times10^{-9}\,{\rm s}$, $r_{\rm L} \sim 0.02\,{\rm m}$ for electrons, and $\Omega_{\rm L}^{-1} \sim 10^{-5}\,{\rm s}$, $r_{\rm L} \sim 1\,{\rm m}$ for ions. In this way, the MHD requirements listed in this section are satisfied in the considered coronal environment and in the phenomena studied in this Thesis, so that this theory provides an accurate description of many of the complicated interactions of magnetic fields with the solar plasma.

Finally, we consider in this Thesis that plasma is fully ionised. The sun is mostly ionised due to the high temperature and the corona, with temperatures of the order of $10^6\,{\rm K}$, is not an exception. However, in cooler layers such as the photosphere and the lower chromosphere as well as in solar prominences, the presence of neutrals has important physical effects, for example for chromospheric heating (Khomenko & Collados 2012), prominence equilibrium (Terradas et al. 2015b), resonant absorption (Soler et al. 2009a, 2011), or coronal rain (Oliver et al. 2016). When the degree of ionisation, that is the proportion of neutrals and ions that are ionised, is small, the plasma is partially ionised. Neutrals do not interact with magnetic fields but are coupled with ions through collisions. To describe the interaction between the different kind of particles it is considered that each of the components of the plasma (electrons, ions, and neutrals) can be treated as a separate fluid through a multi-fluid theory (Khomenko et al. 2014a; Ballester et al. 2018). The single-fluid MHD equations used in this Thesis derive from the multi-fluid equations when the high-frequency short scale dynamics of the electrons and ions are removed, and when collisional invariance, that neglects the collision terms, is considered. However, in partially ionised plasmas, the coupling between neutrals and ionised components of the magnetised plasma, that introduces physical effects such as Cowling's resistivity, isotropic thermal conduction by neutrals, heating due to ion/neutral friction, heat transfer due to collisions, charge exchange, or ionization energy, must be taken into account (Ballester et al. 2018).

In spite of the importance of partially ionised plasmas, in this Thesis we neglect the effects

of neutrals and deal with single-fluid MHD. The behaviour of neutrals on the support of prominences against gravity is similar to that of fully ionised plasmas due to the strong coupling between ions and neutrals (Terradas et al. 2015b) so that the simulations in Chapters 2 and 3 would not significantly change in this respect. An aspect that we have not considered in the present Thesis is the damping of the oscillations due to ion-neutral collisions (Khodachenko et al. 2004, 2006), that is more important for fast waves than for slow waves (Forteza et al. 2007); and how the presence of neutrals contributes to resonant absorption. Soler et al. (2009a) found that the ratio $t_{\rm d}/P$ depends very slightly on the ionization degree for resonant damping and Soler et al. (2011) found that in the range of typically observed periods of transverse prominence thread oscillations, the effect of Cowling's diffusion (and so the ionization degree) is negligible. In consequence, the simplest form of the MHD equations is a reasonable model to describe oscillations in solar prominences.

1.3.1 Ideal MHD

The result of all these assumptions is the ideal MHD equations that is used for all the main results in this Thesis. Ideal MHD is a simplified situation and not representative for the actual processes in nature. However, ideal MHD certainly provides good approximations for many of the dynamical properties of hot and strongly magnetised plasmas, like those in the solar corona (Schnack 2009), so MHD is valid for the description of large dynamical processes like the ones studied in this Thesis.

The ideal MHD equations solved in this Thesis are

$$\frac{D\rho}{Dt} = -\rho\nabla\cdot\mathbf{v}, \tag{1.4}$$

$$\rho\frac{D\mathbf{v}}{Dt} = -\nabla p + \frac{1}{\mu}(\nabla\times\mathbf{B})\times\mathbf{B} - \rho\mathbf{g}, \tag{1.5}$$

$$\frac{\partial\mathbf{B}}{\partial t} = \nabla\times(\mathbf{v}\times\mathbf{B}), \tag{1.6}$$

$$\frac{Dp}{Dt} - \frac{\gamma p}{\rho}\frac{D\rho}{Dt} = 0, \tag{1.7}$$

$$p = \rho R\frac{T}{\tilde{\mu}}, \tag{1.8}$$

$$\nabla\cdot\mathbf{B} = 0, \tag{1.9}$$

being $D/Dt = \partial/\partial t + \mathbf{v}\cdot\nabla$ the advective derivative. Equations (1.4)-(1.7) are eight equations in the eight variables density ρ, fluid pressure p, velocity $\mathbf{v}$ (three components), and magnetic field $\mathbf{B}$ (three components). We have that μ is the magnetic permeability and γ is the ratio of the specific heat that we consider to be constant. We will take $\gamma = 5/3$, the value appropriate

for a fully ionised gas, that corresponds to an ideal monatomic gas with 3 degrees of freedom. Equation (1.4) is the continuity equation which describes the mass flowing into and out of a physically volume element and expresses the conservation of matter. Equation (1.5) is the equation of motion and describes changes in the momentum as a result of forces acting in the fluid. The forces that act on a plasma element are expressed on the right-hand side of the equation. The first force is the pressure gradient force, the second term is the Lorentz force, and the third one is the gravity force. Another force that acts on the plasma but which we have neglected is, for example, the viscous force. Temporal changes in the magnetic field are described by the induction equation, Equation (1.6). Here we have neglected the magnetic diffusion of the fluid so that only the advection of the magnetic field has been taken into account. When we neglect diffusivity the fluid is a perfect conductor and, in general, the plasma of the solar atmosphere acts as such. Under this constraint, the magnetic field lines moves with the plasma motions. While movements along the magnetic lines do not modify the field, transverse movements transport the lines with the flow, in that case the magnetic field lines are termed frozen. Equation (1.7) describes the energy balance equation. We consider adiabatic processes so that we do not take energy sources or drains such as radiative cooling or heat conduction into account. We assume the plasma as a perfect gas so that the equation of state is the ideal gas law, Equation (1.8), where R is the ideal gas constant and $\tilde{\mu}$ the mean molecular weight. Finally, there is a constraint on the magnetic field, Equation (1.9), which is the Gauss's law for magnetism. This constraint is the statement that magnetic monopoles do not exist (see Roberts 2019, for a detailed description of the MHD equations).

Alternatively, the set of ideal MHD governing equations can be expressed in terms of entropy (s) rather than the more usual pressure or thermal energy variables, and in terms of $\ln \rho$. Moreover, the induction equation can be solved in terms of the magnetic vector potential ($\mathbf{A}$) defined so that the curl of $\mathbf{A}$ is equal to the magnetic field ($\mathbf{B} = \nabla \times \mathbf{A}$), and the equation of motion in terms of the gravity potential ($\Phi_{\rm grav}$) and the electric current density ($\mathbf{j} = \frac{1}{\mu}\nabla \times \mathbf{B}$). Thus, Equations (1.4)-(1.7) are rewritten as follows:

$$\frac{D \ln \rho}{Dt} = -\nabla \cdot \mathbf{v} \ , \tag{1.10}$$

$$\frac{D\mathbf{v}}{Dt} = -c_{\rm s}^2 \nabla \left(\frac{s}{c_{\rm p}} + \ln \rho \right) - \nabla \Phi_{\rm grav} + \frac{\mathbf{j} \times \mathbf{B}}{\rho} \ , \tag{1.11}$$

$$\frac{\partial \mathbf{A}}{\partial t} = \mathbf{v} \times \mathbf{B} \ , \tag{1.12}$$

$$\rho T \frac{Ds}{Dt} = 0. \tag{1.13}$$

Here, $c_{\rm p}$ is the heat capacity at a constant pressure (assumed to be equal to one), and the squared sound speed is given by

$$c_{\rm s}^2 = \gamma \frac{p}{\rho} = {c_{\rm s0}}^2 \exp \left[\gamma s / c_{\rm p} + (\gamma - 1) \ln \frac{\rho}{\rho_0} \right] , \tag{1.14}$$

where c_{s0} and ρ_0 are the reference sound speed and the density, respectively. In Chapter 2, the numerical simulations of oscillations in solar prominences will be performed by solving the Equations (1.10)-(1.13).

1.3.2 Lorentz Force

Magnetic effects in the equation of motion, Equation (1.5), are determined by the Lorentz force $\frac{1}{\mu}(\nabla \times \mathbf{B}) \times \mathbf{B}$. As $\mathbf{B}$ changes, the magnetic force influences the plasma changing its velocity. The Lorentz force can be divided into two terms. First we know the vector identity

$$\nabla(\mathbf{A} \cdot \mathbf{B}) = (\mathbf{A} \cdot \nabla)\mathbf{B} + (\mathbf{B} \cdot \nabla)\mathbf{A} + \mathbf{A} \times (\nabla \times \mathbf{B}) + \mathbf{B} \times (\nabla \times \mathbf{A}) \tag{1.15}$$

that reduces to

$$\mathbf{B} \times (\nabla \times \mathbf{B}) = \frac{1}{2}\nabla(\mathbf{B} \cdot \mathbf{B}) - (\mathbf{B} \cdot \nabla)\mathbf{B} \tag{1.16}$$

when $\mathbf{A} = \mathbf{B}$. This expression is equivalent to

$$(\nabla \times \mathbf{B}) \times \mathbf{B} = -\frac{1}{2}\nabla(\mathbf{B} \cdot \mathbf{B}) + (\mathbf{B} \cdot \nabla)\mathbf{B}. \tag{1.17}$$

Introducing Equation (1.17) into the Lorentz force we obtain the following expression

$$\frac{1}{\mu}(\nabla \times \mathbf{B}) \times \mathbf{B} = -\nabla(\frac{B^2}{2\mu}) + (\mathbf{B} \cdot \nabla)\frac{\mathbf{B}}{\mu}. \tag{1.18}$$

By comparing the first term of the right-hand side of Equation (1.18) with the pressure force of Equation (1.4) we can see that this term acts as a magnetic pressure force. The second term is the magnetic tension. When we introduce a distortion or bend into a magnetic field line it applies a tension force, just like an elastic band, that acts trying to straighten out the field line. Since the Lorentz force is perpendicular to $\mathbf{B}$, the contribution from the terms acting in the direction along the field line must cancel. We can express the magnetic tension as follows,

$$(\mathbf{B} \cdot \nabla)\frac{\mathbf{B}}{\mu} = \frac{1}{\mu}B(s)\frac{\partial}{\partial s}[B(s)\hat{\mathbf{s}}] = \hat{\mathbf{s}}\frac{\partial}{\partial s}\left(\frac{B^2}{2\mu}\right) + \frac{B^2}{\mu}\frac{\partial \hat{\mathbf{s}}}{\partial s}, \tag{1.19}$$

where we have considered $B = B(s)\hat{\mathbf{s}}$, being $\hat{\mathbf{s}}$ the unit vector pointing along the magnetic field and $B(s)$ the field strength at s. From vector calculus we know that

$$\frac{\partial \hat{\mathbf{s}}}{\partial s} = \frac{1}{R_c(s)}\hat{\mathbf{n}}, \tag{1.20}$$

being $R_c(s)$ the radius of curvature of the field line and $\hat{\mathbf{n}}$ the unit vector perpendicular to the field line. Therefore, the Lorentz force can be expressed as

$$\frac{1}{\mu}(\nabla \times \mathbf{B}) \times \mathbf{B} = -\nabla\left(\frac{B^2}{2\mu}\right) + \hat{\mathbf{s}}\frac{\partial}{\partial s}\left(\frac{B^2}{2\mu}\right) + \frac{B^2}{\mu R_c(s)}\hat{\mathbf{n}}. \tag{1.21}$$

We see that the component along the field line of the magnetic pressure force cancels with the parallel term of the magnetic tension, so that only perpendicular terms contribute to the Lorentz force. Since the sharper the bend in the field line, the smaller the radius of curvature, we obtain that the tension force acting to straighten out the field increases with decreasing R_c.

1.3.3 Magnetohydrostatic equilibrium

Solar filaments are dynamic structures. However, in general we can observe that quiescent prominences remain static for long periods of time. For this reason, the study of prominence models are grounded in magnetohydrostatic equilibrium. The inertial term in the equation of motion, i.e., the left-hand side term of Equation (1.5), can be neglected when the flow speed is much smaller than the sound speed, Alfvén speed and gravitational free-fall speed, meaning that we have a magnetohydrostatic balance between the pressure gradient, the Lorentz force, and the gravitational force.

As a first approximation we can assume an uniform vertical magnetic field $\mathbf{B} = B_0\hat{\mathbf{z}}$ and a gravity force that acts along the negative z-axis $\mathbf{g} = -g\hat{\mathbf{z}}$. For this case the Lorentz force is null so that from Equation (1.43) together with Equation (1.8) we obtain that

$$\frac{dp}{dz} = -\rho(z)g = -\frac{g\tilde{\mu}}{RT(z)}p(z) = -\frac{p(z)}{\Lambda(z)}, \tag{1.22}$$

where $\Lambda(z)$ is the pressure scale height. If we integrate Equation (1.22) we have that

$$p(z) = p_0 \exp\left[-\int_0^z dz/\Lambda(z)\right], \tag{1.23}$$

where p_0 is the pressure at $z = 0$. When the temperature is constant along the field lines, $\Lambda(z)$ is uniform and Equation (1.23) reduces to

$$p(z) = p_0 \exp\left(-z/\Lambda\right). \tag{1.24}$$

The result is an isothermal stratified atmosphere whose pressure and density decrease exponentially with z.

Force-free magnetic arcades

Under other circumstances, different from the previous case, not all the terms in Equation (1.5) are equally important. In solar prominences the Lorentz force dominates over the gas pressure gradient and the gravity force, hence, we can consider a force-free magnetic field that fulfills

$$\mathbf{j} \times \mathbf{B} = \frac{1}{\mu}(\nabla \times \mathbf{B}) \times \mathbf{B} = 0, \tag{1.25}$$

being $\mathbf{j}$ the current density. When the cross product of two vectors is zero, these vectors are parallel

$$(\nabla \times \mathbf{B}) \parallel \mathbf{B}, \tag{1.26}$$

therefore, the electric current flows along the magnetic field and we can express Equation (1.25) as

$$\nabla \times \mathbf{B} = \alpha\mathbf{B}, \tag{1.27}$$

being α a constant along each magnetic field line that satisfies

$$(\mathbf{B} \cdot \nabla)\, \alpha = 0. \tag{1.28}$$

In the particular case of having the same value of α on each field line, we talk about a constant-α field. Imposing the curl into Equation (1.27) we obtain the Helmholtz equation

$$\left(\nabla^2 + \alpha^2\right) \mathbf{B} = 0. \tag{1.29}$$

When we consider a simple constant-α field with the form $\mathbf{B} = \mathbf{B}(x, z)$, the three components of Equation (1.29) are

$$\frac{\partial^2 B_x}{\partial x^2} + \frac{\partial^2 B_x}{\partial z^2} = -\alpha^2 B_x, \tag{1.30}$$

$$\frac{\partial^2 B_y}{\partial x^2} + \frac{\partial^2 B_y}{\partial z^2} = -\alpha^2 B_y, \tag{1.31}$$

$$\frac{\partial^2 B_z}{\partial x^2} + \frac{\partial^2 B_z}{\partial z^2} = -\alpha^2 B_z. \tag{1.32}$$

When we take solutions of separable form, $B_z = X(x)Z(z)$, then Equation (1.32) reduces to

$$\frac{1}{X}\frac{d^2 X}{dx^2} = -\frac{1}{Z}\frac{d^2 Z}{dz^2} - \alpha^2 = -k^2. \tag{1.33}$$

The solution of Equation (1.33) is

$$B_z = -B_0 \sin(kx) \exp(-lz), \tag{1.34}$$

being $l = (k^2 - \alpha^2)^{1/2}$.

From Equation (1.27) we obtain that $\alpha B_z = \frac{\partial B_y}{\partial x}$ and $\alpha B_x = -\frac{\partial B_y}{\partial z}$, so that

$$B_y = \frac{\alpha}{k} B_0 \cos(kx) \exp(-lz), \tag{1.35}$$

$$B_x = \frac{l}{k} B_0 \cos(kx) \exp(-lz). \tag{1.36}$$

If we impose $B_y = 0$ when $kx = \pi/2$, we have that $f(z) = 0$. The result is a periodic magnetic arcade configuration whose lateral extension is related to the parameter k. The term l is a measure of the vertical magnetic scale height and B_0 is the magnetic field strength at the reference level. When $k = l$, $\alpha = 0$ the magnetic field is purely potential and B_y becomes null. However, when $\alpha \neq 0$, the magnetic component in the y-direction introduces a shear in the system. The amount of shear in the structure is related to the parameter l/k as

$$\theta = \operatorname{atan}\left(B_y/B_x\right) = \operatorname{atan}\left(k^2/l^2 - 1\right)^{1/2}. \tag{1.37}$$

The magnetic field lines in the given configuration do not have any dips because in this case the magnetic structure is bipolar. Since we are interested in a configuration with dips, we select a particular superposition of two magnetic arcades that mimics a quadrupolar configuration. In this way, the dipped magnetic arcade is expressed as follows:

$$\begin{cases} B_x = \frac{l_1}{k_1} B_{01} \cos(k_1 x) \exp[-l_1(z - z_0)] - \frac{l_2}{k_2} B_{02} \cos(k_2 x) \exp[-l_2(z - z_0)] \ , \\ B_y = \frac{\alpha}{k_1} B_{01} \cos(k_1 x) \exp[-l_1(z - z_0)] - \frac{\alpha}{k_2} B_{02} \cos(k_2 x) \exp[-l_2(z - z_0)] \ , \\ B_z = -B_{01} \sin(k_1 x) \exp[-l_1(z - z_0)] + B_{02} \sin(k_2 x) \exp[-l_2(z - z_0)] \ . \end{cases} \tag{1.38}$$

The individual arcades are labelled with the subindices 1 and 2, respectively. To satisfy the Helmholtz equation, Equation (1.29), each individual arcade must have the same α, therefore we have the constraint

$$k_1^2 - l_1^2 = k_2^2 - l_2^2. \tag{1.39}$$

For the new magnetic configuration, the reference level of the arcade can be located according

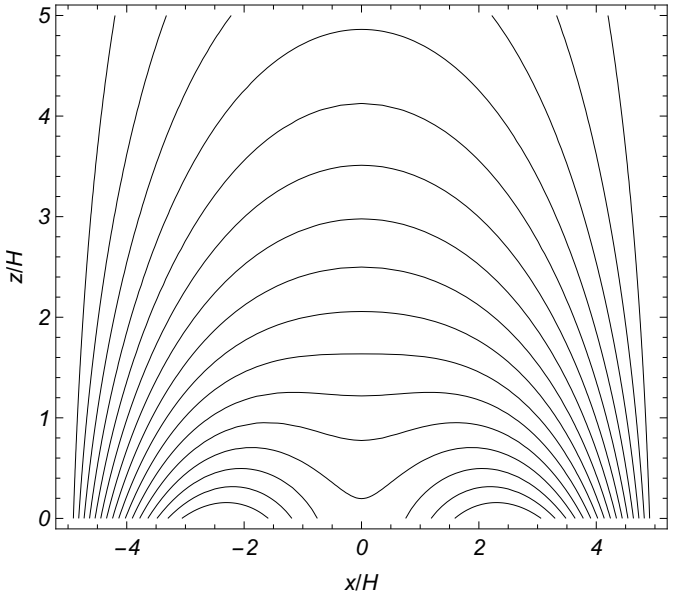

Figure 1.7: Magnetic field lines in the xz-plane. In this plot $B_{01} = B_{02}$, $k_1 = \pi/2L$, $k_2 = 3k_1$, $z_0 = -0.2\,H$, and $l_1/k_1 = 1$. The y-component of the magnetic field is null. The dimensions are to scale H.

to the parameter z_0. In Figure 1.7 some magnetic field lines are plotted in the xz-plane of an unsheared quadrupolar structure, Equation (1.38), for $B_{01} = B_{02}$, $k_1 = \pi/2L$, $k_2 = 3k_1$, and $z_0 = -0.2\,H$, where L is the width of the full structure. Figure 1.7 shows that at $x = 0$, the radius of the curvature takes low positive values in the bottom part of the structure and grows until $z = 1.55\,H$, where the field line becomes flat. From this point, the dip is lost and the curvature becomes concave downwards.

The combination between the isothermal stratified atmosphere that fulfils Equation (1.24) and the magnetic arcade given by Equation (1.38) will be the basis of the initial configuration used in the numerical study of prominence oscillations in Chapters 2 and 3.

Effect of gravity and magnetic field curvature

For the quadrupolar magnetic arcade configuration the magnetic dip is not caused by the weight of the prominence and the magnetic field does not influence the plasma structure when the corona background is in static equilibrium. However, the shape of the dipped field lines can be determined by the balance between magnetic and gravitational forces. Hood & Anzer (1990) took the magnetic field as

$$\mathbf{B} = (X(x), Y(x), Z(x)) \exp(-kz) \tag{1.40}$$

and gas pressure as

$$p = P(x) \exp(-2kz). \tag{1.41}$$

They considered the temperature as a function of the horizontal distance $T = T(x)$ and the density related to the pressure and the temperature through the gas law (Equation (1.8)). From Gauss's law, Equation (1.9), and Equation (1.40) they obtained that

$$X' = kZ. \tag{1.42}$$

When Equation (1.42) is introduced into the y-component of the magnetohydrostactic equation of motion

$$-\nabla p + \frac{1}{\mu}(\nabla \times \mathbf{B}) \times \mathbf{B} - \rho \mathbf{g} = 0, \tag{1.43}$$

we have that

$$Y = \alpha X, \tag{1.44}$$

being α a shear parameter. Applying the same procedure to the x-component of Equation (1.43) results in

$$2\mu P + X^2 + Y^2 + Z^2 = 2\mu P_{\mathrm{T}} = \text{constant} \tag{1.45}$$

which leads to the equilibrium having a constant total pressure in the horizontal direction. Finally, the vertical component of Equation (1.43) reduces to

$$Z' = \frac{k}{X}\left[\left(1 - \frac{1}{2k\Lambda}\right) Z^2 + \frac{1}{2k\Lambda}\left(2\mu P_{\mathrm{T}} - X^2 - Y^2\right) - 2\mu P_{\mathrm{T}}\right], \tag{1.46}$$

being the pressure scale height $\Lambda(x) = RT(x)/\tilde{\mu}g$. Equations (1.42) and (1.46) must be solved numerically by imposing the initial conditions at the centre of the prominence $X(0) = X_0$, $Y(0) = \alpha X_0$, $Z(0) = 0$, and $P(0) = P_0$ and setting a temperature profile that resembles a typical prominence. The result of Hood & Anzer (1990) is a 2.5-dimensional non-isothermal magnetohydrostatic model for a prominence in a force-free coronal arcade whose dip is self-consistently created by the weight of the heavy prominence. Figure 1.8 shows some magnetic field lines together with the density profile in the xz-plane for a typical Hood & Anzer prominence model (H&A, hereafter). In Section 3.3 more details about this equilibrium will be given.

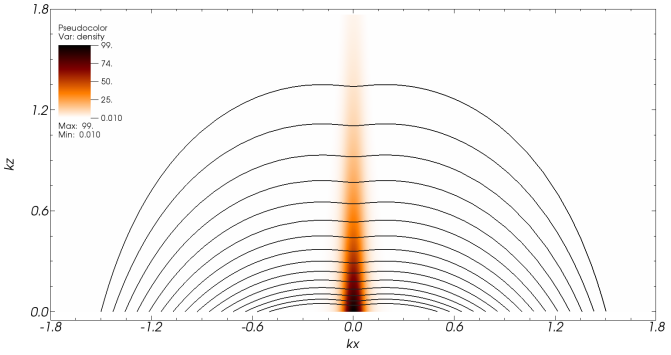

Figure 1.8: Magnetic field lines and density in the xz-plane for a Hood & Anzer model of a prominence. Density is normalised to $\frac{X_0^2}{\mu v_{\mathrm{A}0}^2}$.

1.3.4 MHD waves

Since prominence oscillations are interpreted as MHD waves, in this section we review some basic properties of MHD waves in the solar atmosphere. To describe the different modes of oscillation, first it is considered that the amplitude of the waves is small, so that the basic MHD Equations (1.4)-(1.7) can be linearised assuming that each physical quantity can be written as an equilibrium value plus a perturbation and then neglecting all non-linear terms. After the linearisation, it is possible to obtain analytical solutions for the wave frequency in some simple models. The linearised equations are listed, for example, in Schnack (2009) or Roberts (2019). The combination of the linearised equations reduces to a wave equation that is the ground of the study of MHD waves.

We consider an uniform magnetic field aligned with the z-axis in an uniform medium. Under these conditions, the linearised MHD equations can be combined to arrive at two uncoupled wave equations, namely

$$\frac{\partial^2 \omega_z}{\partial t^2} = v_{\mathrm{A}}^2 \frac{\partial^2 \omega_z}{\partial z^2}, \tag{1.47}$$

and

$$\frac{\partial^4 \Delta}{\partial t^4} - \left(c_{\mathrm{s}}^2 + v_{\mathrm{A}}^2\right) \nabla^2 \frac{\partial^2 \Delta}{\partial t^2} + c_{\mathrm{s}}^2 v_{\mathrm{A}}^2 \nabla^2 \frac{\partial^2 \Delta}{\partial z^2} = 0, \tag{1.48}$$

where $\omega_z = \frac{\partial v_x}{\partial y} - \frac{\partial v_y}{\partial x}$ is the z-component of voticity (along the magnetic field line) and $\Delta = \nabla \cdot \mathbf{v}$ is the compressibility (see Roberts 2019). The wave equations contain the fundamental speeds of MHD: the sound speed $c_{\mathrm{s}} = \left(\frac{\gamma p_0}{\rho_0}\right)^{1/2}$, where ρ_0 and p_0 refere to the fluid density and pressure in the unperturbed state of the medium; and the Alfvén speed $v_{\mathrm{A}} = \left(\frac{B_0^2}{\mu \rho_0}\right)^{1/2}$ where B_0 is the equilibrium field strength. The speeds c_{s} and v_A characterise all wave phenomena described by MHD equations. Other speeds, such as the kink speed, also play an important role, but these are expressed in terms of c_{s} and v_A.

Now we assume the perturbations as plane waves proportional to $\exp\left[i\left(\omega t - \mathbf{k} \cdot \mathbf{r}\right)\right]$, where ω is the wave frequency, $\mathbf{k} = (k_x, 0, k_z)$ is the wave vector, and $\mathbf{r} = (x, y, z)$ is the position

vector. In terms of plane waves, Equations (1.47) and (1.48) provide us with the dispersion relation for Alfvén waves

$$\left[\omega^2 - k_z^2 v_{\rm A}^2\right] \omega_z = 0, \tag{1.49}$$

and for magnetoacoustic waves, namely

$$\left[\omega^4 - k^2\left(c_{\rm s}^2 + v_{\rm A}^2\right)\omega^2 + k^2 k_z^2 c_{\rm s}^2 v_{\rm A}^2\right] \Delta = 0. \tag{1.50}$$

Here, $k^2 = k_x^2 + k_z^2$, $k_z = k\cos\theta$, and θ is the angle that the wave vector forms with the equilibrium magnetic field.

Now we suppose that the z-component of vorticity $\omega_z \neq 0$ so that to satisfy Equation (1.49), $\omega^2 = k_z^2 v_{\rm A}^2$ and Equation (1.50) then implies that $\Delta = 0$. In this case, we obtain a disturbance that propagates with the Alfvén speed and involves no compression of the plasma. This is the Alfvén wave. On the other hand, when $\omega_z = 0$ and $\Delta \neq 0$ the solution of Equation (1.50) is

$$\omega^2 = \frac{k^2}{2}\left[\left(v_{\rm A}^2 + c_{\rm s}^2\right) \pm \sqrt{\left(v_{\rm A}^2 + c_{\rm s}^2\right)^2 - 4 v_{\rm A}^2 c_{\rm s}^2 \cos^2\theta}\right]. \tag{1.51}$$

Here, minus root corresponds to the slow magnetoacustic wave and the plus root gives the fast magnetoacustic wave. The properties of fast and slow magnetoacustic waves depend on the relation between the sound and the Alfvén velocities. The presence of a magnetic field in the equilibrium state of the uniform medium introduces a preferred direction in the magnetohydrodynamic system that affects the behaviour of the phase speed (ω/k) of the waves. In other words, a wave propagating in the direction of the equilibrium field ($\theta = 0$) has a different velocity from one propagating at an angle to the field so that the medium is anisotropic. For $\theta = \pi/2$ the slow phase speed is null, therefore the slow wave is unable to propagate orthogonally to the magnetic field and neither does the Alfvén wave. On the contrary, the fast wave reaches its maximum speed. For typical physical conditions in the solar corona $v_{\rm A} \gg c_{\rm s}$. In this limit Equation (1.51) reduces to $\omega^2 \approx k^2 c_{\rm s}^2 \cos^2\theta$ for the slow wave and to $w^2 \approx k^2 v_{\rm A}^2$ for the fast wave. Therefore, in the solar corona, the slow wave is essentially an acoustic wave that is forced to travel along the magnetic field direction, and the fast wave is an isotropic magnetic wave.

The general nature of Alfvén and magnetoacustic waves derive from the study of uniform mediums. However, many solar plasma structures present a non-uniform character. A strongly structured atmosphere presents different features that cannot be explained by the analysis of uniform mediums. The simplest structured medium consists of two uniform media with different physical parameters, that are joined at a single interface. The interaction between the two uniform plasmas takes place at the interface throughout a new kind of waves, called surface waves. A deep study of surface waves is out of the scope of this Thesis, however this new type of MHD waves is crucial for the study of the damping of prominence oscillations due to resonant absorption.

Resonant absorption

This is an adiabatic process, namely not related to any physical loss of energy, but rather to transfer of energy from the global transverse mode of oscillation to local Alfvén modes in

non-uniform plasmas. First studies of resonant damping of MHD surface waves are based on solving the governing differential equation for linear motions in a single interface medium (slab geometry) consisting of two uniform regions separated by a continuous profile (Sedláček 1971; Rae & Roberts 1981; Lee & Roberts 1986; Hollweg & Yang 1988). The governing equation can be expressed, for example, as follows (see Section 4.5 of Roberts 2019):

$$\frac{d}{dx}\left[\rho_0\left(x\right)\left(k_z^2 v_{\mathrm{A}}^2\left(x\right)-\omega^2\right)\frac{du_x}{dx}\right]=\rho_0\left(x\right)k_z^2\left(k_z^2 v_{\mathrm{A}}^2\left(x\right)-\omega^2\right)u_x. \tag{1.52}$$

The layer of inhomogeneity that joins the two uniform regions can vary in x in terms of density and/or of the Alfvén speed. In general, solutions of the initial value problem show that the system has a frequency $\omega=\omega_{\mathrm{R}}+i\omega_{\mathrm{I}}$, where ω_{R} is the frequency of motion and the imaginary part ω_{I} is related to the damping time as $t_{\mathrm{d}}={}^{1}\!/_{\omega_{\mathrm{I}}}$. For a lineal transitions of density and Alfvén speed,

$$\omega=k_z c_{\mathrm{k}}+i\,\frac{\pi}{4}lk_z\frac{\rho_0\rho_{\mathrm{e}}}{\left(\rho_0+\rho_{\mathrm{e}}\right)^2}\frac{v_{\mathrm{Ae}}^2-v_{\mathrm{A}}^2}{c_{\mathrm{k}}^2}k_z c_{\mathrm{k}} \tag{1.53}$$

where $c_{\mathrm{k}}=\sqrt{\frac{\rho_0 v_{\mathrm{A}}^2+\rho_e v_{\mathrm{Ae}}^2}{\rho_0+\rho_{\mathrm{e}}}}$ is the kink speed, l is the transition layer width, and the subscripts 0 and e refer to each side of the slab.

A similar problem of damping of transverse waves in prominences is discussed from the viewpoint of a cylindrical geometry (Sakurai et al. 1991; Ruderman & Roberts 2002; Goossens et al. 1992; Arregui et al. 2008). The damping time divided by period ($P=2\pi/\omega_{\mathrm{R}}$), beyond the thin tube thin boundary approximation, can be written as (e.g. Equation (3) of Arregui et al. 2008)

$$t_{\mathrm{d}}/P=F\frac{a}{l}\frac{\chi+1}{\chi-1}, \tag{1.54}$$

where $\chi={}^{\rho_{\mathrm{f}}}\!/_{\rho_{\mathrm{c}}}$ is the filament/corona density contrast, a the radius of the flux tube, l the thickness of the transition layer, and F is a numerical factor that depends on the variation of the density in the transition layer. The resonant damping rate that appears in the mathematical derivation should not be considered as an actual attenuation that involves some kind of energy dissipation and so total energy is conserved, but it has to be physically understood as the timescale in which the energy of the global mode is transferred to the localised Alfvén waves (Soler & Terradas 2015). The damping time is inversely proportional to the width of the transition layer so that structures with wider transition regions attenuate more rapidly, or in other words, the efficiency of resonant absorption increases as the non-uniform layer gets thicker. Also, the damping time decreases when the density contrast is increased.

The mode conversion takes place inside the inhomogeneous transition layer. The energy transference is most efficient where the transverse mode frequency matches the local Alfvén frequency, that is the resonance surface. Due to the energy conversion, the global oscillation gradually loses its energy, and its amplitude is attenuated in time. On the other hand, the amplitude of the Alfvén modes increases at the resonant layers where the energy conversion takes place. The process of resonant absorption is linked with phase mixing. The energy transport of the global kink motion towards the non-uniform boundary of the flux tube

generates small spatial scales by phase mixing. Soler & Terradas (2015) investigated the generation of small scales in non-uniform solar magnetic flux tubes due to phase mixing. The process of phase mixing occurs because in transversely non-uniform to the magnetic field direction plasmas, the Alfvén frequency is spatially dependent. Due to this fact, Alfvén waves propagating in adjacent magnetic surfaces become more and more out of phase as time progresses. As a consequence of the mixing of phases, a continuous decrease of the spatial scale of the wave appears across the magnetic field.

1.4 Gravitational instabilities

A question that immediately arises regarding solar prominences is how they can be suspended against gravity above the photosphere for long periods. This issue has lead to the development of theoretical prominence models that include magnetic dips where the gravity force projected along the field lines is zero. One analytical example of such equilibrium configurations is the previously explained H&A model. Other examples were developed by Fiedler & Hood (1992) and de Bruyne & Hood (1993). Later, equilibrium models in flux rope configurations were obtained by Low & Zhang (2004), Petrie et al. (2007), and Blokland & Keppens (2011). More recently, numerical equilibria have been achieved through relaxation processes by solving the time dependent MHD equations in 2D (Hillier & van Ballegooijen 2013; Terradas et al. 2013; Luna et al. 2016b). 3D stable magnetic configurations with dips have been numerically investigated by Terradas et al. (2015a, 2016) and Adrover-González & Terradas (2020) (see Chapter 2 of the present Thesis). In the latter three works the presence of dips was not crucial for the stability of the prominence. However, it seems that there is the common idea in the solar community that threads/blobs automatically fall along the field lines because of gravity force and that if threads are suspended it is because of magnetic dips. However, this is not completely true because the line-tying effect at the photosphere can produce a pressure increment along the magnetic field lines that is able to sustain extra mass. This has also been investigated numerically in some detail in a magnetic arcade configuration by Kohutova & Verwichte (2017b) (see also the former numerical experiments of Mackay & Galsgaard 2001, in a vertical magnetic field).

One characteristic of the Hood & Anzer (1990) model is the fact that the equilibrium is in general unstable to lateral displacements, meaning that the dense and cold part of the prominence body tends to fall along magnetic field lines essentially due to the gravity force (see also the numerical experiments of Kohutova & Verwichte 2017b). This was demonstrated in the stability analysis of de Bruyne & Hood (1993) who found that the model is only stable for sufficiently low prominences. Therefore, the presence of magnetic dips in the configuration is not a warranty for stability. However, Longbottom & Hood (1994), who included a more realistic magnetic shear angle that changes with height into the H&A model, found that a strong shear gradient in the magnetic field near the base of the filament provides a stabilizing effect on prominences with realistic heights. The instability of the H&A model is going to be addressed in Chapter 3. On the contrary, in the magnetic configuration studied numerically in Terradas et al. (2013) the gravitational instability reported in the Hood & Anzer (1990) model did clearly not take place. At first glance, this instability may seem to be directly related to magnetic buoyancy, a phenomenon that has been investigated in great detail by Parker (1979). But indeed it turns out that it is not related to this kind of process since

it also appears in the absence of fluctuations in the magnetic field, hence, the instability is purely gravitational. This is the main motivation of Chapter 4, namely to understand the reasons for gravitational instability in a global sense, and not necessarily under the presence of magnetic dips. This effect, the role of magnetic dips on the stability properties, is investigated in detail in Chapter 5 of this Thesis.

Part I

Numerical simulations

Chapter 2

3D numerical simulations of oscillations in solar prominences [1]

2.1 Introduction

Solar prominence (or filament) oscillations have been the subject of study for decades. The first detection of a winking filament dates back to 1930 (see Hyder 1966). Since then, diverse researches have aimed at establishing theoretical models that explain the examined oscillations. Observations together with the theoretical models have allowed us to expand our knowledge about solar prominences and have facilitated, for example, the estimation of physical parameters that are difficult to measure, such as the minimum magnetic field strength that supports these plasma structures, or the radius of the curvature of magnetic dips (R) (Ballester 2014; Luna et al. 2014).

The observational and theoretical studies of oscillations in filaments are corroborated by numerical simulations. Single 1D threads formed in magnetic flux tubes with a concave upwards shape where plasma oscillates have been studied by several authors. Luna & Karpen (2012) studied large amplitude longitudinal oscillations in 47 independent threads. They found that the main restoring force is the projected gravity along the magnetic field, and that the periodicity of longitudinal oscillations depends on the radius of the curvature of the magnetic dip following the pendulum model (see Equation (1.2)). Zhang et al. (2012) used 1D radiative hydrodynamic simulations that almost reproduced the periodicity of longitudinal oscillations in threads with magnetic dips observed on February 8th 2007. Zhang et al. (2013) carried out a parametric survey to investigate the behaviour of longitudinal oscillations for different filament dimensions and triggering mechanisms. They found that the swaying motion is not determined by the disturbance type and reasserted that the longitudinal oscillations follow the pendulum model. They also found that in addition to the gravity force, the pressure gradient contributes to the restoring force for short threads.

In addition to 1D simulations, 2D numerical studies of oscillations in prominences have been carried out too. Some of these works focussed on studying the evolution of cold and

[1] This chapter is based on: Adrover-González, A., Terradas, J.; 2020, *3D numerical simulations of oscillations in solar prominences*, Astronomy and Astrophysics, 633, A113.

dense plasma structures embedded in an isothermal stratified atmosphere permeated by a dipped arcade magnetic configuration. Based on this method, Terradas et al. (2013) analysed the evolution of the density distribution together with other variables such as the involved forces or the velocity field during the relaxation process of the non-equilibrium initial configuration. Then, when the prominence was in equilibrium, they studied the behaviour of induced vertical, longitudinal, and Alfvén waves solving the linearised MHD equations. For validating purposes, Luna et al. (2016b) reproduced non-linear numerical simulations of large amplitude longitudinal oscillations in a nearly equilibrium configuration. They found that the pendulum model is robust even in the range of short prominence field lines. In addition to this type of models, Kraśkiewicz et al. (2016), based on the Pikelner model, studied the dynamics of a prominence perturbed by a pressure disturbance, and Zhang et al. (2019) analysed 2D non-adiabatic MHD simulations of longitudinal oscillations.

To reproduce more realistic situations, more complex 3D MHD numerical simulations are required, but so far, only few 3D studies have analysed prominence oscillations. Terradas et al. (2016) and Zhou et al. (2018) carried out simulations of prominences embedded in magnetic flux ropes. While Terradas et al. (2016) focussed their study on the evolution of the density profile for different resolutions and magnetic twist during the relaxation process and in the development of Kelvin-Helmholtz instabilities, Zhou et al. (2018) investigated the dynamics of longitudinal, vertical, and horizontal transverse oscillations triggered by velocity disturbances. The magnetic flux rope geometry is the most widely accepted filament model because it aligns the longitudinal filament axis along the magnetic field lines. However, the magnetic arcade configuration with a curtain-like prominence has not yet been used in 3D numerical simulations of oscillations in prominences.

The numerical studies reviewed in this section made an effort to clarify the nature of the attenuation. Luna & Karpen (2012) proposed that the main damping mechanism for their model is the accretion of mass onto the threads during prominence formation. Zhang et al. (2012) suggested that the non-adiabatic terms are responsible for the attenuation. They analysed the importance of radiative loss and thermal conduction and concluded that in their thread model, the first term is responsible for the damping time ($t_{\rm d}$). Zhang et al. (2019) studied the non-adiabatic effects in the attenuation of longitudinal oscillations in detail and found that, on the one hand, these processes are the primary agent that dissipates the oscillations, but on the other hand, wave leakage plays an important role in dissipating the kinetic energy too. Terradas et al. (2016) have shown in their model that the attenuation of the vertical transverse oscillations is produced by resonant absorption, although Kelvin-Helmholtz instabilities could also provide a mechanism to attenuate the prominences. Despite these attempts to establish attenuation mechanisms, numerical studies caution that part of the damping might be caused by computational effects such as numerical viscosity or dissipation. The numerical damping complicates the study of the attenuation mechanisms, and for this reason, many studies neglect the attenuation problem. While for longitudinal oscillations the non-adiabatic processes have been analysed in many studies, resonant absorption in 3D simulations of transverse oscillations requires a deeper study.

Different models have been used to compare analytical expressions to the transverse simulated periods. For example, Terradas et al. (2013) and Zhou et al. (2018), used in their simulations of vertical oscillations the slab and string model of Joarder & Roberts (1992b),

respectively, and obtained large differences between the analytical and the numerical results. Nevertheless, both studies obtained better correlations with the results of Díaz et al. (2001) even though they used a 2D model.

The main aim of this chapter is to perform a 3D numerical study of oscillations in a curtain-shaped prominence permeated by a magnetic arcade that supports the dense and cool plasma against gravity. The magnetic configuration is based on the model proposed by Kippenhahn & Schlüter (1957). Unlike other works, in which the prominence mass is suspended above the photosphere, we anchored the plasma to the bottom boundary of the computational domain, which represents the photosphere in our model. Large-scale filament properties show that the cool plasma of many prominences joins the chromosphere, and possibly the photosphere, through the filament barbs (Parenti 2014). Extensive filaments with a few points of contact with the surface (Hedgerow prominences) are the most common type (Zirin 1998; Engvold 2015). In addition, Shen et al. (2014b) observed transverse oscillations above the solar limb and suggested that the body oscillated as a rigid body with one end anchored on the Sun. However, this structure has not been investigated numerically so far. For these reasons, we considered that our model is a good approximation to study this rich prominence type. The aim is to compute the period and the damping time for vertical and longitudinal/transverse horizontal motions triggered by velocity disturbances for different mass distributions. The primary initial configuration is described in Section 2.2 and the numerical aspects are explained in Section 2.3. The computed results are displayed in Section 2.4. Conclusions and discussion are summarised in Section 2.5.

2.2 Initial reference set up

To numerically study the oscillations in prominences, an isothermal stratified background atmosphere has been configured as in Terradas et al. (2015a). The coronal density profile is expressed as $\rho_c = \rho_0 \exp(-z/\Lambda)$, where ρ_0 is the density of the reference level located at the bottom boundary of the computational box $z = 0$. Unlike the works of Zhou et al. (2018) and Zhang et al. (2019), who inserted a temperature transition between the photosphere and the corona, in our model we consider that the level $z = 0$ represents the photosphere and that it is connected to the corona through the magnetic field (Terradas et al. 2013, 2015a).

The pressure scale height is $\Lambda = c_{s0}^2/\gamma g$ and the velocities are normalised to the sound speed $c_{s0} = \sqrt{\gamma p_0/\rho_0} = 166\,\mathrm{km\,s^{-1}}$ for a coronal temperature of 1 MK. The gravity acceleration is $g = 0.274\,\mathrm{km\,s^{-2}}$, the adiabatic index is $\gamma = 5/3$, and the reference length has been chosen to be $H = 10\,\mathrm{Mm}$. The plasma is permeated by an arch-shaped magnetic field, composed of the superposition of two force-free magnetic arcades, see Section 1.3.3. This quadrupolar configuration adds a magnetic dip to the structure in which the depth of the dip varies with height. In Figure 1.7 some magnetic field lines are plotted in the xz-plane. At $x = 0$, the radius of the curvature takes low positive values in the bottom part of the structure and grows until $z = 1.55\,H$, where the field line becomes flat. From this point, the dip is lost and the curvature becomes concave downwards. To avoid high values of the plasma-β parameter ($\beta = 2c_s^2/\gamma v_A^2$), which affect the character of the modes, the point z_X has been located out of the numerical domain as in Luna et al. (2016b). Unlike Terradas et al. (2015a), the magnetic configuration has no shear and the magnetic field is invariant in the y-direction.

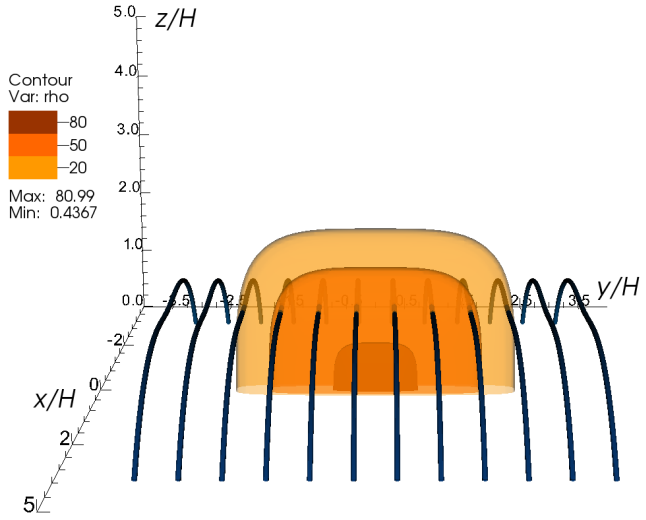

Figure 2.1: Density profile together with some magnetic field lines at $t = 0$. In this plot $n = 4$, $w_x = 0.3\,H$, $w_y = 2.2\,H$, $w_z = 2.6\,H$, and $\rho_{\mathrm{p0}} = 80\,\rho_0$. Density isocontours are normalised to ρ_0.

An increase in shear produces an increase in the horizontal component of the magnetic field, leading to a higher magnetic tension. It also changes the depth and width of the dips so that the magnetic support can be different between sheared and non-sheared structures. The study of oscillations in sheared arcades is beyond the scope of this chapter. To obtain the previously described magnetic configuration, the magnetic vector potential is

$$\begin{cases} A_x = 0, \\ A_y = \frac{B_0}{k_1}\cos(k_1 x)\exp[-l_1(z-z_0)] - \frac{B_0}{k_2}\sin(k_2 x)\exp[-l_2(z-z_0)], \\ A_z = 0. \end{cases} \tag{2.1}$$

For the reference simulation we took $B_0 = 10\,\mathrm{G}$. We chose $k_1 = \pi/2L$ and $k_2 = 3k_1$ to be the parameters related to the lateral extension of the arcades, $2L$ is the width of the whole structure, l_1 and l_2 are measures of vertical magnetic scale height, and $z_0 = -0.2\,H$ is equal to z_X. The relation l_1/k_1 is related to the shear of the magnetic field lines. In this work the shear is null, implying that $l_1/k_1 = 1$, and the value for l_2 is set by the constraint $k_1^2 - l_1^2 = k_2^2 - l_2^2$. The magnetic field is $\mathbf{B} = \nabla \times \mathbf{A}$ and it is given by Equation (1.38).

The mass deposition is artificial and instantaneous because we did not study the prominence formation process here (see Mackay et al. 2010, for a summary of prominence formation models). The deposition maintains the gas pressure at the same level. The density profile consists of a curtain-shaped mass distribution expressed as

$$\rho_{\mathrm{p}} = \rho_{\mathrm{p0}} \exp\left[-2((x/w_x)^n + (y/w_y)^n + (z/w_z)^n\right]. \tag{2.2}$$

The term n determines the width of the prominence-corona transition region (PCTR) (in this work, $n = 4$ by default). The width, the length, and the height of the curtain are chosen to be $w_x = 0.3\,H$, $w_y = 2.2\,H$, and $w_z = 2.6\,H$, respectively, and the density contrast

between the corona and the core of the prominence has a value of $\rho_{p0}/\rho_0 = 80$. With these characteristics and by considering that the prominence density is $5.2 \times 10^{-14}\,\mathrm{g\,cm^{-3}}$, the total mass of the filament is $1.6 \times 10^{14}\,\mathrm{g}$. The feet of the prominence are anchored to the base of the domain box, which represents the base of the corona, therefore the motion is subjected to this condition. The density profile is located centred in the computational box and the filament spine is aligned with the y-coordinate, hence, the magnetic field lines cross the prominence transversely. This configuration is not the most widely used one by authors who accept that in most cases the dense plasma is almost aligned along the magnetic field lines. Observations demonstrate that the angle between the magnetic field lines and the prominence spine is quite small and has a maximum at around 25^{o} (Tandberg-Hanssen 1995). However, for simplicity, we decided to use the present configuration as a preliminary step before sheared arcades are analysed. In Figure 2.1 the described density profile is represented at $t = 0$ including some selected magnetic field lines.

2.3 Numerical aspects

The ideal MHD equations we solved are given by Equations (1.10)-(1.13). The code we used to solve this equations is the Pencil Code[2] which is a publicly available model that uses sixth-order finite-difference schemes. High-order derivative schemes, such as the one used in the Pencil Code, reduce the numerical dissipation, but in order to obtain consistency in numerical solutions, the code needs to add small amounts of diffusion to damp out the modes near the Nyquist frequency (Brandenburg 2003). For this reason we have introduced a simplified second-order hyperviscosity term (see Haugen & Brandenburg 2004) and a shock viscosity term in the equation of motion. We did not use artificial viscosity in the other equations. The hyperviscosity is proportional to a diffusion coefficient that should be as small as possible but sufficiently large to reduce the wiggles in the results. In addition, to avoid wiggles, we used fifth-order upwind derivatives for the advection terms $\mathbf{v}\cdot\nabla \ln\rho$ and $\mathbf{v}\cdot\nabla s$. To calculate the time step we applied a third-order Runge-Kutta scheme.

The Pencil Code uses three layers of ghost points to implement boundary conditions. In this work, closed boundary conditions were applied (see Terradas et al. 2016), which means that line-tying conditions were imposed at all boundaries of the computational box. A line-tying boundary condition sets the three components of the velocity equal to zero, the normal component of the magnetic field is kept constant, and spatial derivatives of the density and the entropy variables are equal to null. This condition imposed at the bottom boundary is crucial to mimic the purely reflecting conditions of the photosphere and to obtain the magnetic support. Since the Pencil Code uses the magnetic vector potential instead of the magnetic field, to fix the magnetic component perpendicular to the boundary, we applied to the three components of $\mathbf{A}$ the condition of antisymmetry relative to the boundary value that eliminates the second derivative of $\mathbf{A}$. The numerical domain is a box of $180 \times 144 \times 90$ mesh points in which the dimensions of the box were chosen to be 100 Mm in the x-direction, 80 Mm in the y-direction, and 50 Mm in the vertical component. Thus, we were able to impose an equidistant grid with a grid size of 0.556 Mm.

[2] http://pencil-code.nordita.org/

2.4 Results

2.4.1 Relaxation process

As was already mentioned in Section 2.2, the mass deposition is instantaneous. The prominence plasma breaks the initial equilibrium and then starts to oscillate vertically. Initially, the force-free magnetic condition implies an equilibrium between the magnetic pressure and the magnetic tension. Additionally, the gas pressure force counteracts the gravitational force, thus, the entire system is stable. However, when the prominence is introduced, the system loses its balance and the gravity force pushes the structure downwards. The top left panel of Figure 2.2 shows the vertical component of the forces at $x = 0$ and $y = 0$ as a function of height at $t = 0$, once the prominence mass is introduced. It shows that, at the beginning of the simulation, the magnetic tension (grey curve) counteracts the magnetic pressure (dashed curve), but gravity (solid line), in the presence of the prominence body, exerts a force pointing downwards and so the pressure gradient (dot-dashed curve) does not counteract. Immediately, the plasma deforms the field lines, increasing the depth of the magnetic dips.

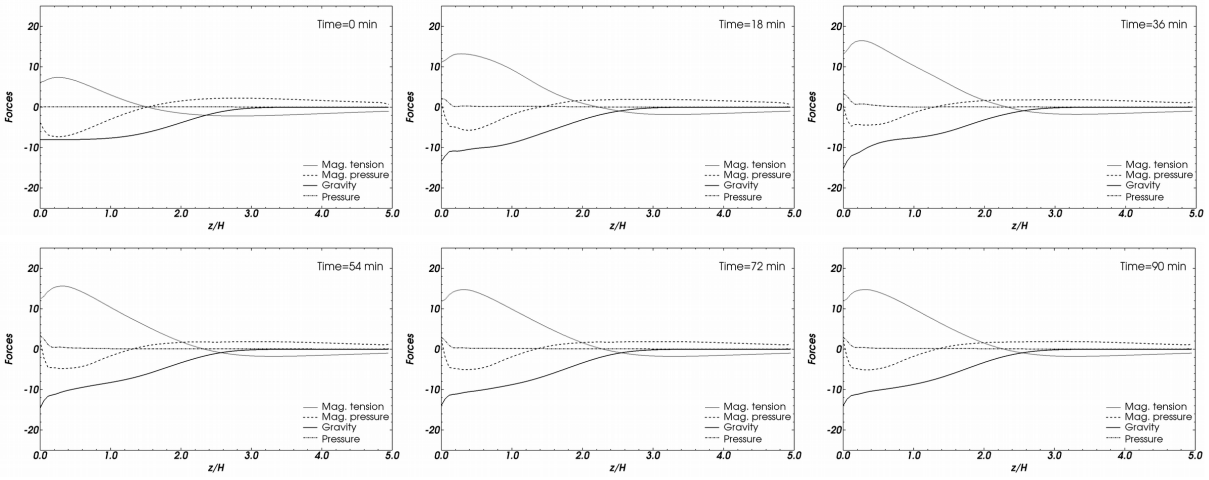

Figure 2.2: Time evolution of the vertical component of the forces at $x = 0$ and $y = 0$ as a function of height. The forces are magnetic tension (grey curve), magnetic pressure (dashed curve), gravity (solid curve), pressure gradient (dot-dashed curve). Forces are normalised to $\rho_0\, c_{s0}^2/H$.

In the top panel of Figure 2.3 we show the final state of the field lines (blue solid curves) compared with the initial state (black dashed curves). This distortion implies an increase in the z-component of the magnetic tension (and to a lesser extent, the magnetic pressure) in such a way that it counteracts the movement, restoring the prominence upwards. After an evolution of approximately 80 min, the Lorentz force almost balances the gravity force (see the time evolution of the forces in Figure 2.2).

The total mass of the system remains practically constant although there is a spatial redistribution. The density distribution of the final equilibrium state at $t = 90$ min is shown in the

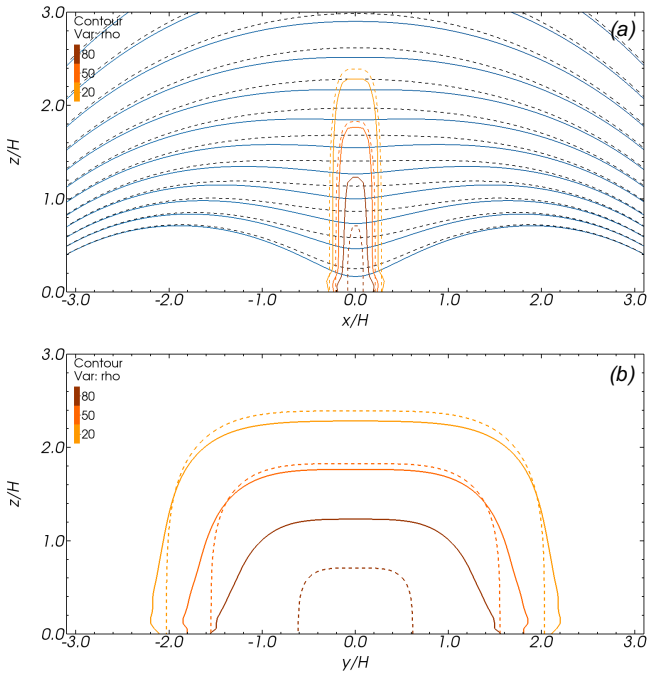

Figure 2.3: Density distribution of the final equilibrium state at $t = 90\,\mathrm{min}$. Top panel: Density isocontours and magnetic field lines in the plane $y = 0$. Bottom panel: Density isocontours in the plane $x = 0$. Dashed lines correspond to the initial reference set-up, and solid lines show the final equilibrium state at $t = 90\,\mathrm{min}$. Density is normalised to ρ_0.

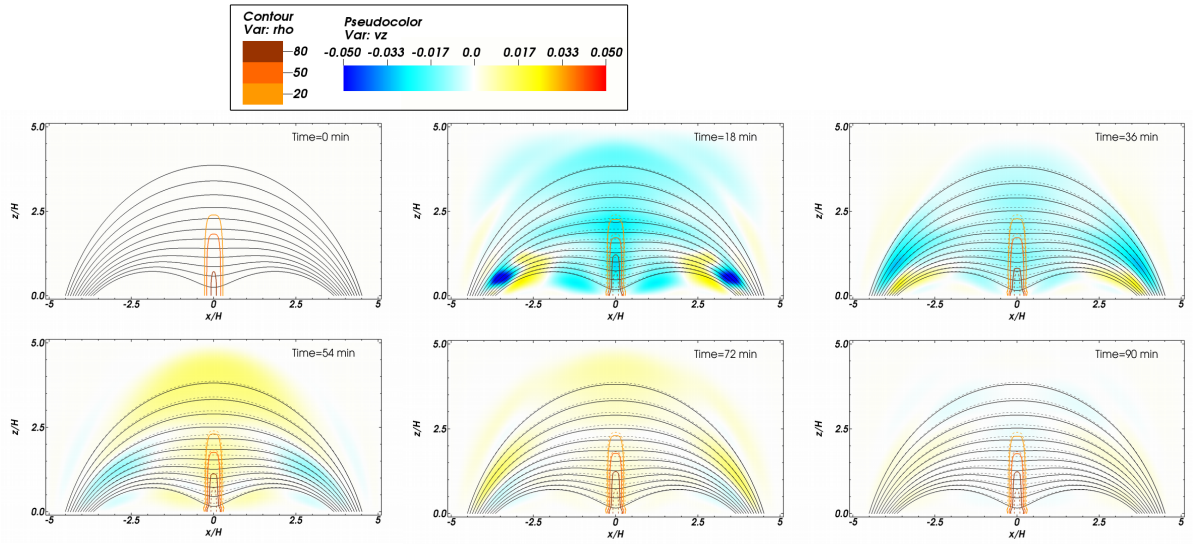

Figure 2.4: Time evolution of the density, v_z and the magnetic field lines for the relaxation process of the reference simulation in the xz-plane at $y = 0$. The dashed lines represent the initial state. v_z is normalised to $c_{\mathrm{s}0}$ and density to ρ_0.

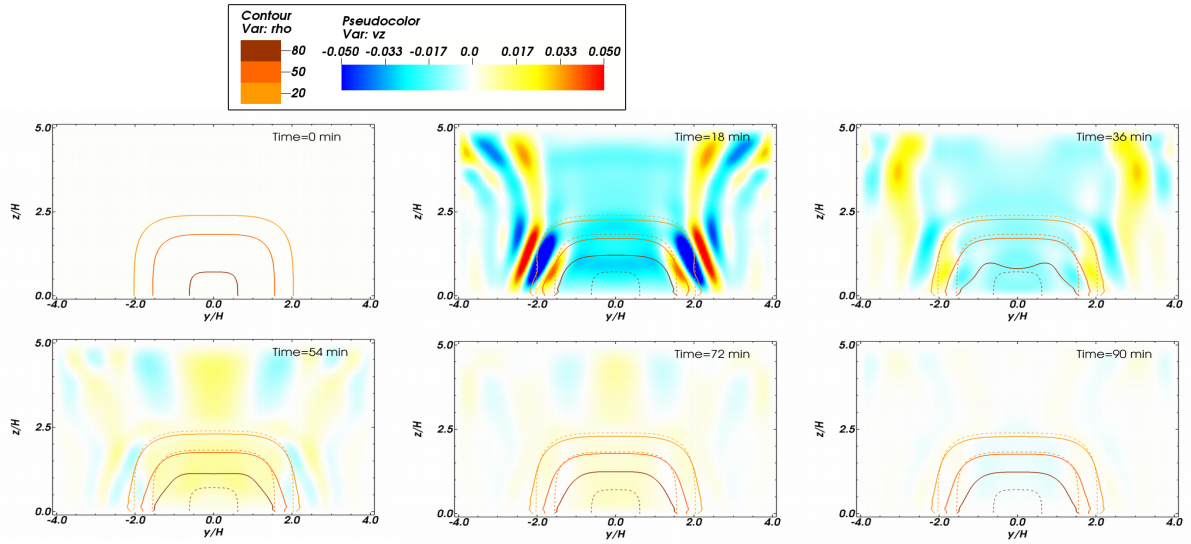

Figure 2.5: Time evolution of the density and v_z for the relaxation process of the reference simulation in the yz-plane at $x = 0$. The dashed lines represent the initial state. v_z is normalised to c_{s0} and density to ρ_0.

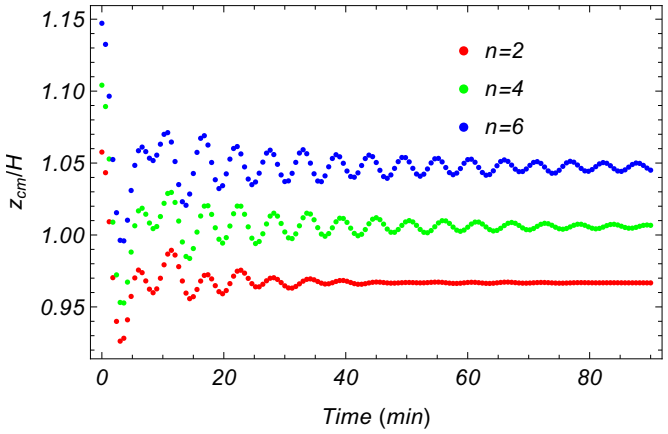

Figure 2.6: Time evolution of the z-component of the centre of mass for $n = 2$ (red), $n = 4$ (green) and $n = 6$ (blue). The density average has been computed for a delimited region ($x \in [-0.5\,H, 0.5\,H], y \in [-3\,H, 3\,H], z \in [0, 3.5\,H]$).

top and the bottom panels of Figure 2.3. In the top panel we observe that the prominence widens slightly in the x-direction near its base, where the plasma gathers. To compensate for the accumulation of mass at the base, the filament narrows at the top and reduces its height. In the bottom panel we find that in the y-direction the redistribution of mass is more noticeable, especially in the inner layers of the prominence, where as a result of the accumulation of plasma, the isocontour $\rho = 80\,\rho_0$ expands. For a more detailed tracking of the density redistribution during the relaxation process of the reference simulation, we show in Figures 2.4 and 2.5 the temporal evolution of the density and the vertical component of the velocity v_z in the xz and yz-planes, respectively. Figure 2.4 also shows the evolution of

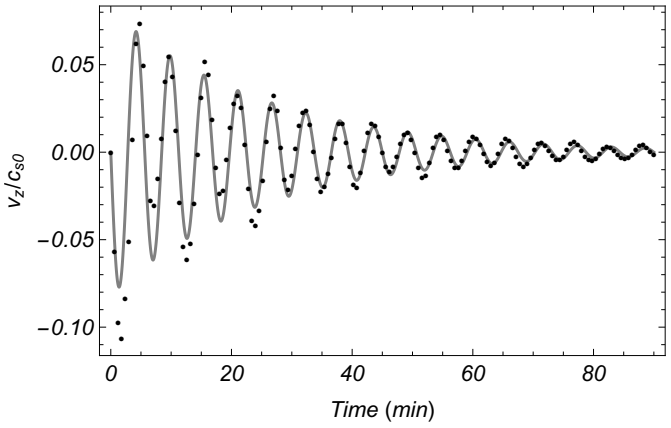

Figure 2.7: v_z as a function of time for the relaxation process at a fixed point $(0, 0, 1.3\,H)$. The dots represent the values obtained from the numerical simulation and the continuous grey curve is the fitting result based on Equation (2.3).

field lines of the magnetic arcade.

The evolution of the z-component of the centre of mass is represented in Figure 2.6. To suppress interactions with the background, the centroid was averaged from a delimited box that only included the prominence body. The green dotted line corresponds to the reference simulation, and, initially, the centre of mass is located approximately at $z = 1.1\,H$, however, it rapidly drops. After two cycles, the prominence oscillates around a new equilibrium height located at $z = 1.01\,H$. This change in height occurs due to the mass redistribution.

The evolution of the vertical velocity at the point $x = 0$, $y = 0$, $z = 1.3\,H$ is represented in Figure 2.7 (dotted line). At the beginning of the simulation, the system is completely at rest, but the prominence body immediately drops, increasing the z-component of the velocity (v_z), which rapidly reaches its maximum value. Approximately at $t = 3.5\,\mathrm{min}$, the speed reaches positive values, which indicates that the prominence begins to ascend towards its original position. This periodic motion is repeated approximately sixteen times for about 90 min. Figure 2.7 shows that the amplitude of the oscillations decreases with time. The observations indicate that the movement describes an attenuated oscillation. We can fit an exponentially decayed sine curve with respect to time, expressed as

$$f = f_0 \sin(\omega\, t)\, \exp(-t/t_\mathrm{d})\ , \tag{2.3}$$

where f_0 is the signal amplitude, ω the frequency, and t_d is the damping time. For the reference simulation we obtained a period of $P = 2\pi/\omega = 5.6\,\mathrm{min}$, a damping time of $t_\mathrm{d} = 25.1\,\mathrm{min}$, and a velocity amplitude of $f_0 = -0.082\,c_{\mathrm{s0}}$. We represent the fitted curve in Figure 2.7 as a solid line.

As in Terradas et al. (2015a), we represent the evolution of v_z in a yz-slice at $x = 0$ (see Figure 2.8). The same result that has been shown in Figure 2.7 can be seen in the top panel of Figure 2.8, namely, that at the beginning of the simulation, v_z takes a negative value at the prominence body, describing a downwards movement. Nevertheless, the global evolution is more complex, and the system also develops vertical shear motions at the lateral edges of the prominence. In the first steps of the simulation, the system shows a single wide lateral

strip, but in the bottom panel of Figure 2.8 we observe that at $t = 8.4\,\mathrm{min}$ the number of bands with opposite speed has grown and their width has narrowed. This is clearer in Figure 2.9, where we plot the time evolution of v_z as a function of the y-coordinate at $x = 0$ and $z = 1.3\,H$. At $t = 2.4\,\mathrm{min}$ (solid line) and $t = 8.4\,\mathrm{min}$ (dashed line), we observe the same pattern as in Figure 2.8, and at $t = 14.4\,\mathrm{min}$ (dotted line), we obtain that these shear motions remain localised at the PCTR and that the typical spatial scales have decreased with time. We also clearly see the same velocity distribution in the top middle panel of Figure 2.5. This velocity pattern is generated as a result of resonant absorption, and it is the origin of part of the attenuation. Terradas et al. (2015a) also found this positive/negative velocity pattern in v_z (see Figure 3 of their work) and they associated this behaviour with the process of mode conversion and phase mixing. Our results agree with the resonant absorption process because the energy conversion takes place at the inhomogeneous layer of the prominence, that is, at the sides of the structure in the transverse direction with respect to the field lines and the direction of motion; in this case, the y-edges. This process is also characterised by the decrease of the typical spatial scales of the shear stripes with time. It is important to mention that the velocity amplitude of the positive/negative bands attenuates with time as Figure 2.5 shows.

The studies of the resonant absorption as a mechanism for the damping of filament oscillations are usually based on simple models of magnetic flux tubes (see, e.g. Arregui et al. 2008; Soler et al. 2009b; Antolin et al. 2015). In these works, the damping time of the fast kink waves caused by the resonant absorption process depends on the width of the PCTR. To study the dependence of the attenuation on the PCTR, the relaxation process was simulated by modifying the density profile but keeping the total mass constant, so that for $n = 2$, we have $\rho_{\mathrm{p0}} = 144\,\rho_0$, and for $n = 6$, we have $\rho_{\mathrm{p0}} = 63.7\,\rho_0$. The prominence with the term $n = 6$ has the steepest profile, whereas the one with $n = 2$ has the least steep one, so that when n increases, the density slope is stronger and leads to thinner transitions between the core and the corona. In Figure 2.6 the evolution of the centre of mass is plotted for the three different cases. The evolution of the three curves are similar to each other, but we can clearly see that for $n = 6$ (blue curve), the evolution has a softer attenuation and for $n = 2$ (red curve) we obtain the strongest damping. In agreement with Arregui et al. (2008), we obtain that the wider the PCTR, the stronger the attenuation. We are interested in estimating the ratio of the damping time to the period. From the fitted curve of Figure 2.7 we computed t_{d} from the v_z series at a localised point. However, in complex configurations we can detect different attenuation times at distinct points. For this reason, in Figure 2.6 we calculated the time evolution of the spatially averaged density. For the relaxation process, to calculate the damping time of the three signals of Figure 2.6, we first applied an empirical mode decomposition (see Terradas et al. 2004) to decompose the signal and select the first intrinsic mode function. In this way, we subtracted the trend of the centre of mass drop. After this, we obtained a damping per period of $t_{\mathrm{d}}/P = 1.9$ for $n = 2$, $t_{\mathrm{d}}/P = 3.7$ for $n = 4$, and $t_{\mathrm{d}}/P = 5.9$ for $n = 6$.

To extend the study of the relaxation process, we studied its evolution for a range of values of the filament width, the density contrast, and the magnetic field strength. The results are shown in Figure 2.10. First, we investigated the dependence of the period on w_x. We varied the width of the prominence from $0.25\,H$ to $0.5\,H$, while we used the reference values for the other parameters. When the width is doubled the total mass is multiplied by a factor

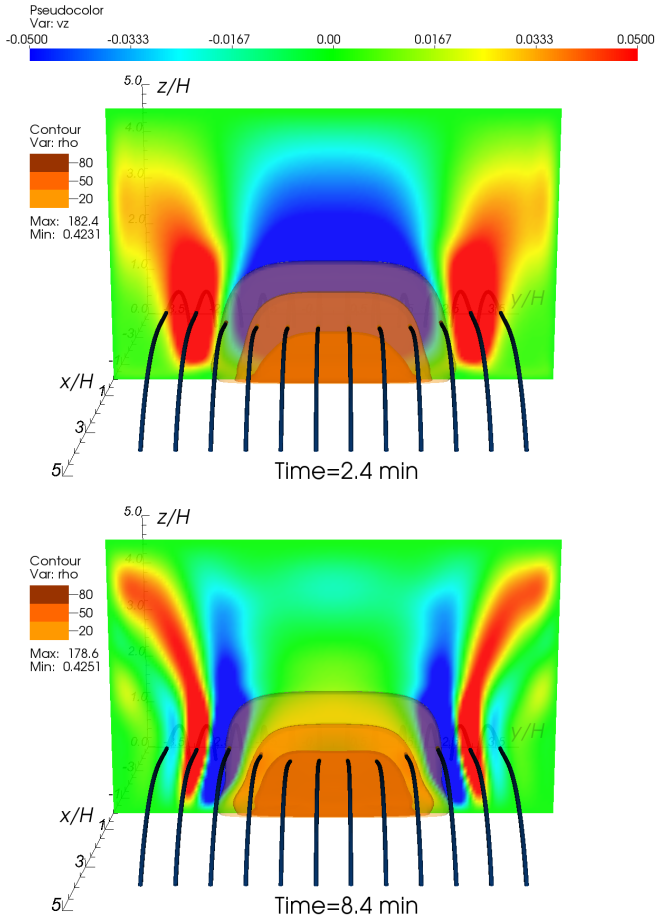

Figure 2.8: Time evolution of the density, v_z and the magnetic field lines for the relaxation process. v_z is represented in the yz-plane at $x = 0$ as a 2D slice. The initial configuration for this case is shown in Figure 2.1. v_z is normalised to c_{s0} and density to ρ_0.

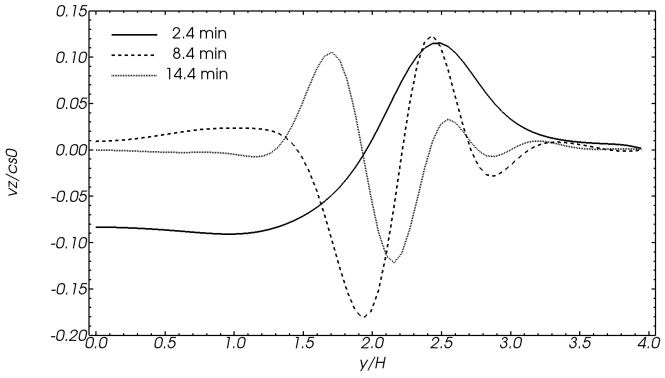

Figure 2.9: v_z as a function of y ($x = 0$, $z = 1.3H$) at $t = 2.4\,\mathrm{min}$ (solid line), $t = 8.4\,\mathrm{min}$ (dashed line) and $t = 14.4\,\mathrm{min}$ (dotted line).

of two. To compute the periodicity of the oscillations, we fitted the results for the different time series of v_z with Equation (2.3) following the same procedure as used in the reference

process. The curtain with the widest width, and therefore with the greatest total mass, shows a higher initial z-velocity amplitude and a greater fall of the centroid into the new equilibrium point. The top panel of Figure 2.10 indicates that the oscillation period varies with the prominence width. We obtained that the wider the prominence, the longer the period.

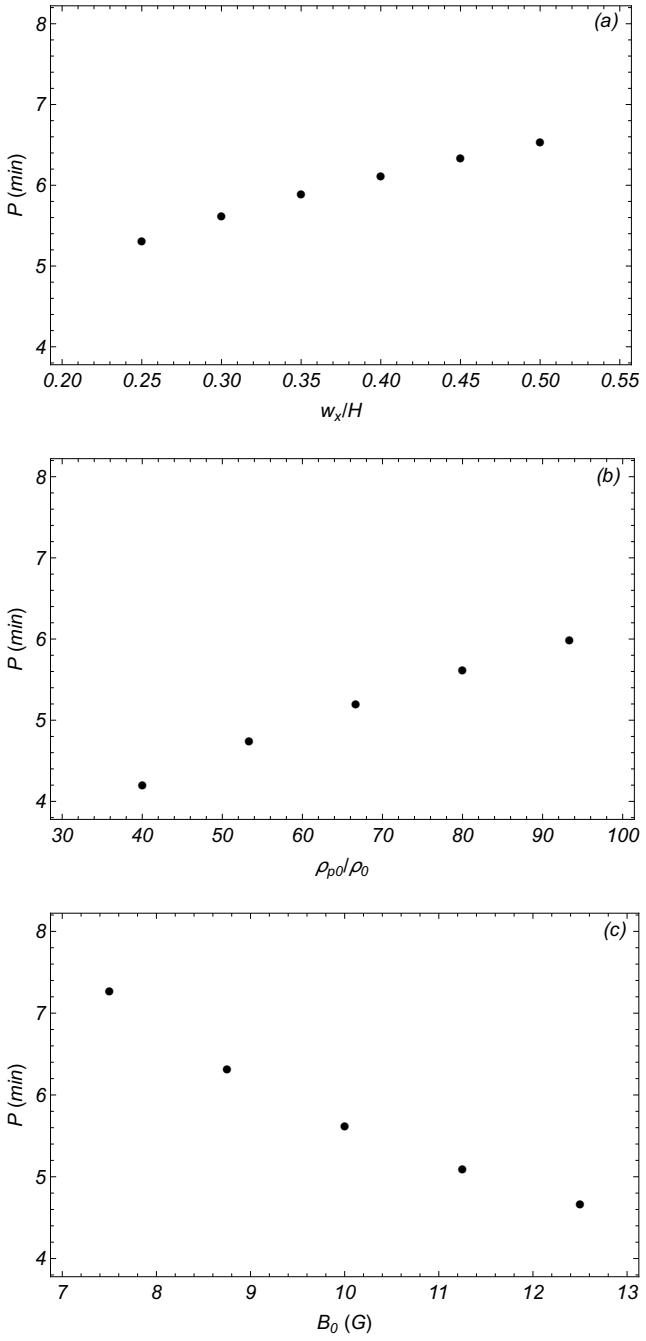

Figure 2.10: Scatter plots of the period of oscillation P during the relaxation process as a function of w_x (top panel), ρ_{p0} (middle panel) and B_0 (bottom panel). The values of P were obtained from the fitted curve based on Equation (2.3) for the evolution of v_z at a fixed point $(0, 0, 1.3\,H)$.

We also studied the dependence of the periodicity on the prominence mass by varying $\rho_{\rm p0}$ and keeping the reference values of the other variables. Now, the total mass of the parametric survey ranges from 7.9×10^{13} g to 1.8×10^{14} g. The highest mass prominence suffers the greatest drop into the new equilibrium point and has the largest z-velocity amplitude. In the middle panel of Figure 2.10 we can see an increase in the period with total mass. In the top and middle panels we observe an almost lineal dependence of the period on the other two parameters. The parameter values were chosen in a way that the curtain with widths of $0.25\,H$ and $0.35\,H$ would have the same total mass as the curtain with $\rho_{\rm p0} = 66.67\,\rho_0$ and $\rho_{\rm p0} = 93.33\,\rho_0$, respectively. Figure 2.10 shows that configurations with the same total mass have practically the same oscillation period.

The last parameter we modified is the magnetic field strength. We varied B_0 so that the maximum Alfvén speed ranges from $13.3\,c_{\rm s0}$ to $22.1\,c_{\rm s0}$. Terradas et al. (2015a) analysed the dependence of the relaxation process for a suspended prominence on β. They found that for low β the magnetic field of their configuration is able to keep the prominence suspended. However, for a low magnetic field strength, the dense plasma falls down and finally forms a hedgerow or curtain-shaped prominence. These downward flows, caused by Rayleigh-Taylor instabilities, complicate the dynamics of the system (see also the simulations by, e.g. Hillier et al. 2012a,b; Khomenko et al. 2014b; Popescu Braileanu et al. 2021a,b). Nevertheless, we avoided these flows by anchoring the density enhancement to the computational box. We obtained that for a weak magnetic field, the magnetic tension can hardly maintain the structure so that the material oscillates with a larger amplitude and at a lower equilibrium point. The top panel of Figure 2.10 shows that the period decreases with the magnetic field strength. These results agree with Terradas et al. (2013), who found in their numerical study that for vertical oscillations, the period increases with the total mass and decreases for weaker magnetic field strengths. They also found that the period decreases slightly with the total length of the magnetic field line that crosses the prominence centre.

We analysed the attenuation of the vertical oscillations for the different cases. From the v_z series we obtained that the damping per period $t_{\rm d}/P$ does not vary significantly with width and ranges from 4.4 to 5.2. However, we found that the attenuation depends strongly on $\rho_{\rm p0}$ and B_0. $t_{\rm d}/P$ decreases with $\rho_{\rm p0}$ from 7.9 to 3.7 and increases with B_0 from 2.2 to 7.6. Then instead of analysing the v_z series, we study the centroid, as has been previously explained, and found that no important changes in periodicity or attenuation are observed. This means that, as in Terradas et al. (2008a), the global mode is dominant everywhere inside the prominence and that the damping time is basically the same everywhere.

2.4.2 Longitudinal oscillations

When the dense plasma enters an almost stationary state, we introduce a velocity perturbation in the x-direction in the prominence body to trigger longitudinal oscillations. The perturbation is

$$v_{xp} = v_{x0} \exp\left[-2\left((x/w_{vx})^4 + (y/w_{vy})^4 + ((z - z_{v0})/w_{vz})^4\right)\right]. \tag{2.4}$$

We refer to longitudinal oscillations as the movement along the magnetic field lines. The spatial distribution of the velocity disturbance was defined in such a way that it produces a global motion of the prominence but maintains the filament foot fixed to the photosphere. The

disturbance has a maximum speed of $v_{x0} = 0.05\, c_{s0}$ located at the centre of the prominence at a height of $z_{v0} = 1.3\, H$, and its shape fits the density profile ($w_{vx} = 0.3\, H$, $w_{vy} = 2.2\, H$, and $w_{vz} = 1.1\, H$). In the top panel of Figure 2.11 the evolution of the x-component of the velocity (v_x) at the xz-slice passing through $y = 0$ at the new equilibrium instant $t = 0$ is plotted with some selected density contours and some magnetic field lines.

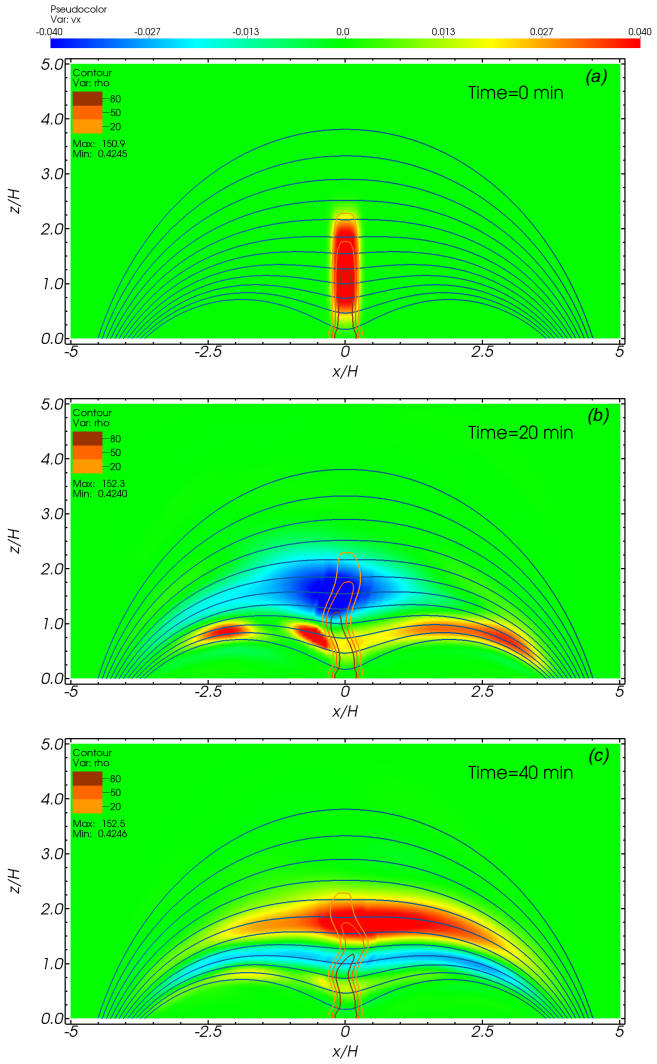

Figure 2.11: Time evolution of v_x at the xz-plane passing through $y = 0$ for the evolution of longitudinal oscillations. The ten blue curves correspond to some selected magnetic field lines. The orange-coloured isocontours represent the density profile. The initial parameters are the same as those in Figure 2.1. v_x is normalised to c_{s0} and density to ρ_0.

Initially, the prominence moves in the direction given by the disturbance. The displacement reaches a different maximum amplitude depending on the perturbation profile. The greatest displacement occurs in the centre of the structure where we located the maximum speed. After the oscillation reaches the maximum displacement, the backward movement restores the motion at a different instant for each height.

The simulation shows that the restoring movement occurs earlier in the lower part of the

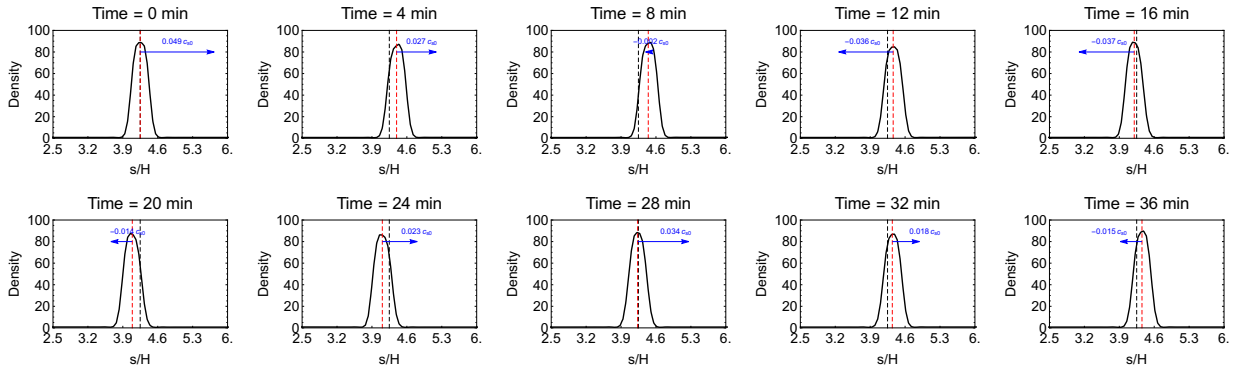

Figure 2.12: Time evolution of the density distribution (solid black line) along a selected magnetic field line. The field footpoint is located at $x = -3.885\,H$. The dashed black line is the half of the field line and the dashed red line is the position of the centre of mass. The blue vector describes v_x of the centre of mass.

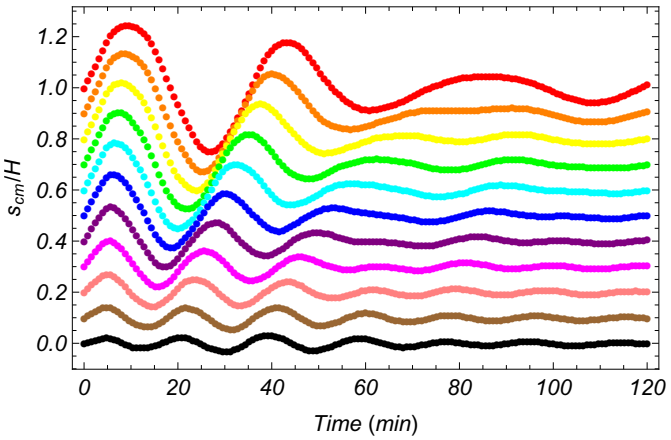

Figure 2.13: Evolution of the centre of mass along eleven selected field lines in the case of longitudinal oscillations. Every dotted curve is shifted by a distance of $0.1\,H$ from the curve below.

structure than in the upper part. This fact causes the motion to describe a serpentine movement that can be seen in the middle and bottom panels of Figure 2.11. We also observe that v_x displays different velocity stripes of opposite sign aligned with the magnetic field lines that cross the prominence body. These positive/negative bands indicate that the body oscillates out of phase. On the whole, the centroid oscillates with a period of $P = 37\,\mathrm{min}$, a damping time of $t_\mathrm{d} = 47.6\,\mathrm{min}$, and a displacement of $f_0 = 0.093\,H$.

To study the dependence of the period on the height and the driving mechanism of the longitudinal oscillations, we compared the results with the pendulum model. Based on Luna et al. (2016b), we selected eleven magnetic field lines located at the central xz-plane of our numerical domain. The position of the centre of mass along each magnetic line (s_cm) was calculated. The left foot position of the selected field lines ranges from $x = -4\,H$ to $x = -3.65\,H$ with an increase of $0.035\,H$. The height of the selected lines at the centre of the prominence varies approximately from $z = 0.3\,H$ to $z = 1.4\,H$ for the reference simulation.

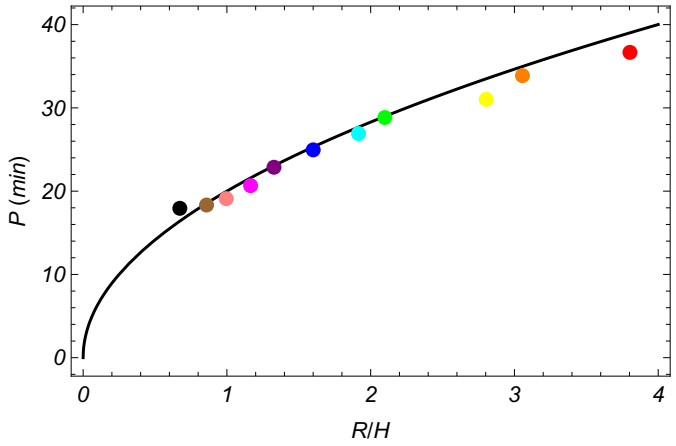

Figure 2.14: Scatter plot of the periods of oscillations P as a functions of the radius of curvature R of the magnetic dips. Each coloured point corresponds to the period obtained from the curves of Figure 2.13 with the same colour. The black solid curve represents the pendulum model based on Equation (1.2).

At these heights all the selected field lines are concave upwards. An overview of the motion along one of the field lines is shown in Figure 2.12, where we display the evolution of the density profile along a magnetic field line. The field footpoint is located at $x = -3.885\,H$. We took this footpoint to have a field line that crosses the prominence body through the centre of mass of the equilibrium state, approximately at $z = 1.1\,H$. In Figure 2.12 s is the coordinate along the tube, starting from the left foot. The red dashed vertical line represents the evolution of the centre of mass (black dashed line displays the centre of mass at $t = 0$), and the blue arrow provides the horizontal component of the velocity v_x at the centre of mass. We see how the prominence oscillates around its original position with a period of approximately 28 min. In Figure 2.13 we show the evolution of the centroid position for the eleven selected lines. Actually, all the dotted lines oscillate around $s_{\rm cm} = 0$, but, for a better visualization, each curve has been displaced from its original position. We calculated the oscillation periods from the time evolution of $s_{\rm cm}$ of each selected field line and represent them in Figure 2.14 as a function of the radius of the field line curvature. To calculate R we ignored its changes during the evolution of the oscillations, and we averaged the different values of the radius along a distance of $0.25\,H$ from the prominence centre. Figure 2.14 shows that the numerical results for the reference simulation agree with the theoretical model expressed by Equation (1.2) (solid line), at least for the reference simulation.

In order to perform a parametric study, we introduced a v_x disturbance in each of the different stationary states obtained in Section 2.4.1, and analysed the periodicity of longitudinal oscillations as a function of w_x, $\rho_{\rm p0}$, and B_0. In Figure 2.15 we show the scatter plots of the oscillation periods as a function of R for the different events. Top, middle, and bottom panels correspond to simulations of different w_x, $\rho_{\rm p0}$ and B_0, respectively. As we showed in Section 2.4.1, the structures with a thinner density distribution, a lower density contrast, and a greater magnetic field strength suffer a smaller fall of their centre of mass during the relaxation process. Consequently, the prominence mass deforms the magnetic field lines less strongly, so the radius of each field line is longer. As a result, in Figure 2.15 we observe that

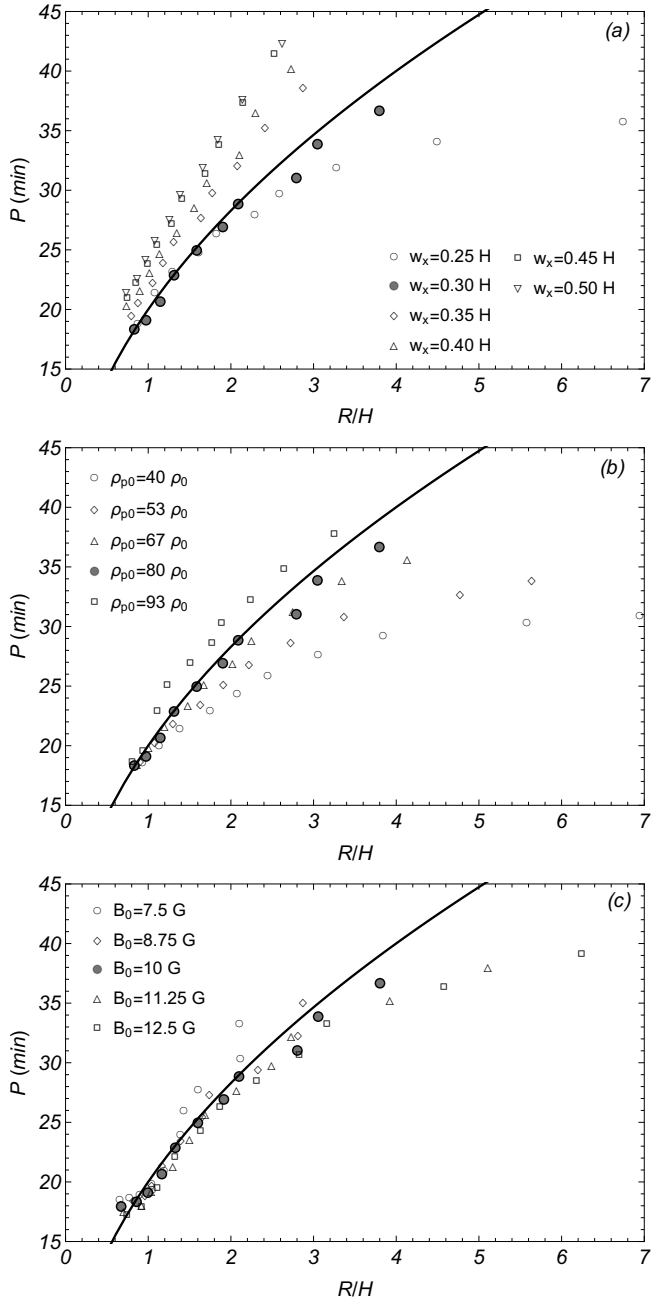

Figure 2.15: Scatter plots of the periods of oscillation in the case of longitudinal oscillations as a function of the radius of curvature of the field lines. The top panel represents the different cases as a function of w_x, the middle panel as a function of $\rho_{\rm p0}$ and the bottom panel as a function of B_0. The filled circles correspond to the reference simulation. Solid line represents Equation (1.2).

the dotted lines for $w_x = 0.25\,H$ (top panel), $\rho_{\rm p0} = 40\,\rho_0$ (middle panel), and $B_0 = 12.5\,{\rm G}$ (bottom panel) reach longer radii for field lines with the same footpoint. In the top panel of Figure 2.15 we show that the period increases with the prominence width. As a result, the computed results become different from those of the pendulum model. This result

agrees with Zhang et al. (2013). They reported a numerical study of a parametric survey of longitudinal oscillations and found that P increases slightly with the width of the thread. The authors proposed that the dependence of the period on the prominence width arises because in shorter threads the gas pressure gradient increases, contributing to the restoring force and shortening the periodicity. In the middle panel of Figure 2.15 we also show that the oscillation period increases with the density contrast of the structure. In agreement with this result, Terradas et al. (2013) found that higher mass prominences have longer periods than low-mass prominences. They proposed that the cause of the increase in periodicity is the decrement of the sound speed with mass. In contrast, in the bottom panel of Figure 2.15 the dispersion in the scatter plot is small, and this means that there is no dependence of the period on the magnetic field. In a low-beta regime, longitudinal oscillations are associated with the slow oscillatory modes whose characteristic speed is essentially $c_{\rm s0}$. The period therefore does not change significantly with B_0. In the top and bottom panels of Figure 2.15 we also show that the differences obtained with respect to the reference simulation and therefore with the pendulum model are greater for larger radii. These results indicate that in addition to the curvature radius, the prominence width and the density contrast also modify the period of the longitudinal oscillations. This means that the pendulum model is only a first approximation of longitudinal oscillations. This result agrees with Luna et al. (2012a). They determined that for larger radii the pressure force contributes to the restoring force so that the pressure-driven term introduces a correction into the pendulum model. In addition, the discrepancies regarding the pendulum model could be caused by the calculation of the radii of the magnetic field line curvature. R is not uniform along the streamline. The distance along the field lines we used to calculate the averaged radii can modify the results considerably. Furthermore, in this research, the variations in time that R suffers due to the residual oscillations of the relaxation process were ignored.

To estimate the damping time per period, we computed these two parameters from the evolution of the x-component of the centroid. We obtained that $t_{\rm d}/P$ decreases slightly with $\rho_{\rm p0}$ and B_0, from 1.7 to 1.2 and from 1.8 to 1.1, respectively. $t_{\rm d}/P$ does not vary significantly with w_x, whose values range between 1.2 and 1.5 (these results do not change if we calculate the damping from the v_x series). The values of $t_{\rm d}/P$ are much lower for longitudinal oscillations than for the relaxation process. This significant damping in contrast to the transverse motion was also observed in the simulations of Luna et al. (2016b), who associated the damping mechanism for longitudinal motions with a numerical viscosity that cancels the motion by stress. The variations of $t_{\rm d}/P$ along with $\rho_{\rm p0}$ and B_0 could be understood by the correlation between the attenuation and the oscillation amplitude. For the same speed disturbance, the higher the density, the greater the inserted kinetic energy, and therefore the greater the oscillation amplitude. From the simulations we also obtained a slight increase in amplitude with magnetic force strength and so the variation of the attenuation, but the amplitude does not change with respect to w_x. Another mechanism that can explain the attenuation of longitudinal oscillations is wave leakage. Zhang et al. (2019) found in a 2D non-adiabatic filament simulation that when the ratio of gravity to Lorentz force is close to unity, longitudinal oscillations deform the magnetic field, generating the subsequent transverse waves which propagate away from the filament body. In our model we did not find significant deformation of the field lines and the system does not develop waves perpendicular to the magnetic lines (not shown here). This means that no wave leakage is observed in

the simulations. This is probably the case due to the low β regime considered in this work.

2.4.3 Horizontal transverse oscillation

To trigger horizontal transverse oscillations, we induced a velocity disturbance pointing in the y-direction. The spatial distribution of the velocity perturbation is the same as the one introduced in Section 2.4.2 for longitudinal oscillations, expressed by Equation (2.4). In this case, the maximum speed located at the centre of the prominence at a height of $z = 1.3\,H$ is $v_{y0} = 0.2\,c_{s0}$. In the top panel of Figure 2.16 we show an yz-slice of the y-component of the velocity (v_y) passing through the central plane at $t = 0$ together with some contours of the density profile. The plasma motion is somewhat complex. Initially, the inserted disturbance pushes the curtain, which is anchored at the base, tilting it towards the imposed direction. The displacement amplitude is greater in the internal parts of the filament where the velocity disturbance is stronger. Immediately, the plasma of the corona reacts to the movement in the opposite direction and tends to fill the displaced plasma. In addition, it is observed that the recovery movement starts at distinct times for different parts of the curtain. Regarding v_y, it is observed that during the first steps of the simulation the movement spreads as much throughout the prominence body as throughout the corona.

As time progresses, the oscillations are more localised at the prominence and its PCTR but attenuate at the corona. In the middle and the bottom panel of Figure 2.16 we show that v_y develops different stripes of opposite speed. These bands are localised in the prominence body but also in the background. The distribution of the velocity traces horizontal bands at the corona, but these stripes bend when they approach the prominence and take the shape of the density contour. These clear shear motions indicate differences in periodicity with height. The numerical results show that from the evolution of the y-component of the centre of mass, the oscillation period is $P = 9.41\,\mathrm{min}$, the damping time is $t_d = 11.9\,\mathrm{min}$, and the displacement amplitude is $f_0 = 0.14\,H$. As we expected, P is shorter than the one of longitudinal oscillations because in a low-β regime slow modes have longer periods. We obtained that for transverse oscillations P is longer than the one of the relaxation process. As has already been mentioned, P varies with height, therefore we plot in Figure 2.17 the oscillation period as a function of z. We computed P by fitting the temporary evolution of v_y for different heights with Equation (2.3) in which the sine was exchanged by a cosine. We obtained that the periodicity decreases with height. This result was also found by Zhou et al. (2018).

We again analysed the behaviour of horizontal transverse oscillations from the different events studied in Section 2.4.1. In Figure 2.18 the scatter plots of P are represented as a function of w_x, ρ_{p0} and B_0. The top and middle panels show that the periodicity increases with the prominence width and the initial density contrast. However, the bottom panel indicates that P decreases with the magnetic field strength. This behaviour coincides with the results observed in Figure 2.10 for the relaxation process. In both cases, the decrease with the strength of the magnetic field is strong and the increase with density and prominence width is weaker. The fast mode of transverse oscillations is essentially a magnetic wave that is driven by magnetic forces; for this reason, we expected to find a stronger dependence of the period on the magnetic field strength.

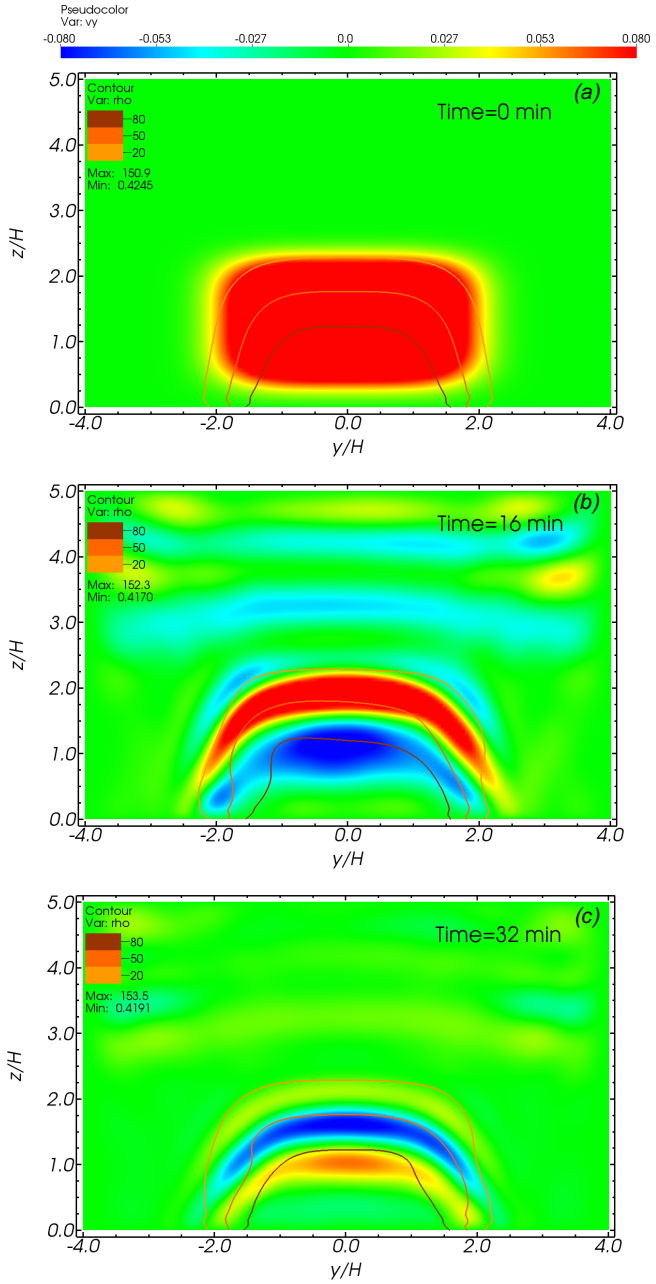

Figure 2.16: Evolution of v_y at the yz-plane passing through $x = 0$ in the case of horizontal transverse oscillations together with the prominence density (orange-coloured isocontours). The initial parameters are the same as those in Figure 2.1. v_y is normalised to c_{s0} and density to ρ_0.

The restoring force for the horizontal transverse oscillations is the magnetic tension force but not the gravity or the pressure gradient. The different driving mechanisms for longitudinal and transverse oscillations reveal the different periodicity of the two oscillation modes.

While for vertical oscillations we obtained that t_d/P varies with ρ_{p0} and B_0, the damping in horizontal transverse oscillations does not change considerably with the considered parame-

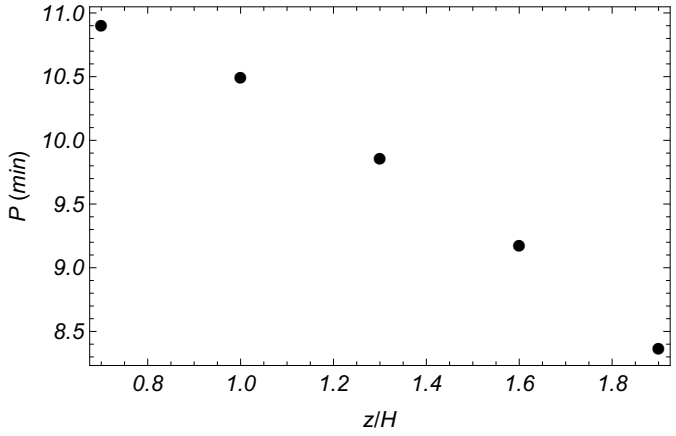

Figure 2.17: Scatter plot of the period as a function of height in the case of horizontal transverse oscillations. The initial parameters are the same as those in Figure 2.1.

ters. When we compute $t_{\rm d}/P$ from series of the y-component of the centroid, all events show values that range from 1.25 to 1.34. These values are higher (from 2.79 to 2.92) when the calculation is made from the series of v_y at the point $x = 0$, $y = 0$, $z = 1.3\,H$. This means that we have different damping at different parts of the prominence. As was explained in Section 2.4.1, the attenuation mechanism of the transverse modes is resonant absorption. For horizontal oscillations the absorption would occur in the upper part of the curtain, in its PCTR. However, as we showed in Figure 2.16, the shear motions are displaced towards the inside of the prominence. This behaviour is studied in more detail in Section 2.4.4. The attenuation of transverse oscillations also depends on the PCTR. As we saw for the vertical oscillations, we obtained that the smoother the PCTR, the stronger the attenuation. We obtained that for $n = 2$, $t_{\rm d}/P = 0.7$, $n = 4$ $t_{\rm d}/P = 1.27$ and $n = 6$ $t_{\rm d}/P = 1.87$, respectively.

A combination of the longitudinal and the transverse disturbance simultaneously triggered, shows that the two modes oscillate independently from each other. We have obtained that the periodicity of the y-component of the centroid is 9.41 min, the same result as in the single case. The period of the x-component is now 35.1 min instead of 37 min which was the case for longitudinal oscillations. The difference could be explained by the fact that the transversal movement, when pushing the magnetic field lines, modifies its radius.

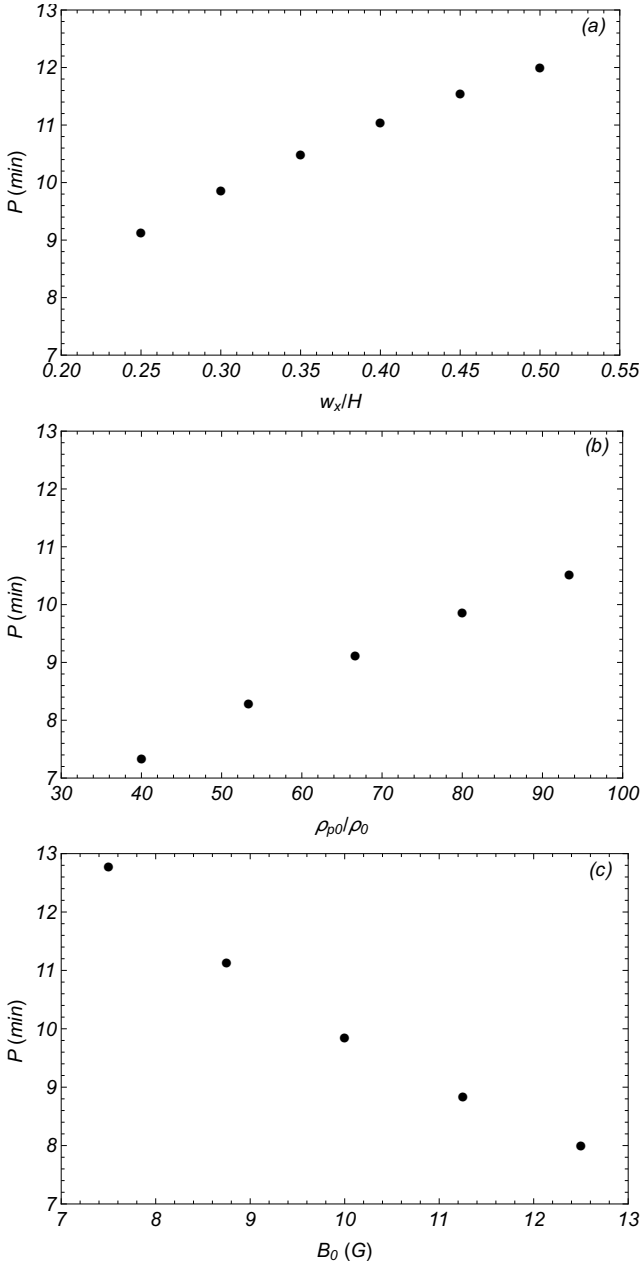

Figure 2.18: Same as Figure 2.7 but for horizontal transverse oscillations.

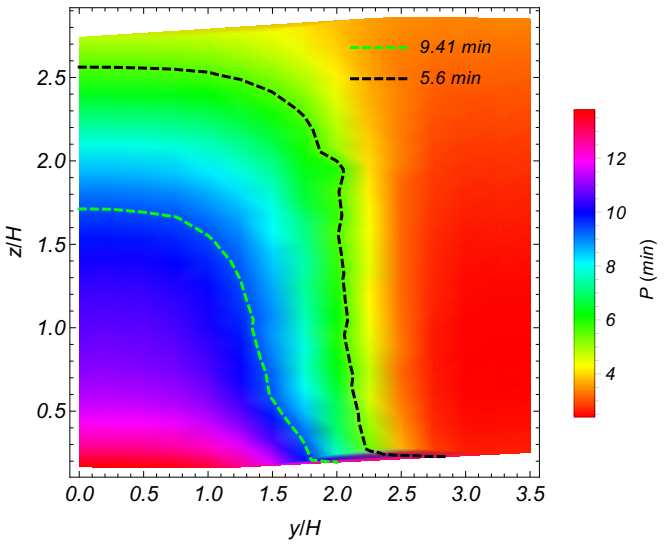

Figure 2.19: Alfvén continuum spectrum in terms of the periodicity as a function of the position of each field lines at $x = 0$. Dashed black and green curves are the isocontours corresponding to the periods of the vertical and transverse oscillations respectively inferred from the time-dependent simulations.

2.4.4 Continuum modes

We have computed the Alfvén continuum modes of the MHD equations based on the expressions of Goossens et al. (1985). They derived the continuous spectrum of a 2D magnetostatic equilibrium. Their study is invariant with respect to y, therefore we considered our structure as $2D$ slices in the xz-plane. This is the main approximation because our prominence model is in 3D. The expression for the modes of the Alfvén continuum is written in Terradas et al. (2013) (see their Equation (15)) in terms of the distance along the magnetic field lines. According to this equation, we can numerically compute the Alfvén frequency for different field lines by solving the eigenfrequency problem. To solve the equation, we need to extract the coordinates of each line and the variations of the magnetic field strength along the field line for the equilibrium state. We selected diverse magnetic field lines whose footpoints range from $-4.315\,H$ to $-3.65\,H$ in the x-direction and from 0 to $3.5\,H$ in the y-direction. The Alfvén spectrum is represented in Figure 2.19 in terms of the oscillatory period as a function of the position of each line at the central plane. The computation of the local Alfvén frequency is useful for understanding the resonant absorption process (see Section 1.3.4) because, essentially, the resonant surface is the one where this frequency coincides with the frequency of the global mode inferred from the time-dependent simulations. In Figure 2.19 we show the contour of the global mode for the relaxation process (dashed black line) and for the horizontal transverse oscillation (dashed green line). For vertical oscillations, the resonant surface is more external than in the horizontal case. Terradas et al. (2008a) found that the resonant surface can be located inside the structure, as we have obtained for the horizontal case. In Section 2.4.1 and Section 2.4.3, according to the velocity distribution of Figure 2.8 and Figure 2.16, we have estimated where the energy conversion takes place: at the y-edges of the prominence body for the relaxation case and at the sheared bands inside the prominence for the horizontal transverse oscillations. However, the location of the reso-

nant absorption process is clearer when we study the kinetic energy of the system. The top panel of Figure 2.20 shows that the resonance surface of the vertical motion (dashed black curve) matches in space the location where the kinetic energy associated with the vertical velocity component, i.e. $E_{\mathrm{kin},z} = \frac{1}{2}\rho\, v_z^2$, increases due to the energy conversion. Only one snapshot of $E_{\mathrm{kin},z}$ at $t = 8.4\,\mathrm{min}$ is represented, but the maximum of $E_{\mathrm{kin},z}$ is always localised around this point until the oscillations attenuate. In the bottom panel of Figure 2.20 we show a snapshot at $t = 32\,\mathrm{min}$ of the kinetic energy associated with the horizontal transverse oscillations, that is $E_{\mathrm{kin},y} = \frac{1}{2}\rho\, v_y^2$. Again, the resonance layer almost coincides with the maximum energy of the system. The exact behaviour of 3D Alfvén resonances has been studied in Wright & Elsden (2016) and Elsden & Wright (2017). They found that in 3D an infinite number of possible resonant solutions exists within a resonant zone, where the energy is accumulated, on which a dominant contour stands out from different ridges. It is beyond the scope of the present work to calculate the 3D Alfvén resonances, and it is sufficient to mention that the 2D approach provides reasonable results.

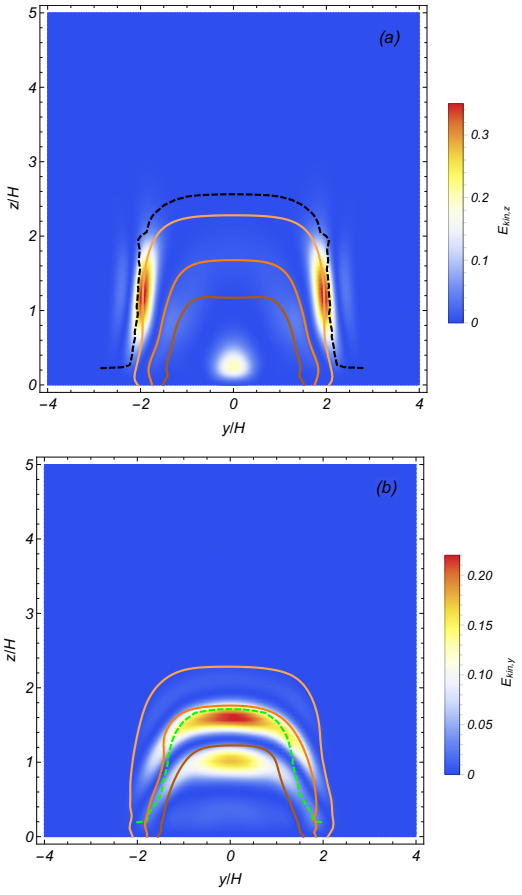

Figure 2.20: Top panel: Snapshot of the vertical kinetic energy and the density profile at $t = 8.4\,\mathrm{min}$ together with the vertical resonant surface (dashed black curve) obtained in Figure 2.19. The orange-coloured density contours are the same as bottom panel of Figure 2.8. Bottom panel: Snapshot of the y-component of kinetic energy and the density profile at $t = 32\,\mathrm{min}$ together with the horizontal resonant surface (dashed green curve) obtained in Figure 2.19. The orange-coloured density contours are the same as bottom panel of Figure 2.16. Kinetic energy is normalised to $\rho_0\, c_{\mathrm{s}0}^2$.

2.4.5 Effect of numerical resolution

Based on Terradas et al. (2016) and in order to study the numerical dissipation of the system, we have performed a detailed analysis of the evolution of the total energy ($E_{\rm tot}$) of the system; the sum of magnetic ($E_{\rm B}$), internal ($E_{\rm p}$), gravitational ($E_{\rm g}$), and kinetic energy ($E_{\rm k}$); integrated over the whole 3D domain. The expression $E_{\rm B} = \frac{1}{2\mu}\left(B_x^2 + B_y^2 + B_z^2\right)$, $E_{\rm p} = \frac{p}{(\gamma-1)}$, $E_{\rm g} = \rho\, z\, g$, and $E_{\rm k} = \frac{1}{2}\rho\, v^2$. In Figure 2.21 we have represented the total energy difference with respect to the initial state ($\Delta E_{\rm tot} = E_{\rm tot}\,(t) - E_{\rm tot}\,(t=0)$), normalised to the total energy at $t = 0$ ($E_{\rm tot,0}$) in the case of the reference relaxation process (solid line). The curve decreases until reaching a quasi stationary state as a consequence of numerical diffusion produced at scales below the spatial grid resolution. As we can see in the dashed curve of Figure 2.21, increasing the resolution of the system reduces the energy dissipation. It is important to mention that this reduction in energy loss does not significantly change the evolution of the system and we obtain essentially the same damping time and the same period in both simulations. Actually, the energy losses are very small (of the order of 10^{-2} %) and therefore do not affect the estimation of periods and damping times. In the cases of horizontal transverse and longitudinal oscillations the simulations also show similar attenuation. For this reason it seems that the attenuation of our system in the case of horizontal/vertical oscillations is not connected with numerical diffusion.

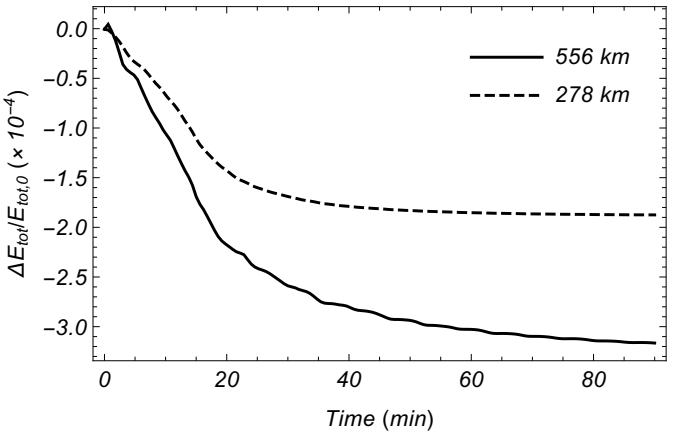

Figure 2.21: Change in total energy for two different grid resolutions in the case of the relaxation process of the reference simulation.

2.5 Conclusions and discussion

A 3D numerical study of transverse and longitudinal oscillations in filaments has been presented. A curtain-shaped prominence is anchored to the base of the corona so that the system does not develop downwards flows due to Rayleigh-Taylor instabilities, which complicate the analysis of the results of the oscillatory motions. In addition to the fixed foot of the structure, the behaviour of the system is subject to closed boundary conditions, meaning that we have imposed line-tying conditions at all sides of the computational box. This perfectly reflecting condition applied in the bottom plane is essential to support the structure. Line-tying conditions applied at the lateral and the upper boundaries ideally imply the conservation of the total energy. However, as was already mentioned in Section 2.4.5, the system shows a little loss of energy due to numerical dissipation. A better grid resolution reduces the energy dissipation, however, the evolution of the system does not depend on it and we obtained the same damping time and period for different resolutions. This means that the attenuation of our system in the case of horizontal and vertical oscillations is not connected with numerical diffusion. To study the attenuation mechanism for transverse oscillations, we analysed the velocity distribution of the motions, the dependency of the attenuation on the PCTR, and the continuum Alfvén modes. In agreement with our simulations, we proposed that the main damping mechanism is resonant absorption. As the theoretical models predict, we obtained that the attenuation is stronger for a wider PCTR. From the analysis of the Alfvén continuum modes, we obtained that the location of the resonant surface coincides with the concentration of the kinetic energy as expected from the resonant absorption process. However, we obtained that $t_{\rm d}/P$ ranges from 2.2 to 7.9 for the relaxation process of different scenarios, values which in principle are higher than expected from the observations. This means that in addition to the resonant absorption, another type of damping mechanism must be considered in our model. On the other hand, for transverse and longitudinal horizontal oscillations we obtained a stronger attenuation. One reason that can explain this significant damping for longitudinal oscillations could be changes in periodicity with height. The plasma of two adjacent magnetic field lines with different curvature radius oscillates at a different frequency, so that some shear develops in the system. This type of sheared viscosity mechanism can also contribute to the attenuation of horizontal transverse oscillations. The shear motions inside the prominence due to the resonant absorption can brake the oscillation and increase the attenuation. Our model is relatively simple to understand the observed damping, and other mechanisms such as non-adiabatic processes, mass flows, or partial ionisation effects must be considered.

Regarding the periodicity, we reproduced oscillations with periods that range approximately from 4.2 min to 7.3 min for vertical oscillations, from 28.2 min to 42.3 min for longitudinal oscillations, and from 7.4 min to 12.0 min for horizontal transverse oscillations. These results give periods that are somewhat shorter than those reported in the observations. In Tripathi et al. (2009) the periods associated with vertical motions range from 15 min to 29 min and in Shen et al. (2014a) from 11 min to 22 min. In Luna et al. (2018) the periods for horizontal transverse oscillations range from 30 min to 80 min and for longitudinal events from 30 min to 110 min. We recall that in the field of observations, in contrast to this work, longitudinal oscillations are motions along the filament axis. Mackay et al. (2010) reported that the magnetic field rotates with respect to the filament axis by an angle in the range from 15 to

30 degrees. Then, Luna et al. (2018) in their catalogue considered as longitudinal oscillations those whose velocity vector forms an angle with the filament axis smaller than 40^{o}. This suggests that a certain error is made in classifying the oscillation polarisation. Despite the short results obtained in P, for longitudinal oscillations we performed a reference simulation that agrees with the pendulum model. However, for values of w_x and ρ_{p0} different from those of the reference simulation, the results move away from the theoretical expression. This means that another mechanism may drive the longitudinal motions, such as pressure force. For example, we obtained that the periodicity of the oscillations increases with the prominence width independently of the polarisation direction. This is an interesting result because it can be compared with diverse observed events. Luna et al. (2018) collected a valuable catalogue that can be used to extract useful information, especially from the statistics section. In agreement with our results, in Figure 21 (panel *d*) of Luna et al. (2018) they show that P tends to increase with width for quiescent prominences. In addition, the catalogue shows that high values of t_{d}/P are reported, which means that our results are not as different as the observed results. Moreover, strong damping of about $t_{\mathrm{d}}/P \sim 1.25$ is the mean value obtained for longitudinal oscillations. As we found for horizontal transverse and longitudinal oscillations, Luna et al. (2018) did not find a correlation between t_{d}/P and the filament dimensions.

Another interesting result that we can compare with observations is the variation of P with height. Hershaw et al. (2011) studied the dependence of the periodicity and the attenuation on height of two successive trains of transverse oscillations observed on July 30th 2005. They found that the periods range between 90 and 110 min and increase slightly with height. Conversely, Shen et al. (2014b) did not find differences of the period with the altitude in a transverse oscillation observed on August 9th 2012, so that they suggested that the prominence oscillated as a rigid body. These behaviours differ from our results and from those of Zhou et al. (2018). We obtained that the period increases with height for longitudinal oscillations and decreases for transverse ones. These discrepancies suggest that a deeper analysis of the variations of P with height is necessary. For example, Hershaw et al. (2011) reported long periods, and if we take into account our simulations we can interpret that the reported oscillations are longitudinal instead of transversal. In any case, knowing the oscillation polarisation with respect to the magnetic field is essential for understanding the nature of the wave motions.

We have exhaustively analysed vertical oscillations for different scenarios. The origin of these oscillations is the relaxation process of our prominence model. For the stationary state, we induced a v_z perturbation in the reference simulation to trigger vertical motions. The results (not shown in this work) reveal basically the same behaviour as the relaxation process. According to this, we could consider the vertical oscillations of the relaxation process as a winking filament if the velocity amplitude of the movement is sufficiently large. We did not take the nature of the disturbance into account here. For this reason, in a future work we will study the dependence of the oscillations varying the characteristics of the perturbation. This is partially addressed in Chapter 3.

Chapter 3

Extension of the prominence model: incorporating shear and external perturbations

3.1 Introduction

In Chapter 2 we have studied the dynamics of a curtain-shaped prominence embedded in an unsheared magnetic field. However, the observed magnetic arcades that extend upwards into the corona from the filament channel and support the prominence plasma show a strong shear. The angle between the field lines of the arcade and the prominence spine is about 25° on average (Leroy et al. 1983). Moreover, the trigger mechanisms of large amplitude oscillations are usually external waves, such as Moreton or EIT waves, that impact the prominence and activate the oscillations. On the contrary, in the simulations analysed in the previous chapter, we have utilised an internal velocity disturbance instead of an external perturbation.

Luna & Karpen (2012) studied longitudinal oscillations triggered by flows of hot evaporated plasma that push the thread. These flows are produced during the process of prominence formation by thermal evaporation-condensation. Zhang et al. (2013) compared the nature of two types of perturbations. In the first case, a velocity perturbation over the whole prominence body was performed and for the second case they utilised impulsive heating deposited near one of the legs of a magnetic loop to mimic a microflare near the prominence. They found that the oscillation period does not strongly depend on the type of perturbation. In order to trigger oscillations, internal velocity perturbations have been proposed by Luna et al. (2016b), Zhou et al. (2018), or Zhang et al. (2019), and Kraśkiewicz et al. (2016) perturbed their model of prominence by adding a gas pressure pulse. An alternative method was suggested by Liakh et al. (2020) in which the authors incorporated a source term in the momentum equation. In this way, all the magnitudes adjust to the source term following the MHD equations. In spite of the difference between the trigger mechanisms proposed in numerical studies, all of them are internal disturbances and only Liakh et al. (2020) modelled external perturbations. For the external disturbance they used a source term in the equation

of energy which induces a strong pressure perturbation that rapidly propagates towards the cool prominence. The passing wave deforms the magnetic field lines of the flux rope but it does not hit directly the dense prominence. However, the changes in the magnetic field lines propagate producing significant perturbations of the magnetic field that end up being responsible for the prominence oscillations.

One of the difficulties of using an external velocity pulse located at the tenuous corona is that, due to the low density there, a very large velocity amplitude is necessary to reach the required energy to push the heavy plasma. This large amplitude in the initial perturbation can be challenging from the numerical point of view because it can generate strong shocks. How we apply the disturbance in the system is a key aspect of the present chapter. This perturbation is analysed in two different prominence models: the sheared magnetic arcade and the H&A model, partially described in Chapter 1.

3.2 Sheared magnetic arcades

Since observations show that the filament axis is approximately aligned with sheared magnetic field lines, we extend the prominence model of Chapter 2 to have the appropriate angle between the prominence spine and the field lines. In our arcade model, Equation (1.38), the magnetic shear is set by the parameter l/k. Figure 3.1 shows the magnetic filled lines for three different values of l/k. In this case, we set $B_{01} = B_{02}$, $z_0 = 0$, and $k_2 = 3k_1$. When $l/k = 1$, we are in the unsheared configuration (left panel of Figure 3.1). From Figure 3.1 we can discern different features. First, we see that the shear of the magnetic structure increases when reducing the parameter l/k. When the shear increases longer field lines are obtained, so that the width of the numerical simulation domain in the y-direction must be larger than the one in the unsheared case. Another important aspect of the quadrupolar sheared magnetic arcades is that at the centre of the configuration ($x = 0$) there is a null point where the magnetic components B_x and B_z are equal to zero (although for sheared fields B_y is different from zero and the term null point is no longer applicable). The height of this point is

$$z_X = \frac{1}{l_1 - l_2} \ln\left(\frac{B_{01}}{B_{02}} \frac{l_1 k_2}{l_2 k_1}\right). \tag{3.1}$$

For unsheared magnetic arcades we have that $z_X = 0$. When we have shear, the magnetic field lines that cross the point $x = 0$ and $z = z_X$ is totally horizontal along the y-axis. The middle and right panels of Figure 3.1 show that below z_X the spin of the shear points in the opposite direction. This is clearer in Figure 3.2 which displays the top view of the same configuration of the middle and the right panel of Figure 3.1. Figure 3.2 also shows that the shear of the magnetic lines varies with height. The shear angle with respect to the y-axis is defined as $\theta = \text{atan}(B_x/B_y)$. The shear angle as a function of z for $l/k = 0.75$ (dashed line) and $l/k = 0.55$ (solid line) is represented in Figure 3.3. At $z = z_X$, $\theta = 0$. As already mentioned, below the point z_X the direction of the spin reverses which turns into a change in the sign of θ. For $l/k = 0.55$ and $z = 2\,H$ the shear angle is about 25° which is the angle found in the observations.

In addition, Figure 3.1 also shows that the configuration of the magnetic dips of the structure varies with the magnetic shear. The location of the dips is invariant in the y-direction, for

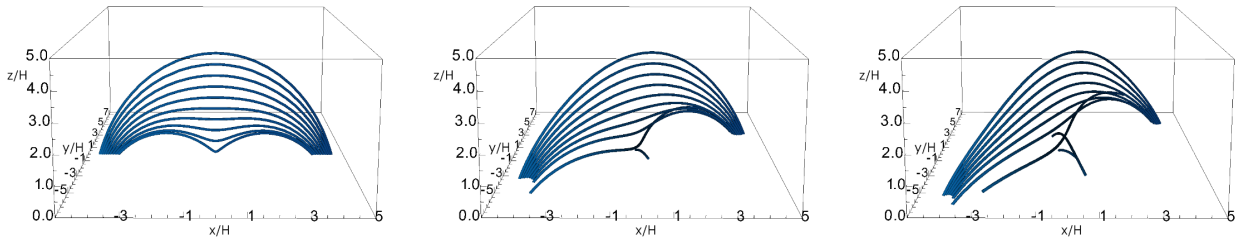

Figure 3.1: Magnetic field lines for three different values of the magnetic shear, $l/k = 1$ (left panel), $l/k = 0.75$ (middle panel), and $l/k = 0.55$ (right panel). In all cases $B_{01} = B_{02}$ and $z_0 = 0$. The selected field lines of each panel cross the structure through $x = 0$ and $y = 0$ at different heights.

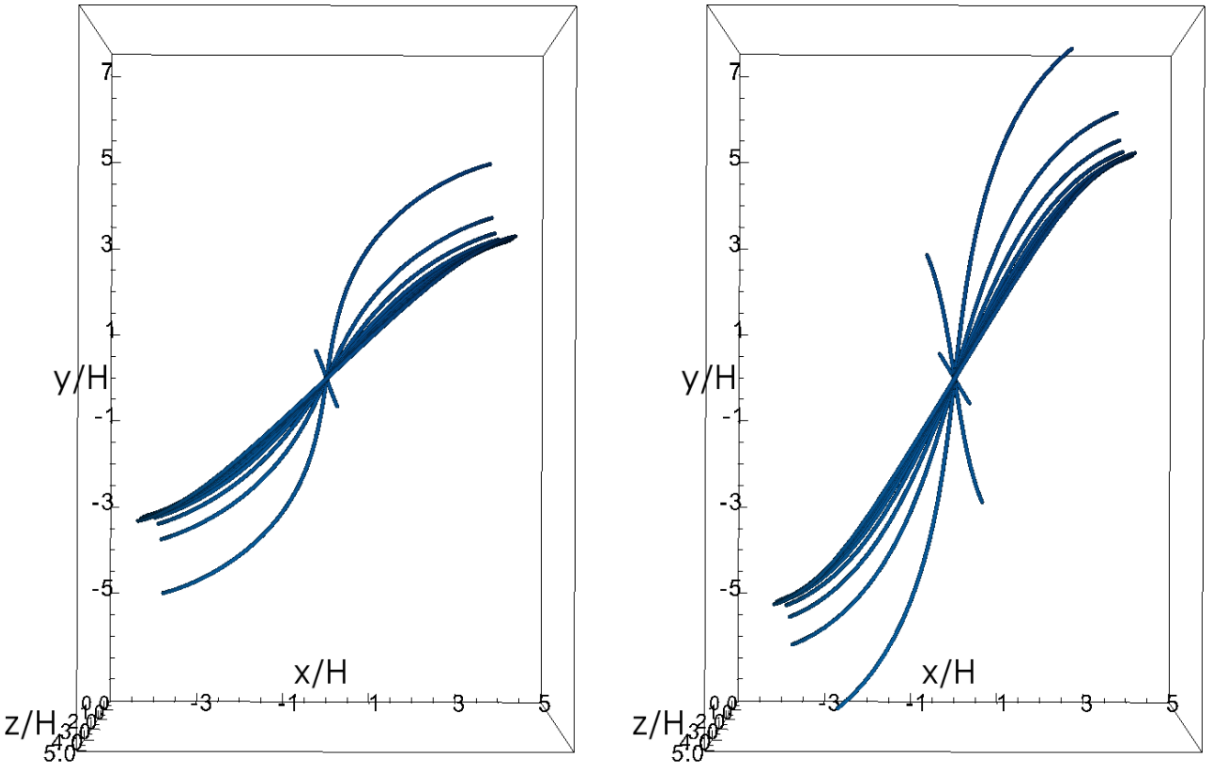

Figure 3.2: Top view of magnetic field lines for $l/k = 0.75$ and $l/k = 0.55$. In both cases, $B_1 = B_2$ and $z_0 = 0$.

this reason we present in Figure 3.4 some magnetic field lines projected in the xz-plane for different values of the shear. Firstly, what stands out in this figure is that the region with dips (from z_X to the first concave downwards line, i.e., where the curvature of the field lines changes) is wider for configurations with less shear. Moreover, a closer inspection of the figure shows that when the shear increases, the depth and the width of the dips change. To compare the field lines of the three configurations we plot in Figure 3.5 two lines of each structure crossing the centre of the structure at the same height. The apex of the top lines

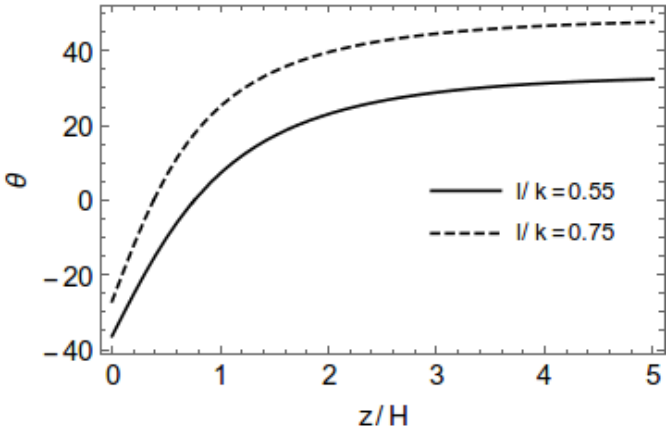

Figure 3.3: Shear angle as a function of height for $l/k = 0.75$ (dashed curve) and $l/k = 0.55$ (solid curve).

is almost flat for the three cases, but for the configuration with the strongest shear (green lines) the field line is more curved. The depth of the dips increases when we move towards the chromosphere. The bottom lines have a central height equal to z_X with $l/k = 0.55$. At this point, the depth of the dip is larger for $l/k = 0.55$ and it decreases with increasing l/k. On the contrary, the width of the dips increases with decreasing the shear. All these different features point out that the magnetic support can strongly depend on the magnetic shear. Another conclusion that can be drawn is that in the present model we do not obtain deep dips, even when we change the magnetic shear. As we will show in the following, this has important implications.

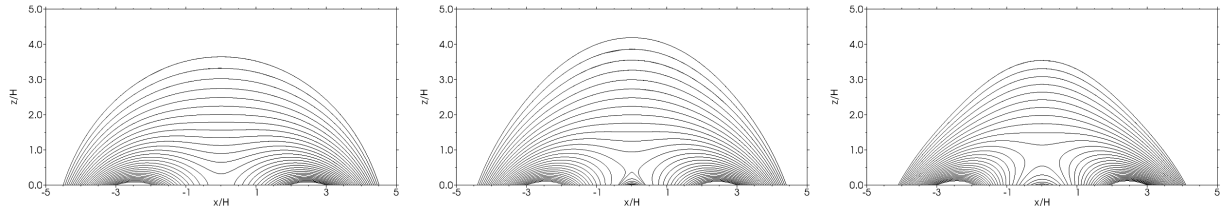

Figure 3.4: Projection at the xz-plane of selected magnetic field lines for $l/k = 1$, $l/k = 0.75$, and $l/k = 0.55$. The lines are set to cross the centre of the structure at the same height.

3.2.1 Initial set up and numerical aspects

To study the dynamics of solar prominences in sheared magnetic arcades we build an isothermal stratified background atmosphere as in Chapter 2 (Equation (1.24)), but now, with the aim of being more realistic, we introduce a thin chromosphere-corona transition region at the bottom of the domain. This transition consists of an isothermal region whose pressure scale height is twenty times larger than the one of the coronal part. We impose continuity in the density and pressure profiles at the chromosphere-corona interface. The transition region can be seen in Figure 3.6 as horizontal layers of density isocontours, and more clearly in Figure 3.9 where we display the density profile along a specific field line. The plasma

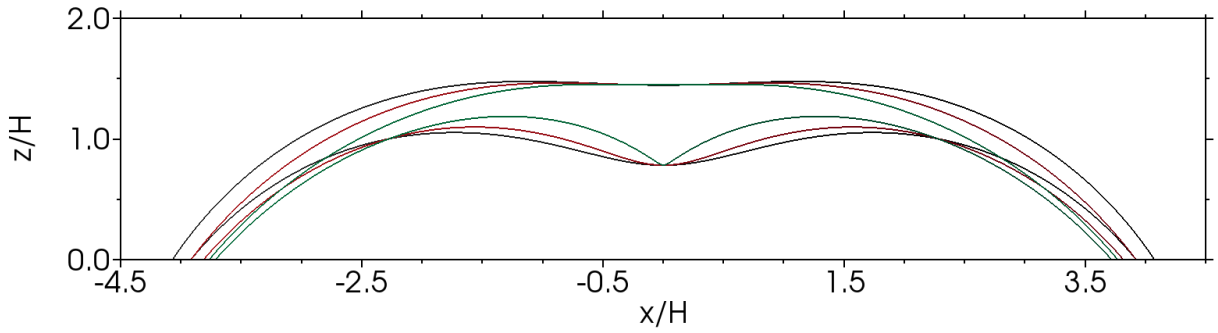

Figure 3.5: Selected magnetic field lines for the case $l/k = 1$ (black lines), $l/k = 0.75$ (red lines), and $l/k = 0.55$ (green lines).

is permeated by a sheared magnetic arcade, given by the magnetic components of Equation (1.38). We set $l_1/k_1 = 0.55$ (right panel of Figure 3.1) to have a shear angle of about 25°, as the observations suggest. To avoid the point in the domain that inverts the spin of the field lines we set $z_0 = z_X$. The rest of the magnitudes are the same as those of the reference simulation in Chapter 2, which also includes the parameters of the prominence mass deposition (Equation (2.2)).

The code we used to solve the MHD equations is the MoLMHD code (see Terradas et al. 2008b; Bona et al. 2009; Terradas et al. 2013, for details about the numerical method), where we have included the superbee limiter dissipation term (Roe 1985). As in Chapter 2, we applied line-tying boundary conditions at all planes of the computational domain. The numerical domain is a box of $180 \times 270 \times 90$ mesh points. The dimensions of the box are 100 Mm in the x-direction, 150 Mm in the y-direction, and 50 Mm in the vertical component. In this way, we imposed an equidistant grid of 0.556 Mm.

3.2.2 External perturbation

For many oscillatory events reported in the observations we do not identify the trigger mechanism of prominence oscillations (Luna et al. 2018). However, it is known that wave disturbances initiated by flares are responsible for triggering the oscillations both, near to and far from the flare. They are large-scale propagating disturbances in the solar atmosphere and are considered to be fast mode MHD waves. In addition, there is evidence that these waves are of non-linear nature. The aim of this chapter is to study the dynamics of solar prominences triggered by distant disturbances. However, if we simply impose an external velocity pulse, keeping the rest of variables unchanged, we will need a very large initial velocity amplitude to push the prominence with the required energy. As we have explained before, there are numerical issues and simulations might not work. To have an initial consistent perturbation it is necessary for the rest of variables to be modified in order to fulfill the governing equations, at least in an approximate way. This problem was addressed in Liakh et al. (2020) who incorporated a source term for each of the MHD equations. In this way, they produced self-consistent solutions where all the variables of the perturbation adjust to the source term following the MHD equations. However, we implement an alternative

method that was partially discussed in Piantschitsch et al. (2020).

We consider the simple situation of a vertical magnetic field as well as a constant density and a constant pressure. For the perturbations we can assume that the variables depend on the velocity v, which is transverse to the equilibirum magnetic field. It is not difficult to see (e.g., Piantschitsch et al. 2020) that for a purely magnetic fast wave, density variations in the wave are related to the velocity through the following equation

$$\rho_{\rm pert} = \rho \left(1 \pm \frac{v}{2v_{\rm A0}}\right)^2, \tag{3.2}$$

for right (+) and left (−) propagating waves. $v_{\rm A0}$ is the unperturbed Alfvén speed and v is the velocity amplitude of the wave. From the adiabatic condition $p\rho^\gamma = \text{constant}$ we obtain (for the right propagation) that

$$p_{\rm pert} = p \left(1 + \frac{v}{2v_{\rm A0}}\right)^{2\gamma}. \tag{3.3}$$

Finally, the magnetic variations are

$$\mathbf{B}_{\rm pert} = \mathbf{B}\frac{\rho_{\rm pert}}{\rho}. \tag{3.4}$$

The previous equations provide the recipe to produce an initial non-linear perturbation with consistent fluctuations in velocity, density, gas, and magnetic pressure.

Obviously, in an arcade configuration the previous equations are no longer valid since they were derived for a very simple equilibrium configuration. However, they can be used as a guide to calculate an approximate form of the perturbation in the inhomogeneous equilibrium. In this case the velocity disturbance is imposed to be aligned along the sheared field lines and external to the dense prominence. It is expressed as

$$v_{\rm pert} = v_0 \exp\left[-\left(((x - x_0^*)/w_x)^2 + ((y - y_0)/w_y)^2 + ((z - z_0)/w_z)^2\right)\right], \tag{3.5}$$

being $x_0^* = y/\tan\phi - x_0$ and $\phi = \text{atan}(B_y/B_x)$. To excite a fast MHD wave, the velocity components are expressed as

$$\begin{cases} v_x = v_{\rm pert}\sin\phi, \\ v_y = -v_{\rm pert}\cos\phi. \end{cases} \tag{3.6}$$

Using this expression for the velocity we apply the previous equations to the rest of the variables, taking into account that the magnetic perturbation must be perpendicular to the local magnetic field.

The perturbation pulse should be placed at a certain distance from the prominence body since we are interested in external perturbations. It turns out that the magnetic arcade configuration is a periodic system in the x-coordinate. The consecutive arcades are separated by an interface of a purely vertical field at $x = \pm L/2$. In our numerical domain, we have only one arcade. If the perturbation was located in the adjacent arcade, the wavefront would remain trapped in the neighbouring arcade. To avoid this situation, the initial position of

the perturbation must be located inside the main arcade, so that we are not able to initially place the pulse too far from the prominence body with the present magnetic configuration. The initial velocity amplitude of the pulse is $v_0 = 5\,c_{s0}$, where $c_{s0} = 166\,\mathrm{km\,s^{-1}}$ is the sound speed. We set $w_x = 0.8\,H$, $w_y = 1.8\,H$, $w_z = 1.5\,H$, $x_0 = 4.5\,H$, $y_0 = 3\,H$, and $z_0 = 2.5\,H$. The module of the velocity pulse is plotted in the top left panel of Figures 3.6 and 3.7.

3.2.3 Results

As in Chapter 2, the prominence mass deposition is instantaneous and so the initial configuration is not in static equilibrium. Unlike in Chapter 2, now the relaxation phase is not relevant here. During the relaxation we have introduced a simple dissipation term in the equation of motion to force the system to quickly achieve an equilibrium. This method is efficient to save computational time in the relaxation process.

At this stage it is important to mention that the density profile tends to softly rotate with the magnetic lines. When the point given by z_X is inside of the numerical domain as in Figures 3.1 and 3.2, the spin of the shear points in the opposite direction and so the rotation of the prominence during the relaxation appears at different heights. The inverse turn strangles the plasma and abruptly increases the pressure which causes the simulation to stop. For this reason we imposed $z_X = 0$. The final state after the relaxation is plotted in the first panels ($t = 0$) of Figures 3.6 and 3.7.

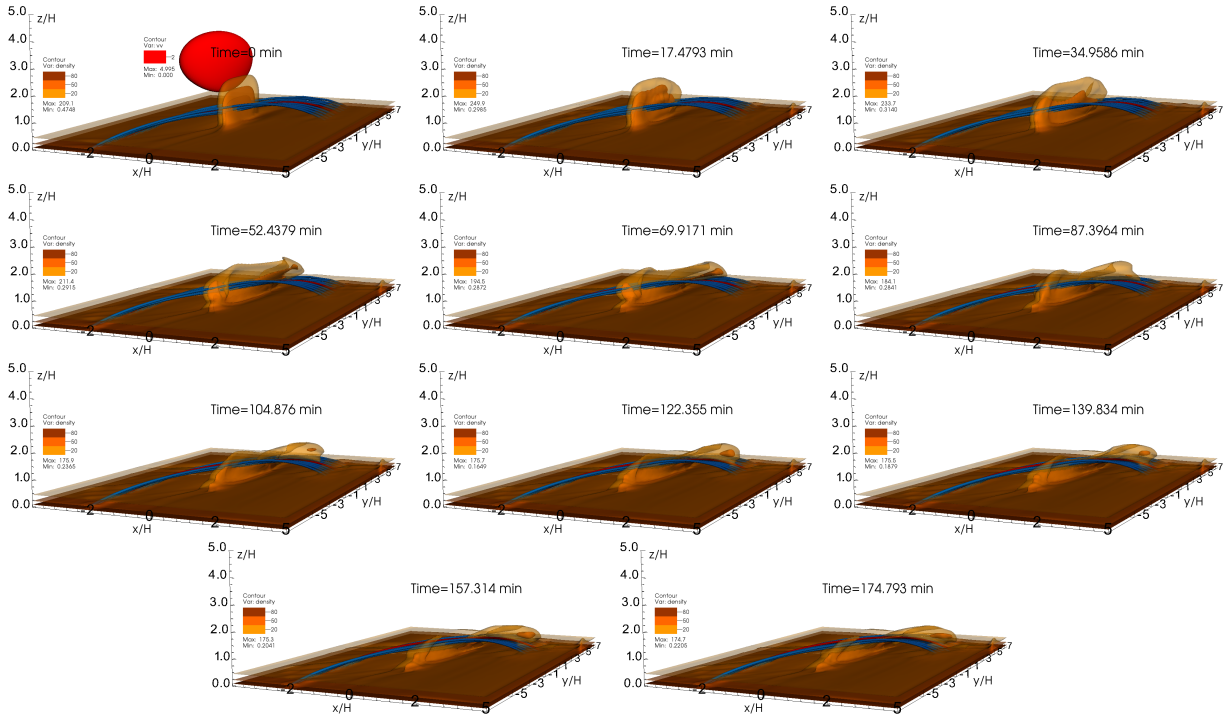

Figure 3.6: Time evolution of density and magnetic field lines. The module of the velocity perturbation (normalised to $c_{s0} = 166\,\mathrm{km\,s^{-1}}$) is plotted in the top left panel at $t = 0$. The red magnetic field line is used to find the density profile of Figure 3.9.

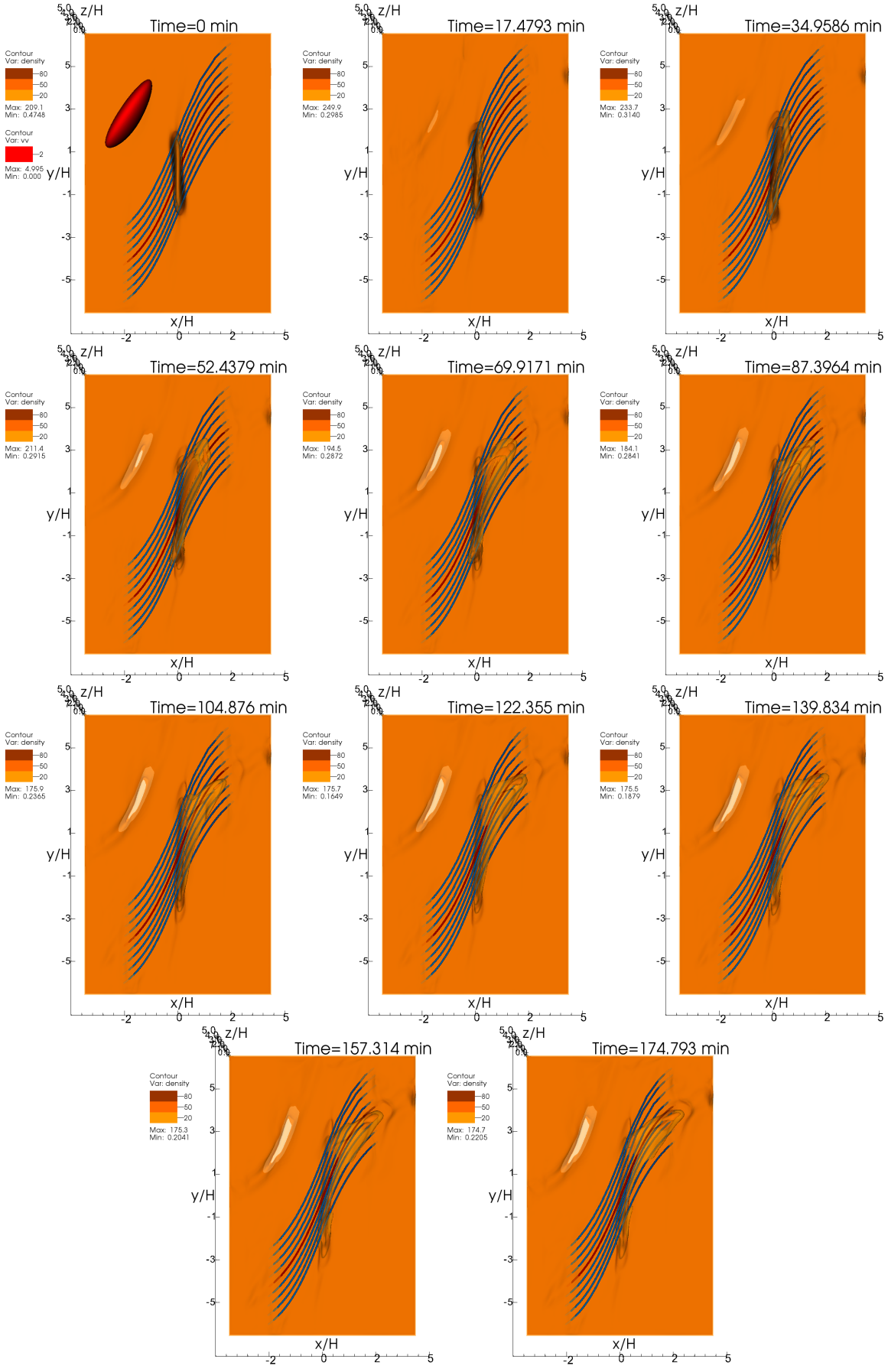

Figure 3.7: Top view of Figure 3.6.

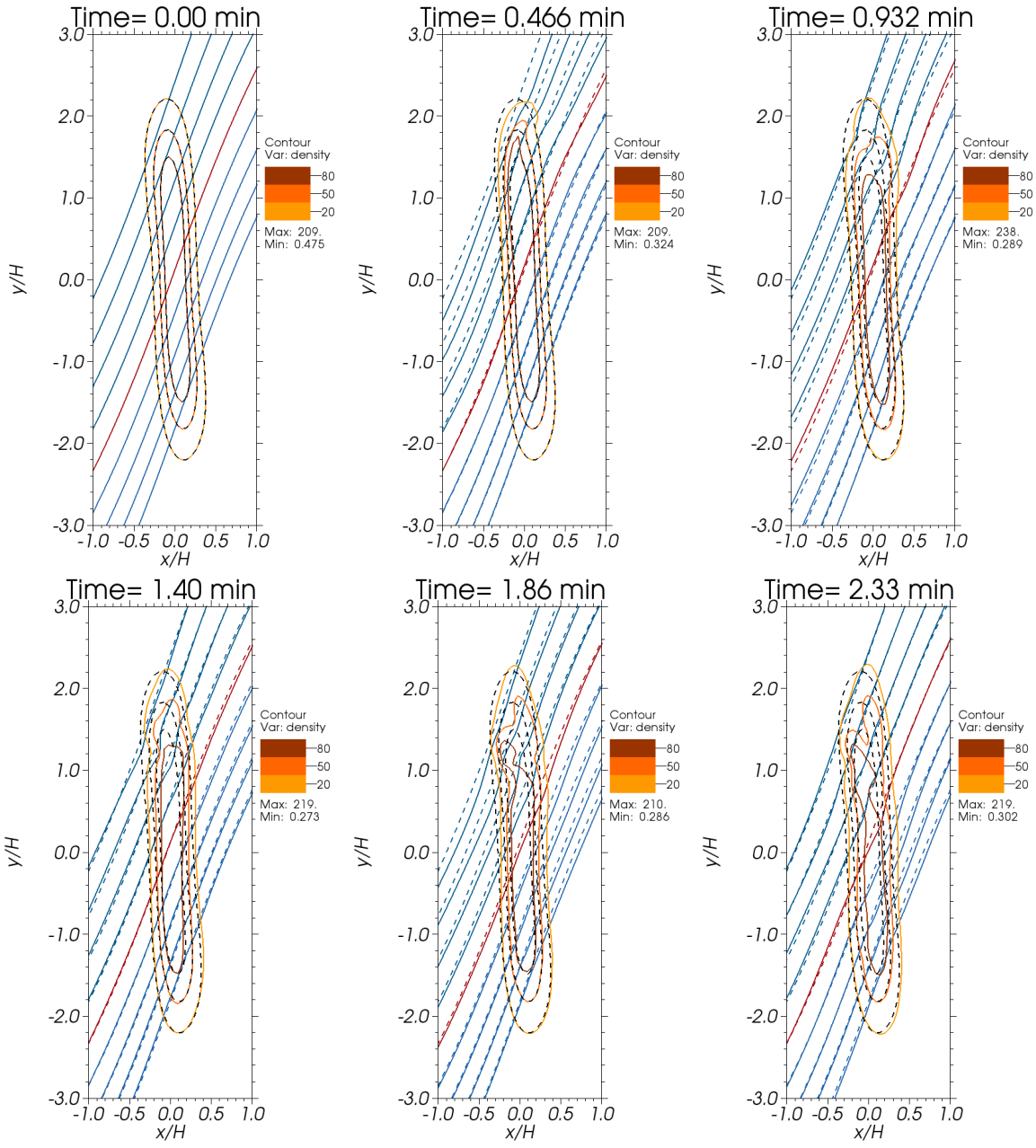

Figure 3.8: Time evolution of the density and magnetic field lines for the first time steps of the simulation. The density isocontours depict the prominence body at the xy-plane at $z = 0.79\,H$. This height corresponds approximately to the dip height of the red field line of Figures 3.6 and 3.7. The magnetic field lines are projections at the same xy-plane. The dashed curves correspond to the initial state.

Once the prominence is relaxed enough, we can remove the dissipation term in the equation of motion and perturb the prominence with the external disturbance described before. The module of the velocity perturbation is plotted in the top left panel of Figures 3.6 and 3.7 at $t = 0$. The perturbation moves towards the prominence and impacts transversely the dense body at the closest edge. Figures 3.6 and 3.7 show the time evolution of the 3D

structure for a long time period. Before analyzing the dynamics of the system for long time periods, it is important to observe how the prominence shakes during the first time steps. Figure 3.8 shows the time evolution of the prominence body at the beginning of the simulation. The top left panel shows the initial state and it is plotted as dashed lines in the other panels. We see that at the very beginning only a small portion of the prominence moves into the right direction. This displacement has a very small amplitude. In the top middle panel we clearly see that the plasma sweeps the magnetic field lines. The first displaced magnetic field lines are those placed at the left of the red field line, i.e., those that are closer to the perturbation. This indicates that the filament response to the passing wave is not simultaneous for the whole structure. The movement rapidly reaches its maximum displacement, approximately at $t = 0.46\,\mathrm{min}$ (top middle panel), the motion reverses and the prominence starts to oscillate transversely. The right maximum displacement is again reached approximately at $t = 1.28\,\mathrm{min}$ so that we obtain a very short oscillation period for the transverse oscillation. At $t = 2.33\,\mathrm{min}$ (bottom right panel) we can see that the motion has been moving along the filament spine so that the density isocontours start to deform throughout the whole structure.

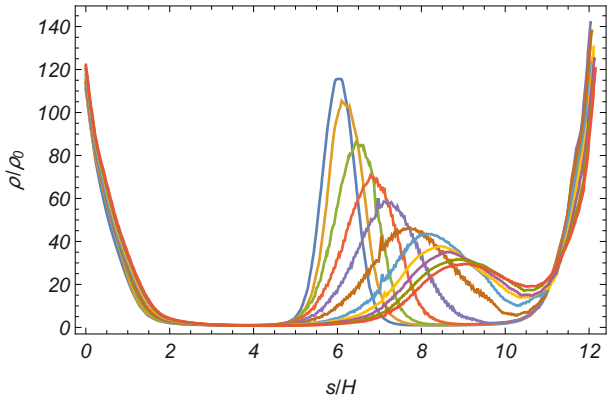

Figure 3.9: Time evolution of the density profile along the red coloured magnetic line of Figures 3.6 and 3.7. The time of each curve corresponds to the time step of Figure 3.6. The chromosphere-corona transition region is shown at the feet of the filled lines.

After some cycles the prominence plasma starts to flow downwards along the magnetic field lines. This process is clearly observed in the 3D Figures 3.6 and 3.7. At $t = 17.5\,\mathrm{min}$ (top middles panel) the direction of flux is not well defined yet, but at $t = 35.0\,\mathrm{min}$ (top right panel) we can see that the movement is produced only at one edge of the filament. In the second row of Figure 3.7 the movement along the magnetic field lines is visible. The prominence foot apparently remains unperturbed and only the upper parts of the structure eventually fall. For the longitudinal movement we do not see that the motion reverses, meaning that we cannot identify a clear oscillatory event. However, when we observe the movie of the simulation we can discern plasma rebounds during the drop. These rebounds have also been detected by other authors in observations or in studies of prominence formation by thermal evaporation/condensation processes in one-dimensional curved flux tubes without or with shallow dips. For example, Luna et al. (2012b) described that most of the blobs formed in their shallow-dip or loop shaped model of tubes 'slow down as they approach the tube feet,

and in some cases several bounces occur before they fall finally to the chromosphere'. de Groof et al. (2005) observed bright blobs of plasma falling along magnetic field lines. They found that when the falling blobs encounter the transition region, they 'slow down or even bounce back, before they reach the solar surface'. The downward flows along the magnetic field lines are clear in Figure 3.9, which shows the time evolution of the density profile along the red coloured field line plotted in Figures 3.6 and 3.7. We can see how the prominence structure is initially placed at the centre of the field line, around $s = 6\,H$, but it rapidly moves towards one of the feet.

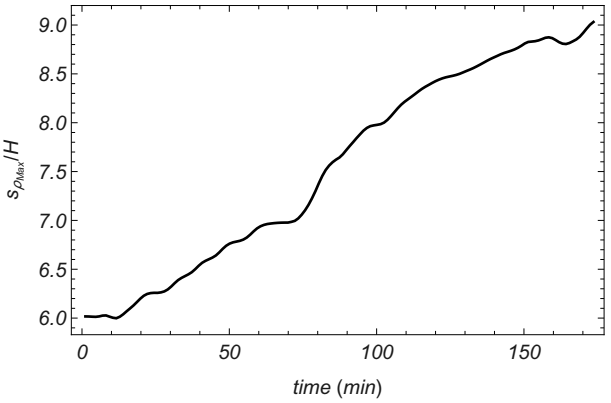

Figure 3.10: Time evolution of the maximum prominence density along the red magnetic field line of Figures 3.6 and 3.7.

In Figure 3.9 we also see that the peak of the density decreases but its width increases, meaning that the prominence width grows during the drop. Figure 3.10 shows the displacement of the density peak as a function of time. As we saw in Figure 3.8, at the beginning of the simulation the prominence body remains located at the original position. Around $t = 12\,\mathrm{min}$, the prominence starts to move until $t \approx 60\,\mathrm{min}$. At this point the displacement stops at approximately 10 min, exhibiting the rebound previously mentioned. At the end of the simulation, around 160 min, we clearly see a second bounce. The mean velocity of the drop is $2.9\,\mathrm{km\,s^{-1}}$, with a maximum peak of $10\,\mathrm{km\,s^{-1}}$ at $t = 80\,\mathrm{min}$. These velocities are smaller than the reported values from observations (Schrijver 2001; De Groof et al. 2004) and simulations. Luna et al. (2012b) investigated the process of formation and subsequent evolution of prominence plasma in one-dimensional magnetic arcades. They found that after the formation, the plasma moves along the field lines with a mean value of $34.2\,\mathrm{km\,s^{-1}}$ for quasi horizontal motions and $51.0\,\mathrm{km\,s^{-1}}$ for quasi vertical falling blobs. In a similar work, Müller et al. (2004) found flow velocities of the order of $100\,\mathrm{km\,s^{-1}}$. Nevertheless, while the falling plasma of these studies is in individual blobs, in our case the falling plasma is a portion of a 3D curtain-shaped structure whose feet are anchored to the chromosphere so that the dynamics must be different. Actually, Zirker et al. (1998) observed counter-streaming flows along closely vertical prominence barbs at speeds of $5 - 20\,\mathrm{km\,s^{-1}}$, and Berger et al. (2008) reported downflow streams that occur in a hedgerow prominence with speeds of $10\,\mathrm{km\,s^{-1}}$, which are velocities values that are closer to our results but a detailed comparison is out of the scope of the present study.

Besides the oscillatory and downward motions, Figure 3.7 shows a decrease of the density

that matches in space the location where the perturbation was initially placed. This density dimming remains static at its original position for all the simulation. It is a straightforward effect of the sudden perturbation we imposed, that can change the background equilibrium. The magnetic field and the density are coupled through the frozen condition (see Section 1.3.1) and so the plasma motion must conserve the magnetic flux. This implies that the ratio between the magnetic field and the density, co-moving with the fluid, is ideally constant. Another magnitude that is conserved for adiabatic processes is entropy, and for perpendicular propagation there is a balance between gas and magnetic pressure. Under these conditions a positive pressure perturbation, as in the present case, produces a decrease in the final density. This decrease of the density can be associated to parts of the coronal dimming observed in flares.

3.3 Hood & Anzer model

The aim of this chapter is to investigate oscillations triggered by external waves in prominences embedded in sheared magnetic fields. We have seen that the chosen sheared magnetic arcade model does not allow to keep mass suspended since it eventually falls down towards the photosphere. For this reason, we decided to investigate other prominence models. We focussed on the H&A prominence model (see Section 1.3.3). In this model we can impose a magnetic shear in the structure without losing the magnetic dips, relevant for the magnetic support. This model is initially in a magnetohydrostatic equilibrium meaning that the relaxation phase is not necessary. In any case, we have checked that the structure is in numerical equilibrium with only very small flows due to the grid discretization. To obtain the initial magnetic configuration, we first have to numerically solve Equations (1.42) and (1.46). Then, the magnetic field is given by Equation (1.40) and the gas pressure by Equations (1.41) and (1.45). We have chosen the following temperature profile (scale height),

$$\Lambda(kx) = k\Lambda_{\rm c} + (k\Lambda_{\rm p} - k\Lambda_{\rm c}) \exp\left[-(kx/0.25)^4\right], \tag{3.7}$$

being the corona and prominence pressure scale heights $\Lambda_{\rm c} = RT_{\rm c}/(\tilde{\mu}g)$ and $\Lambda_{\rm p} = RT_{\rm p}/(\tilde{\mu}g)$, respectively. The coronal and prominence temperatures are $T_{\rm c} = 10^6\,{\rm K}$ and $T_{\rm p} = 10^4\,{\rm K}$, gravity acceleration is $g = 0.274\,{\rm km\,s^{-2}}$, the gas constant $R = 8,300\,{\rm m^2\,s^{-2}\,K^{-1}}$, and the mean molecular weight for a fully ionised plasma is $\tilde{\mu} = 0.5$. The pressure scale height profile is represented in Figure 3.11.

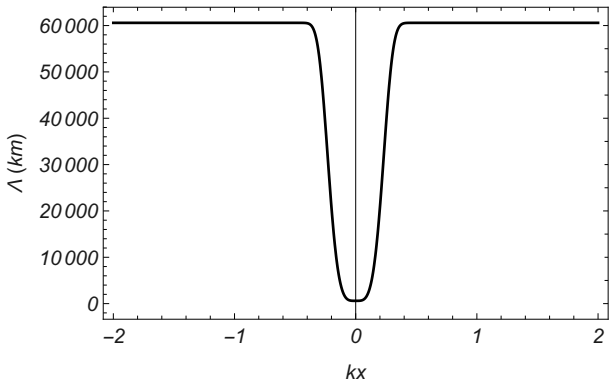

Figure 3.11: Pressure scale height as a function of position across the prominence body.

We select the dimensions to scale k so that $k\Lambda_c = 0.5$, and velocity is normalised to the Alfvén speed $v_A = 1,000\,\mathrm{km\,s^{-1}}$. For a typical prominence we set the initial parameters $X(x=0) = X_0 = 1$, $Z(x=0) = 0$, $P(x=0) = c_{s0}^2/\gamma$, being $\gamma = 5/3$ and the square of the reference sound speed $c_{s0}^2 = \Lambda_c \gamma g$. Finally, the density can be determined as $\rho = p/(\Lambda(kx)g)$. The initial configuration is plotted in the top left panel of Figure 3.12.

Once we have the initial configuration, we apply a perturbation to trigger the oscillations. To numerically solve the MHD equations we utilised again the MoLMHD code. Note that the configuration studied in this section is 2D now. Line-tying conditions are applied at all the boundaries of the numerical domain that consists of a box of 270×135 mesh points. The dimensions of the box are determined by the lateral dimension of the arcade, which is defined as the point where the x-component of the magnetic field is null. For this set of parameters we obtained that the half of the arcade is $x_a \approx 1.76/k = 213\,\mathrm{Mm}$, therefore the resolution of the system is about 1.58 Mm.

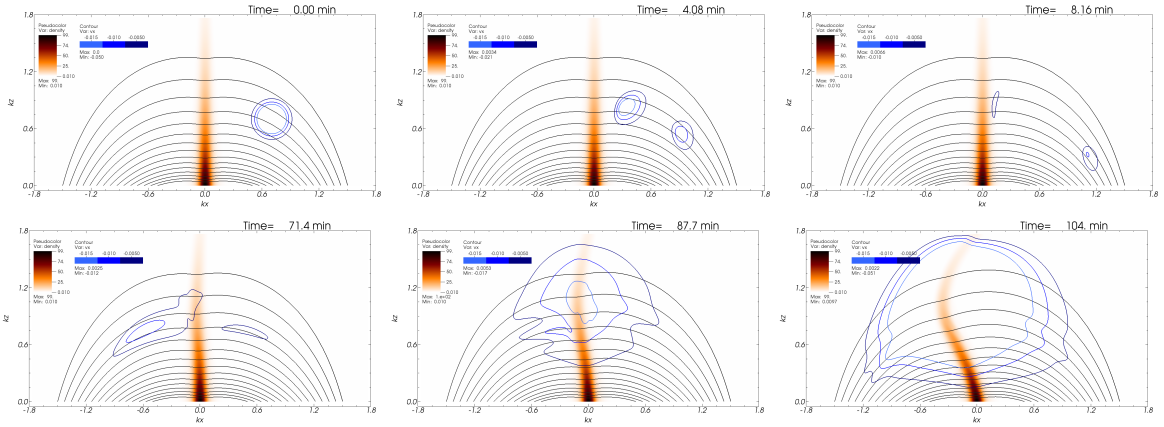

Figure 3.12: Time evolution of density, magnetic field lines, and v_x for a Hood & Anzer prominence model. v_x is normalised to $v_A = 1,000\,\mathrm{km\,s^{-1}}$ and density to $\frac{X_0^2}{\mu v_{A0}^2}$.

We start with a very simple case: an unsheared structure ($\alpha = 0$) so that the y-component of the magnetic field is zero. A simple external velocity perturbation points in the x-direction in order to trigger longitudinal oscillations (see top left panel of Figure 3.12). For this case we did not use the disturbance previously described in Section 3.2.2. The spatial distribution of the pulse is a two-dimensional Gaussian whose initial amplitude is $v_0 = 50\,\mathrm{km\,s^{-1}}$. In the top row of Figure 3.12 we can see the first time steps of the simulation. The pulse splits in two parts, one part goes towards the dense plasma and the second one falls down along the magnetic field lines. At $t = 8.16\,\mathrm{min}$ the pulse impacts the prominence. As the heavy prominence apparently does not respond to the passing wave we might think that the initial velocity amplitude of the pulse is not high enough. However, some time after the impact (bottom row of Figure 3.12), the prominence starts to move towards the left. As we saw in Chapter 2 we expected that the motion reverses triggering longitudinal oscillations. However, the prominence body falls down along the field lines and a gravitational instability inevitably grows (see blue coloured curves). We have repeated the simulation for different configurations and for different shear angles obtaining the same effect. As a result of the simulations, we conclude that the H&A model is not stable to lateral displacements although it contains magnetic dips.

3.4 Conclusions and discussion

We studied the dynamics of prominences perturbed by an external shock wave for two different model of prominences. First we numerically studied a curtain-shaped prominence anchored in a chromospheric layer that connects to an isothermal stratified corona and it is permeated by a strongly sheared magnetic arcade. As a consequence of the shear, the magnetic filled lines have shallow dips at the bottom of the structure or even lines with no dips at higher heights. Despite the lack of dips in the magnetic field, the system reaches an static equilibrium before introducing the perturbation. Once we reach a relatively relaxed situation we instantaneously introduce an external transverse perturbation to mimic a typical observed excitation event such as an EIT wave. The shock wave rapidly impacts the dense body activating different motions. We distinguish two phases: a short oscillatory stage and longer phase of downflows and sort of lack of equilibrium.

Once the wave impacts the dense plasma it starts to oscillate perpendicularly to the magnetic field lines. The magnetic field is frozen to the plasma so that the motion transports the lines with the flow. The transverse oscillatory period is of the order of 1 min, which is a very short compared to the transverse periods obtained in Chapter 2 or in other numerical studies (Luna et al. 2016b; Zhou et al. 2018), of the order of $5 - 10$ min. However, very short oscillatory periods ($1 - 5$ min) in prominences have also been detected (Tsubaki et al. 1987; Blanco et al. 1999; Okamoto et al. 2007).

The second phase consists of plasma downflows. The transverse oscillations destabilises the plasma configuration in such a way that a part of the filament moves downwards along the magnetic field lines. During this process no clear oscillatory pattern is observed, however we can discern plasma bounces. Only the edge of the filament where the shock wave hits the plasma drops. We obtained that the velocity of the downflow is $2.9\,\mathrm{km\,s^{-1}}$. This speed is too slow to consider the flow as a falling blob of coronal rain, however we can compare the motion with the movements along the filament barbs. As the prominence falls, the coronal plasma is compressed increasing the gas pressure below the flow front as they approach the chromosphere. The pressure gradient may decelerate the downward flows and cause the observed rebounds.

The second prominence model utilised to study prominence oscillations triggered by external perturbations is the H&A model. This is a 2.5D prominence model, with normal polarity, in which all the vectors have three spatial components but there is no dependence on the y-coordinate. The magnetic dip is the result of the equilibrium between magnetic and gravitational forces. Once we apply an external velocity pulse to trigger oscillations along the magnetic field lines, we expected that the prominence would describe an oscillatory motion, at least for some choices of the parameters. However, we found that the prominence mass always drops. The column of plasma does not fall as a rigid body but drops at different speeds depending on the height. As the prominence falls, the pressure increases below, but now the increase of the pressure gradient is not sufficient to decelerate the motion so that a velocity instability grows exponentially.

As a result of the two studies the question that arises is whether a gravitational equilibrium is possible under the absence of magnetic dips. Note that in the model used in Chapter 2 we did not find this gravitational instability. This is the main point that is addressed in the following two chapters of this Thesis.

Part II

Gravitational instabilities in threads

Chapter 4

Curved magnetic fields without dips [2]

4.1 Introduction

The solar atmosphere shows a variety of dynamic structures much denser than the background corona. These formations, guided by the curved magnetic field and most likely created by thermal instabilities or non-thermal equilibrium, have their own dynamics and are undoubtedly affected by the gravity force. Examples of such configurations are solar prominences, like those studied in Chapters 2 and 3, and introduced in Chapter 1, or coronal rain among others.

High-resolution observations show that the prominence body is composed of a bunch of individual threads of plasma. Each of these threads is embedded along a magnetic flux tube, so that the structure of a prominence thread can be modelled as one dimensional hydrodynamic problem. The magnetic field of these models is not taken into account explicitly since the magnetic field is not affected by the plasma dynamics. This assumption is more in accordance with active prominences due to their stronger magnetic fields. Prominence threads are not the only dense plasma structure we can observe along magnetic flux tubes. Loop-like magnetic structures also work as paths for falling blobs of coronal rain (Antolin & Rouppe van der Voort 2012; Antolin et al. 2012), so that the model presented in this work could be applied to any low-beta plasma structure in the solar atmosphere where field-aligned instabilities of density enhancement can occur, e.g. coronal rain. The shape of a curved magnetic flux tube with (or without) dips is represented by the definition of the projected gravity along the magnetic field line. This type of model has been utilised in many studies such as numerical simulations of prominence formation (Dahlburg et al. 1998; Luna et al. 2012b; Zhou et al. 2014), simulations of longitudinal oscillations in solar prominences (Luna & Karpen 2012; Zhang et al. 2012, 2013), or in the theoretical study of normal modes in prominence oscillations (Luna et al. 2012a). The next step is the study of the gravitational stability of these threads.

A common method to study the stability of a system is based on the frequency analysis of

[2]This chapter is based on: Adrover-González, A., Terradas, J., Oliver, R., Carbonell, M.; *Gravitational instability of solar prominence threads: I. Curved magnetic fields without dips*, Astronomy and Astrophysics, accepted for publication.

the oscillatory modes. An alternative method to study the stability of a system is based on bifurcation theory. This is a mathematical study that, given a specific dynamical system, determine whether or not the existing equilibrium points, also called fixed points (hereafter we mostly use this notation), are stable when key parameters of this system vary. Changes of the stability of equilibrium points take place at the bifurcation points. At these bifurcations, the system can create or destroy pairs of equilibrium points. In solar physics, bifurcation theory has been applied to the study of creation or annihilation of magnetic null points in the solar corona (see Priest et al. 1996, 1997; Brown & Priest 2001).

In this chapter we comprehensively investigate the gravitational instability by using a very simple configuration. This allows us to disentangle the main physical processes that occur in the system. We consider a circular magnetic flux tube in which gravity has a spatially varying parallel component along the field lines. We use elementary physics describing a plasma in this configuration, the interplay between gas pressure and gravity force. Magnetic field is assumed not to change due to the presence of the density enhancement or thread, and it simply acts as a guide for the longitudinal motions. We do not include non-ideal effects that are most likely important in the solar corona (and chromosphere), because in our opinion, the purely mechanical situation under line-tying conditions in the absence of dissipative mechanisms has received little attention in the literature and needs to be understood more deeply. We start with a magnetic flux tube without the presence of a magnetic dip. The effect of magnetic dips will be addressed in Chapter 5.

4.2 Background equilibrium solution

We start with the description of our model. We assume that the shape of the magnetic field is circular. Among other implications this means that the flux tube along a given field line has constant cross-section, A_0, since the distance between two field lines is constant along the field (see dotted curves in Figure 4.1 top panel). As a consequence, the magnetic tube geometry reduces to a 1D problem for which we analyse the gravitational stability in the direction of the magnetic field. In spite of the ambiguity, all through this and next chapter we refer to our model as a magnetic flux tube. We denote by s the coordinate along the tube, starting from the left foot. The total length of the magnetic tube is L and the top or apex is located at $s = L/2$. Gravity is pointing downwards and the projection along the field lines in this circular configuration is

$$g_{\parallel}(s) = -g \cos\left(\pi \frac{s}{L}\right), \tag{4.1}$$

being the radius of the field line $R = L/\pi$. The hydrostatic equation along the tube is simply

$$\frac{dp}{ds}(s) = \rho(s)\, g_{\parallel}(s), \tag{4.2}$$

meaning that the pressure derivative with position must balance the projected gravity force along the field lines. Since we assume an isothermal atmosphere the sound speed, c_{s0}, is constant and we write

$$p(s) = \frac{c_{s0}^2}{\gamma}\rho(s), \tag{4.3}$$

where $\gamma = 5/3$. Introducing this expression into Equation (4.2) we find the following simple differential equation

$$\frac{d\rho}{\rho} = \frac{\gamma}{c_{s0}^2} g_{\parallel}(s) ds, \tag{4.4}$$

which is integrated directly to give

$$\rho(s) = \bar{\rho}_0 \exp\left[-\frac{\gamma g}{c_{s0}^2} \frac{L}{\pi} \sin\left(\pi \frac{s}{L}\right) \right], \tag{4.5}$$

being $\bar{\rho}_0$ the reference density at $s = 0$ and $s = L$, i.e., at the footpoints of the magnetic tube. According to Equation (4.3) gas pressure and density have the same dependence with the coordinate s.

4.3 Equilibrium solutions containing threads

A stratified prominence unbounded with height, as for example, in the Hood & Anzer (1990) model (see Chapters 1 and 3), can be seen as a continuous collection of threads stacked in the vertical direction but located at magnetic dips. It is crucial to understand the stability of a density enhancement or equivalently a thread in the solar atmosphere even in the absence of magnetic dips as we have explained in Section 4.1.

The idea is to analyse the simple situation of a finite mass (called generically a thread, hereafter) with density ρ_t located on the curved magnetic field (see Figure 4.1 for a sketch of the model). The question is whether this equilibrium is stable or unstable and we investigate the conditions in which the system allows equilibrium solutions at lower heights.

The basic equation of our system is the momentum equation

$$\rho_t \frac{d^2 s}{dt^2} = -\frac{dp}{ds}(s) + \rho_t \, g_{\parallel}(s), \tag{4.6}$$

being s the coordinate of the centre of the thread along the curved path. Since the thread is surrounded by plasma, fluctuations in gas pressure at the edges of the thread in the longitudinal direction create a net force. We need to provide an expression for the gas pressure derivative. The other force existing in the system is the gravity projection along the magnetic field line given in Equation (4.1). Before we go into the details about the calculation of the gas pressure derivative it is necessary to describe the general features of our system from the mathematical point of view.

In order to analyse the stability of the system we write Equation (4.6) as the vector field

$$\begin{pmatrix} \dot{s} \\ \dot{v} \end{pmatrix} = \begin{pmatrix} v \\ -\frac{1}{\rho_t}\frac{dp}{ds}(s) + g_{\parallel}(s) \end{pmatrix}, \tag{4.7}$$

where the dot represents the time derivative. The system has equilibrium or fixed points when

$$\begin{aligned} v &= 0, \\ -\frac{1}{\rho_t}\frac{dp}{ds}(s) + g_{\parallel}(s) &= 0, \end{aligned} \tag{4.8}$$

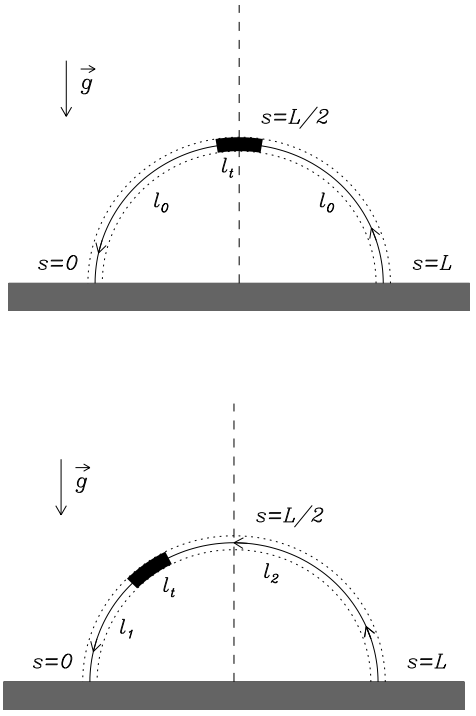

Figure 4.1: Sketch of the basic model. The upper panel corresponds to the situation in which the plasma thread, represented by the dark rectangle of length $l_{\rm t}$, is located at the tube apex. This configuration is in an equilibrium that can be stable or unstable. The lower panel represents a new equilibrium of the thread at a lower height. The curved magnetic field is uniform and directed along the tube axis. The gravity force is pointing downwards and is projected along the field line according to Equation (4.1). The footpoints are supposed to be anchored at the base of the corona, represented by the shaded grey area.

and the corresponding solution for the position is denoted as $s_{\rm e}$ (the velocity at the equilibrium point is always zero). The linearised version of Equation (4.7) is

$$\begin{pmatrix} \dot{s} \\ \dot{v} \end{pmatrix} = \mathbf{A} \begin{pmatrix} s \\ v \end{pmatrix}, \tag{4.9}$$

where the matrix $\mathbf{A}$ is the Jacobian,

$$\mathbf{A} = \begin{pmatrix} \frac{\partial \dot{s}}{\partial s} & \frac{\partial \dot{s}}{\partial v} \\ \frac{\partial \dot{v}}{\partial s} & \frac{\partial \dot{v}}{\partial v} \end{pmatrix} = \begin{pmatrix} 0 & 1 \\ f(s) & 0 \end{pmatrix}, \tag{4.10}$$

where

$$f(s) = \frac{d}{ds}\left[-\frac{1}{\rho_{\rm t}}\frac{dp}{ds}(s) + g_{\parallel}(s)\right]. \tag{4.11}$$

The eigenvalues of $\mathbf{A}$ at the equilibrium points ($s = s_{\rm e}$) provide valuable information about their stability. If $f(s_{\rm e}) > 0$ we have

$$\lambda_{\pm} = \pm\sqrt{f(s_{\rm e})}. \tag{4.12}$$

In this case the fixed point is a saddle point since we have real values with opposite signs (e.g., Jordan & Smith 1987). This point is unstable.

If $f(s_e) < 0$ (in this case the linearised system is exactly the same as that of the simple harmonic oscillator equation), the eigenvalues are

$$\lambda_{\pm} = \pm i \sqrt{|f(s_e)|}. \tag{4.13}$$

This corresponds to a linear centre which is a stable point. The last case is when $f(s_e) = 0$, this is a degenerate case but still provides information about the stability of the equilibrium points.

4.3.1 Thread initially at the tube apex

We analyse first the situation of the thread initially located at the top of a curved magnetic field (see Figure 4.1 top panel). This mass is in equilibrium since the gravity force is zero at $s = L/2$ (see Equation (4.1)), and the gradient of the background pressure is zero at the tube apex (see Equations (4.3) and (4.5)). The goal is to obtain an approximation for the pressure derivative in Equation (4.8) once the thread has moved from the initial equilibrium position. In our model we apply line-tying conditions, meaning that pressure fluctuations are not lost along the field lines at the base of the corona. There is no energy leakage through the footpoints and mass flows along the magnetic tube injected from the photosphere are not allowed. Therefore we have perfect reflection at these points because of the big difference in density between the photosphere and corona. It is important to remark that this specific boundary condition allows us to have suspended threads at a given height even in the absence of magnetic dips and that the presence of a chromospheric layer (not included in our model) may affect how the pressure is balanced along the tube.

We denote the length of the thread as l_t and by a simple geometrical reasoning $l_t/2 < s < L - l_t/2$ since the thread edge cannot connect with the base of the corona. Under equilibrium at $s = L/2$ the length of the external part of tube that contains the thread is $l_0 = L/2 - l_t/2$ along each loop leg (see Figure 4.1 top panel). We have the simple relation $L = 2l_0 + l_t$. Now we assume that the thread has moved to another location along the magnetic field (see Figure 4.1 bottom panel). The distance on the left part is l_1 now (different from l_0), while the distance on the right part is l_2. We have that $l_1 = s - l_t/2$, and $l_2 = L - l_1 - l_t = L - s - l_t/2$. Quiescent prominences are typically $100 - 200$ Mm long (L) and are about 100-fold denser than the surrounding corona (ρ_t/ρ_0). However, it is known that the entire bodies of prominences consist of a collection of individual short threads of plasma located in long field lines so that only a fraction of each field line (l_t) is filled with dense plasma. Observations show that the typical thread length ranges from 0.3 Mm to 20 Mm (Lin et al. 2005; Mackay et al. 2010). On the other hand, the length of blobs of coronal rain is shorter and ranges approximately between 0.2 Mm and 2.4 Mm with a distribution pick around $0.5 - 0.6$ Mm (Antolin & Rouppe van der Voort 2012; Antolin et al. 2012). In this study a wide range of the thread parameters will be utilised to exemplify a vast sort of prominence threads (see Mackay et al. 2010; Engvold 2015, for a detailed description of solar prominences).

Since the system is assumed to be dissipationless we consider that the evolution during the

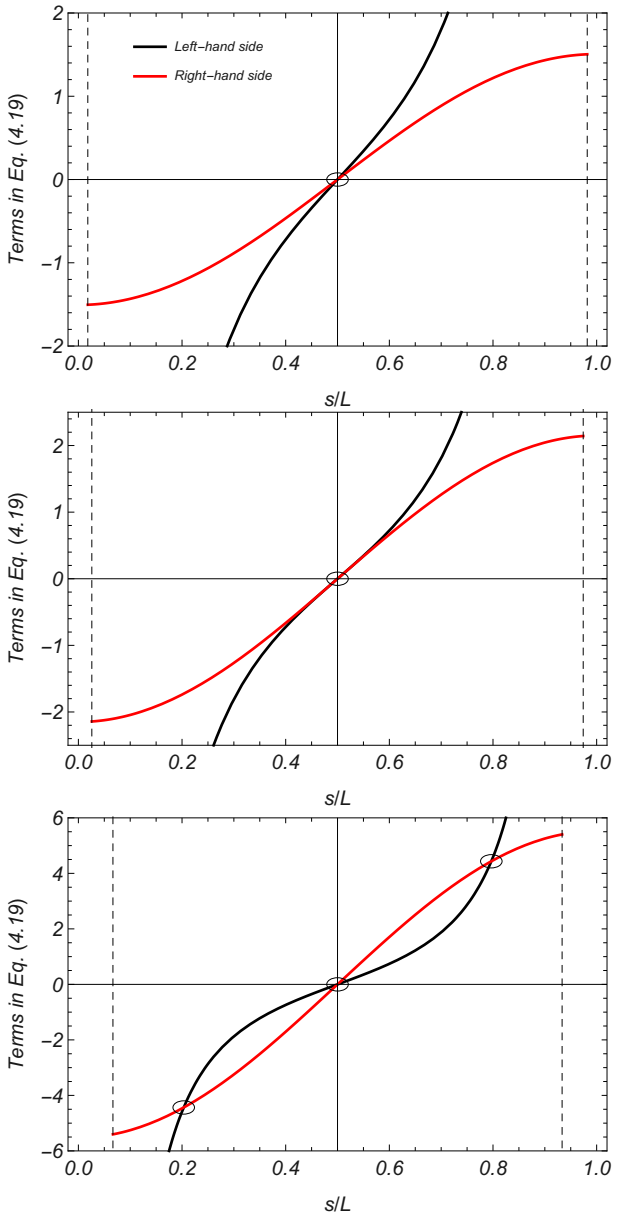

Figure 4.2: Left- (black line) and right- (red line) hand sides of Equation (4.19) as a function of s/L, for three different values of l_t. In the top panel the system is linearly stable with one solution (see circle). On the bottom panel the system relaxes to a new equilibrium at a lower height (see the two complementary solutions) and the trivial solution becomes an unstable solution. In all cases $L = 10\,H$ and $\rho_\mathrm{t} = 100\,\rho_0$; $l_\mathrm{t} = L/110$ (top panel), $l_\mathrm{t} = l_\mathrm{tb}$ (middle panel) and $l_\mathrm{t} = L/30$ (bottom panel). The value $l_\mathrm{tb} \approx L/77.08$ is obtained when the derivatives of the two curves at $s = L/2$ are the same (see Equation (4.20)). The vertical dashed lines represent the edges of the domain of the variable s, namely $s = l_\mathrm{t}/2$ and $s = L - l_\mathrm{t}/2$.

motion of the thread is adiabatic. The behaviour of the plasma in the evacuated parts of the tube, i.e., where the density is low, is similar to that of a piston because of the line-tying conditions at the footpoints. The gas pressure can be written as the background, stratified

due to gravity, plus a term that depends on the position of the thread. The key idea here is to apply the adiabatic law to each part of the tube but to this term only, removing the contribution from the background,

$$\begin{aligned} p_1 \left(l_1 A_1\right)^\gamma &= p_0 \left(l_0 A_0\right)^\gamma , \\ p_2 \left(l_2 A_2\right)^\gamma &= p_0 \left(l_0 A_0\right)^\gamma , \end{aligned} \tag{4.14}$$

where p_0 represents the reference pressure before the thread has moved, changing the length of the evacuated part from l_0 to l_1 and pressure from p_0 to p_1 for the left part. For the right part we have changes from l_0 to l_2 and from p_0 to p_2. Since we are considering a perfectly circular geometry we have that $A_0 = A_1 = A_2$ and the cross-sectional areas cancel in the previous expressions. Now from Equation (4.14) we obtain that

$$\begin{aligned} p_1(s) &= p_0 \left(\frac{l_0}{l_1}\right)^\gamma = p_0 \left(\frac{L/2 - l_\mathrm{t}/2}{s - l_\mathrm{t}/2}\right)^\gamma , \\ p_2(s) &= p_0 \left(\frac{l_0}{l_2}\right)^\gamma = p_0 \left(\frac{L/2 - l_\mathrm{t}/2}{L - s - l_\mathrm{t}/2}\right)^\gamma . \end{aligned} \tag{4.15}$$

At this point we impose the condition that the plasma thread has to be in static and stationary equilibrium, i.e., no flows are allowed and the solution does not change in time. These conditions imply that Equation (4.7) reduces to Equation (4.8). To simplify things we assume that the thread does not change its shape and keeps its length, l_t, constant. Now we approximate the gas pressure derivative that appears in Equation (4.8) as

$$\frac{dp}{ds}(s) \approx \frac{\Delta p}{\Delta s}(s) = \frac{p_2(s) - p_1(s)}{l_\mathrm{t}}. \tag{4.16}$$

Since the thread has a finite length, gravity changes along it, therefore this term is approximated by the average gravity on the thread

$$\bar{g}_\parallel(s) = \frac{1}{l_\mathrm{t}} \int_{s-l_\mathrm{t}/2}^{s+l_\mathrm{t}/2} g_\parallel(s) ds = -g \, \frac{2}{\pi} \, \frac{L}{l_\mathrm{t}} \sin\left(\frac{\pi}{2} \frac{l_\mathrm{t}}{L}\right) \cos\left(\pi \frac{s}{L}\right) . \tag{4.17}$$

Since under typical conditions $l_\mathrm{t} \ll L$, using the Maclaurin expansion of the sinus for small arguments, we recover exactly $g_\parallel(s)$ in the previous expression. Hereafter, to simplify things we use $g_\parallel(s)$ from Equation (4.1) instead of Equation (4.17).

The hydrostatic equation for the thread is therefore

$$\frac{p_2(s) - p_1(s)}{l_\mathrm{t}} = \rho_\mathrm{t} \, g_\parallel(s). \tag{4.18}$$

Using Equation (4.3) for the sound speed together with the previous expressions for pressure and gravity we obtain the following equation for s, representing the location under static equilibrium of the dense thread along the tube,

$$\left(\frac{L/2 - l_\mathrm{t}/2}{L - s - l_\mathrm{t}/2}\right)^\gamma - \left(\frac{L/2 - l_\mathrm{t}/2}{s - l_\mathrm{t}/2}\right)^\gamma = -\frac{\gamma}{c_{\mathrm{s}0}^2} \frac{\rho_\mathrm{t}}{\rho_0} \, g \, l_\mathrm{t} \, \cos\left(\pi \frac{s}{L}\right) , \tag{4.19}$$

where $c_{s0}^2 = \gamma p_0/\rho_0$, and ρ_t/ρ_0 corresponds to the density contrast between the thread and the density background at $s = L/2 - l_t/2$. The parameter ρ_t/ρ_0 must be much larger than one since we are not taking into account any energy flux through the thread and its mass and length are assumed to be constant.

Equation (4.19) is a transcendental one and it has to be solved numerically. To search the numerical solution of Equation (4.19) we used the *Findroot* command of Mathematica[1] (Wolfram Research 2020). From now on we denote s_e a solution of Equation (4.19). It is easy to verify that $s_e = L/2$ is a solution for any values of the parameters. Hence, there is always an equilibrium solution at the tube apex ($s_e^{\mathscr{A}} = L/2$) that can be stable or unstable. Furthermore, the symmetry of the model with respect to $s = L/2$ implies that if there are additional solutions, they will appear in pairs ($s_e^{\mathscr{L}}, s_e^{\mathscr{R}}$) verifying $s_e^{\mathscr{L}} + s_e^{\mathscr{R}} = L$, i.e. the solutions will be distributed symmetrically with respect to $s = L/2$, one on the left ($s_e^{\mathscr{L}}$) and the other on the right part ($s_e^{\mathscr{R}}$) of the tube.

To understand the nature of the these possible situations we have plotted in Figure 4.2 the left- and right-hand side terms of Equation (4.19) as a function of s, for fixed parameters L, c_{s0}, g, ρ_t/ρ_0, and varying l_t using the projected gravity given in Equation (4.1). The gravity acceleration is $g = 0.274\,\mathrm{km\,s^{-2}}$, and we take a spatial reference length of $H = 10,000\,\mathrm{km}$. The sound speed takes a value of $c_{s0} = 166\,\mathrm{km\,s^{-1}}$ for a fully ionised coronal tube with $10^6\,\mathrm{K}$ temperature. When the two curves cross (see circles) we have a solution at that particular point. On the upper panel we have only one solution, the trivial one at $s_e^{\mathscr{A}} = L/2$, while on the bottom panel three solutions appear, the trivial one plus two complementary solutions. As we will see in Section 4.4, in the first situation the mass will remain at its original position, and, upon being subject to a small disturbance, it will oscillate around this point because this equilibrium is stable. In the second situation, the mass is not stable at the initial position at the apex and after being perturbed it will move to one of the solutions along the legs which are energetically more favorable. The stability analysis performed here and in the following sections provides a simple criterion that tells us when a plasma thread is gravitationally stable or unstable.

The transition between one to three solutions is represented in the middle panel of Figure 4.2 and the mathematical condition is that the slopes of the curves are the same for the left- and right-hand sides of Equation (4.19),

$$\frac{(L/2 - l_t/2)^\gamma}{(L - s - l_t/2)^{\gamma+1}} + \frac{(L/2 - l_t/2)^\gamma}{(s - l_t/2)^{\gamma+1}} = \frac{1}{c_{s0}^2}\frac{\rho_t}{\rho_0}\, g\, l_t\, \frac{\pi}{L} \sin\left(\pi \frac{s}{L}\right). \tag{4.20}$$

Considering the following equation

$$f(s) = \frac{d}{ds}\left[-\frac{1}{\rho_t}\frac{dp}{ds}(s) + g_\parallel(s)\right] = 0, \tag{4.21}$$

and using the expressions for the pressure derivative (Equation (4.16)) and the projected gravity (Equation (4.1)) we obtain Equation (4.20). When Equation (4.20) or Equation (4.21) is satisfied together with Equation (4.19) the system is said to have a bifurcation point. We realise that the left-hand side term of Equation (4.21) is precisely the term inside the square

[1] https://www.wolfram.com/mathematica

root of the computed eigenvalues in Equations (4.12) and (4.13). We have shown that depending on the sign of $f(s_e)$ the nature of the equilibrium solutions changes. When $f(s_e)$ is positive (Equation (4.12)) the eigenvalue λ_- represents an exponentially damped solution that is eventually dominated by the growing solution in time associated to λ_+ of the form $\exp(\tau t)$ where the growth time is $\tau = \lambda_+$. When $f(s_e)$ is negative we have a stable linear centre with a harmonic time-dependence of the form $\exp(i\omega t)$ and frequency $\omega = \lambda_+/i$ (Equation (4.13)). In this case, it is known from linear theory of ODE systems that we cannot conclude that the equilibrium point is truly a centre since it could be also a stable or unstable spiral (e.g., Jordan & Smith 1987). Nevertheless, when the system is reversible or energy conservative (Hamiltonian), and in our case the two conditions are fulfilled, the linear centre is indeed a true centre (e.g., Strogatz 2018, Sections 6.5 and 6.6) and stability is ensured. In Section 4.4 we confirm using physical arguments that the equilibrium point is stable.

Let us discuss the results from the physical point of view. Figure 4.2 shows that the existence of the non-trivial solutions of Equation (4.19) depends on the thread model parameters. Figure 4.3 (top panel) shows the equilibrium position s_e as a function of ρ_t/ρ_0 for different values of L when the thread length is $l_t = 0.1\,H$. We obtain that the system only develops the $s_e^{\mathscr{L}}$ and the $s_e^{\mathscr{R}}$ solutions for values of ρ_t beyond ρ_{tb} (see thin dashed vertical line). When $\rho_t < \rho_{tb}$, meaning before the appearance of the bifurcation, $s_e^{\mathscr{A}}$ is the only equilibrium position, so that we are in the situation of the top panel of Figure 4.2 and therefore $s_e^{\mathscr{A}}/L = 0.5$ is stable. However, when the thread structure allows the existence of two complementary solutions, these are energetically more suitable so that $s_e^{\mathscr{A}}$, that remains located at $s_e/L = 0.5$ (see horizontal dashed lines in Figure 4.3 top panel), becomes an unstable solution. To distinguish between stable or unstable solutions, we represent in Figure 4.3 (and in the following figures) stable solutions as solid curves and unstable solutions as dashed curves. In addition, we realise that for the three values of L, $s_e^{\mathscr{L}}$ and $s_e^{\mathscr{R}}$ appear around the same bifurcation value ρ_{tb}. This means that the bifurcation density value from which we obtain an equilibrium out of the apex of the structure, does not strongly depend on the length of the magnetic tube. Note that s_e is normalised to H for normalisation purposes since if we keep the normalisation to L, the solutions of the three configurations overlap. This means that the normalised s_e/L does not depend strongly on L for this set of parameters. This feature is clearer in the bottom panel of Figure 4.3 where s_e as a function of L is plotted (when L is large the stable solutions are almost horizontal). Moreover, as was expected, the equilibrium position of the thread drops with increasing ρ_t. It is interesting to study the dependence of the equilibrium position on the thread length. Figure 4.3 (middle panel) shows s_e as a function of l_t/L for different values of L when $\rho_t/\rho_0 = 100$. For $L = 10\,H$ (black curve) we obtain that below the bifurcation $s_e = s_e^{\mathscr{A}}$ is the only solution of Equation (4.19) and this is stable, but when $l_t > l_{tb}$, $s_e^{\mathscr{A}}$ becomes unstable and the emerged branches $s_e^{\mathscr{L}}$ and $s_e^{\mathscr{R}}$ are stable. For $L = 15\,H$ and $L = 20\,H$ the bifurcation thread length is out of the plot and their $s_e^{\mathscr{A}}$ overlaps with that for $L = 10\,H$ at $s_e/L = 0.5$. In Figure 4.3 (middle panel) we also see that the equilibrium position of the thread changes along the magnetic tube when the thread length increases. Figure 4.3 (top and middle panels) shows the same behaviour for all sets of parameters, that consists in a sole stable solution for values below the bifurcation, and two symmetric stable solutions out of the apex plus an unstable solution at $s_e = L/2$ beyond the bifurcation point. However, Figure 4.3 (bottom panel) shows that for some set of parameters, the system does

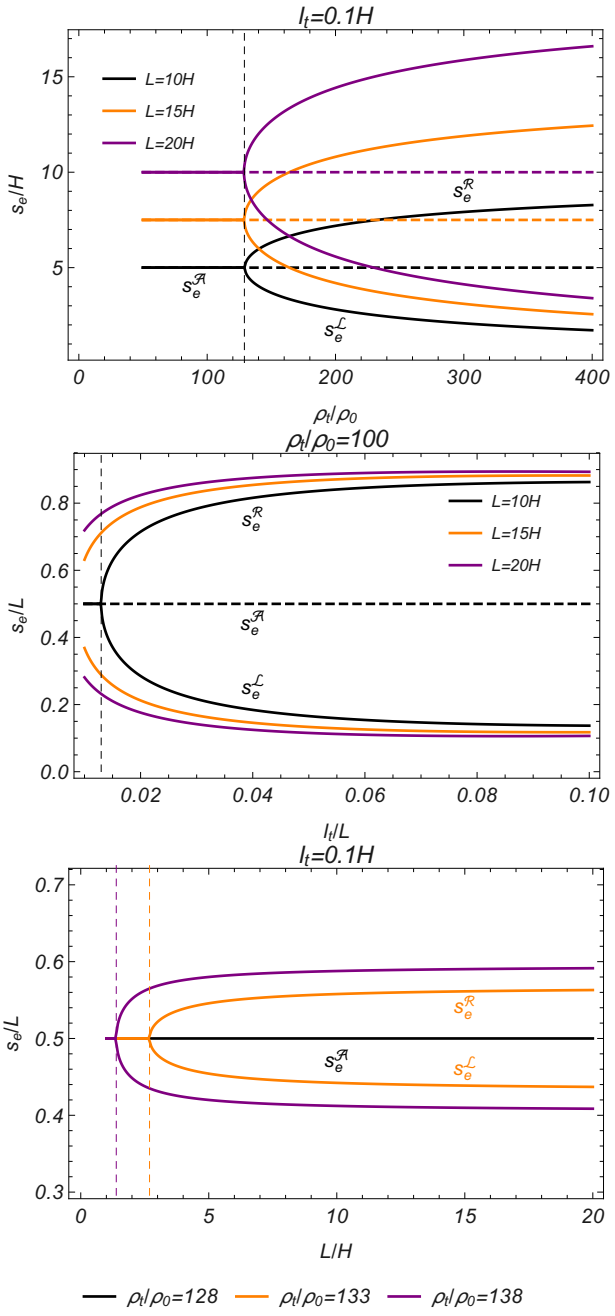

Figure 4.3: Solutions s_e of Equation (4.19) as a function of ρ_t/ρ_0 (top panel), l_t/L (middle panel), and L/H (bottom panel). Solid lines correspond to stable solutions and dashed lines to unstable ones. The thin vertical dashed lines correspond to the bifurcation values that have been calculated by solving Equations (4.19) and (4.20) simultaneously and coincide with the results in Equation (4.32) (top panel), Equation (4.33) (middle panel), and Equation (4.34) (bottom panel).

not present the $s_\mathrm{e}^{\mathscr{L}}$ and $s_\mathrm{e}^{\mathscr{R}}$ equilibria when L varies so that $s_\mathrm{e}^{\mathscr{A}}$ is always stable (see solid horizontal black line). Interestingly, the bottom panel of Figure 4.3 shows that for small changes of ρ_t, $s_\mathrm{e}^{\mathscr{L}}$ and $s_\mathrm{e}^{\mathscr{R}}$ vary significantly. Moreover, we see that the bifurcation length L_b for $\rho_\mathrm{t}/\rho_0 = 133$ and $\rho_\mathrm{t}/\rho_0 = 138$ is short, around $L_\mathrm{b} = 2.7\,H$ and $L_\mathrm{b} = 1.4\,H$, respectively.

These values are shorter than the typical magnetic tube observations.

More aspects about the bifurcation values and how to calculate them are given in Section 4.4. But it is interesting to finish this section by analysing the presented results from a dynamical systems perspective. The transition from one stable equilibrium solution to two symmetric stable solutions and one unstable solution is characteristic of the supercritical pitchfork bifurcation, see for example Section 3.4 of Strogatz (2018) or Section 20.1E of Wiggins (2003). This bifurcation is present in systems that have a symmetry, such as the one between the left and right sides of our magnetic tube when the thread is initially at the tube apex. In Figure 4.3 we find the same type of pitchfork bifurcation in the three panels (although in the bottom panel the unstable solutions, pink and orange curves, are overplotted by the stable one, black curve).

4.3.2 Thread initially at any location along the tube

It is straight forward to derive analytical expressions for the situation of a thread initially located at any position along the tube, denoted by s_0, and not necessarily at $L/2$ as discussed in the previous section. We simply need to rewrite Equation (4.15) as

$$\begin{aligned} p_1(s) &= p_0 \left(\frac{s_0 - l_\mathrm{t}/2}{s - l_\mathrm{t}/2} \right)^\gamma , \\ p_2(s) &= p_0 \left(\frac{L - s_0 - l_\mathrm{t}/2}{L - s - l_\mathrm{t}/2} \right)^\gamma , \end{aligned} \tag{4.22}$$

and the corresponding equilibrium equation analogous to Equation (4.19) is now,

$$\left(\frac{L - s_0 - l_\mathrm{t}/2}{L - s - l_\mathrm{t}/2} \right)^\gamma - \left(\frac{s_0 - l_\mathrm{t}/2}{s - l_\mathrm{t}/2} \right)^\gamma = -\frac{\gamma}{c_{\mathrm{s}0}^2} \frac{\rho_\mathrm{t}}{\rho_0} g\, l_\mathrm{t} \cos\left(\pi \frac{s}{L} \right) . \tag{4.23}$$

Equation (4.23) simplifies to Equation (4.19) when $s_0 = L/2$. Different types of representative solutions are shown in Figure 4.4 and in this case the parameter that has been chosen to change is ρ_t (in Figure 4.2 it was l_t). In these plots the initial position of the thread is $s_0 = 0.4/L$, therefore located on the left half section of the tube. The left-hand side of Equation (4.23) is not symmetric anymore with respect to the tube apex, and this allows the existence either of one, two or three solutions, according to Figure 4.4. But note that by continuity there must be a situation in these circumstances with two solutions when the left- and right-hand side curves are tangential. This case is calculated as in Section 4.3.1 by imposing that the spatial derivatives of the left- and right-hand sides of Equation (4.23) are equal,

$$\frac{(L - s_0 - l_\mathrm{t}/2)^\gamma}{(L - s - l_\mathrm{t}/2)^{\gamma+1}} + \frac{(s_0 - l_\mathrm{t}/2)^\gamma}{(s - l_\mathrm{t}/2)^{\gamma+1}} = \frac{1}{c_{\mathrm{s}0}^2} \frac{\rho_\mathrm{t}}{\rho_0} g\, l_\mathrm{t} \frac{\pi}{L} \sin\left(\pi \frac{s}{L} \right) . \tag{4.24}$$

So, Equation (4.24) has to be satisfied together with Equation (4.23) for the system to have two equilibrium solutions. An example of such a situation is found in Figure 4.4 middle panel. For simplicity, we still denote the equilibrium position at the left part of the tube as $s_\mathrm{e}^{\mathscr{L}}$, as $s_\mathrm{e}^{\mathscr{R}}$ at the right part, and as $s_\mathrm{e}^{\mathscr{A}}$ for the central near apex solution, so that when the system has only two equilibrium solutions, $s_\mathrm{e}^{\mathscr{R}} = s_\mathrm{e}^{\mathscr{A}}$ (or $s_\mathrm{e}^{\mathscr{L}} = s_\mathrm{e}^{\mathscr{A}}$). As in Section 4.3.1

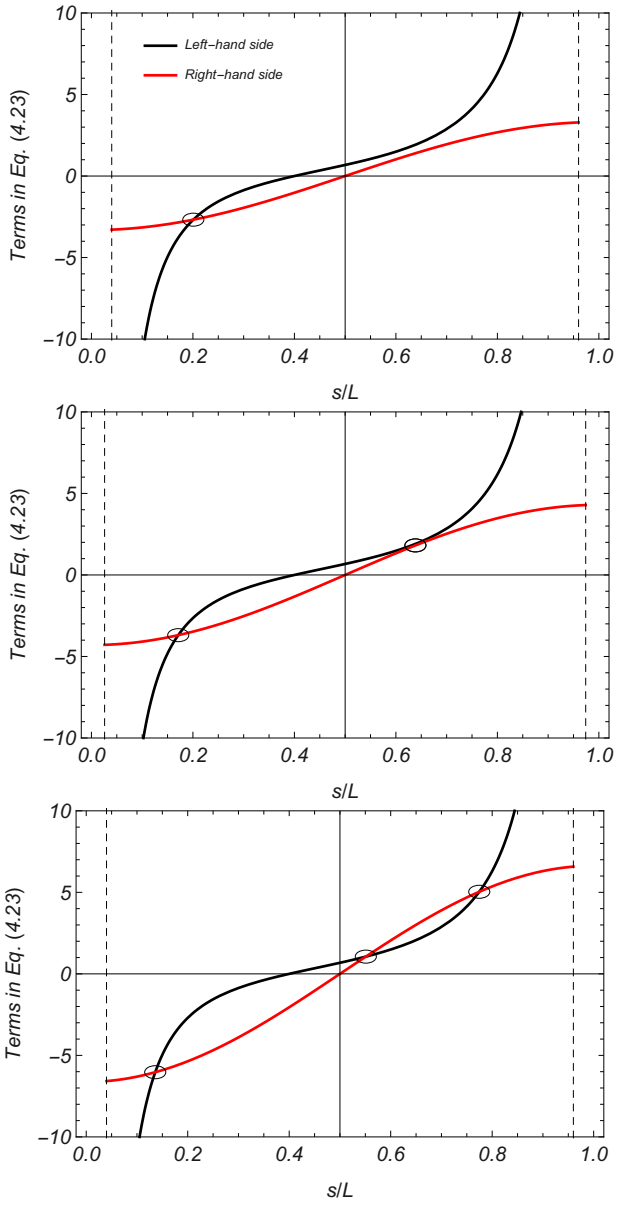

Figure 4.4: Left- (black line) and right- (red line) hand sides of Equation (4.23) as a function of s/L, for three different situations with one, two and three solutions. In these plots $s_0 = 0.4/L$ (where the black line crosses zero), $L = 10\,H$, $l_\mathrm{t} = L/50$; $\rho_\mathrm{t}/\rho_0 = 100$ (top panel), $\rho_\mathrm{t}/\rho_0 = \rho_{\mathrm{t_b}}/\rho_0$ (middle panel), and $\rho_\mathrm{t}/\rho_0 = 200$ (bottom panel). The value $\rho_{\mathrm{t_b}}/\rho_0 \approx 137.28$ is obtained from Equations (4.23) and (4.24). The vertical dashed lines represent the edges of the domain of the variable s, namely $s = l_\mathrm{t}/2$ and $s = L - l_\mathrm{t}/2$.

the sign of the difference between the left-hand side term and the right-hand side term of Equation (4.24) reveals the nature of the different solutions.

Now in the bifurcation diagram we find that the characteristic pitchfork for the symmetric case disconnects into two curves, one below $s_0/L = 0.5$ and another one above this value. An example is shown in Figure 4.5 (top panel) when the density contrast is changed. The lower curve is always stable, whereas the upper curve has both stable and unstable branches.

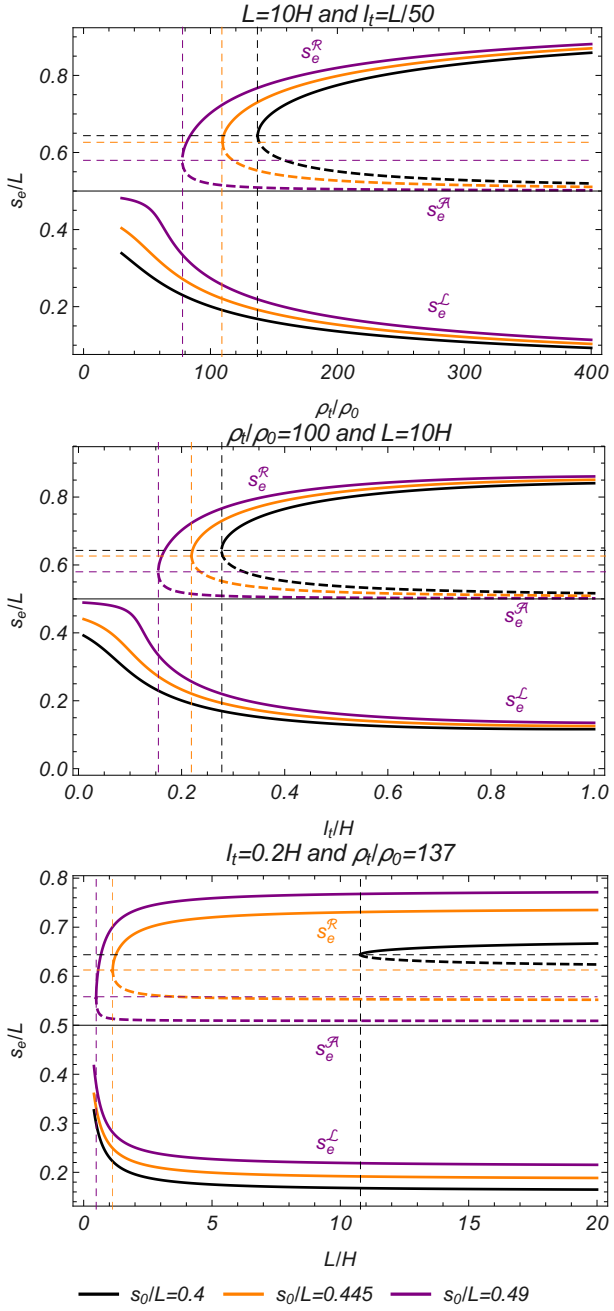

Figure 4.5: Same as Figure 4.3 but for Equation (4.23) and for different values of s_0/L. The bifurcation points (intersections between vertical and horizontal thin dashed lines) have been calculated by solving Equations (4.23) and (4.24) simultaneously.

Therefore, the pitchfork bifurcation occurring in the symmetrical case is essentially replaced in the non-symmetrical case by a stable state (lower curve) alongside with a saddle-node bifurcation (upper curve). As we increase the density contrast there is no longer a sharp transition at the bifurcation point representative of the symmetric case (compare with Figure 4.3). Hence, the equilibrium position of the thread varies smoothly with the density contrast on the lower stable curve. Furthermore, the stable branch of the upper curve, which is also a permitted equilibrium state of the system, is not accessible unless the thread

is given a large initial disturbance making this equilibrium more favourable. Qualitatively similar results are obtained for the bifurcation diagrams as a function of the thread length and the total length, see Figure 4.5 middle and bottom panels, respectively. As was expected, when s_0/L tends to 0.5, the diagrams tend to those in Figure 4.3, characterised by an stable solution at $s_e/L = 0.5$ below the bifurcation values (see lower purple solid line in the top and middle panels), however, we see that the two curves (upper and lower) still remain disconnected for $s_0/L = 0.49$.

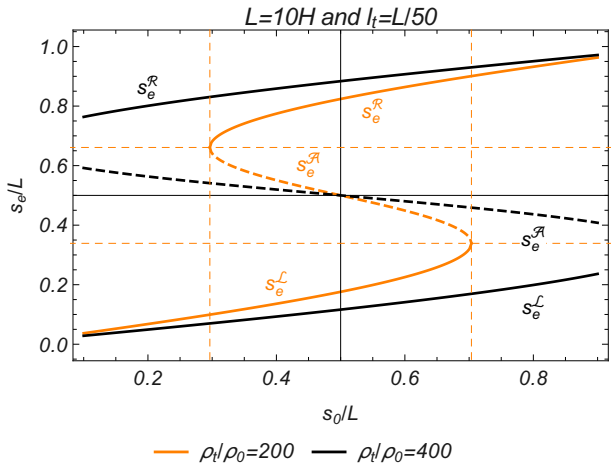

Figure 4.6: Solutions s_e of Equation (4.23) as a function of s_0/L for $\rho_t/\rho_0 = 200$ (orange lines) and $\rho_t/\rho_0 = 400$ (black lines). $L = 10\,H$ and $l_t = L/50$. The curves correspond to $s_e^{\mathscr{L}}$ and $s_e^{\mathscr{R}}$ (solid lines), and $s_e^{\mathscr{A}}$ (dashed line). The bifurcation points around $s_0/L = 0.3$ and $s_0/L = 0.7$ (intersections between vertical and horizontal orange dashed lines) have been calculated by solving Equations (4.23) and (4.24) simultaneously.

Figure 4.6 shows the situation when there is a transition between one to three solutions (orange lines, $\rho_t/\rho_0 = 200$) when the initial position of the thread, s_0, is changed. One of the emerging solutions around $s_0/L = 0.3$, $s_e^{\mathscr{A}}$, is unstable, while the other solution, $s_e^{\mathscr{R}}$, is stable. This behaviour is similar to that found for the symmetric case with $s_0 = L/2$ described earlier. In Figure 4.6 a case with no bifurcations but with multiple solutions for fixed parameter values (black lines, $\rho_t/\rho_0 = 400$) is also represented. The solutions that are around the apex (dashed curves) have a different behaviour with respect to the left and right part solutions. In this case $s_e^{\mathscr{A}}$ decreases when s_0 is raised, while for the other two solutions $s_e^{\mathscr{L}}$ and $s_e^{\mathscr{R}}$ increase with s_0. When s_0 tends to the tube apex, $s_e^{\mathscr{A}}$ tends precisely to $s_e = L/2$ and this solution is unstable. In conclusion, given that the initial thread position, s_0, is not at the apex, this parameter breaks the symmetry of the system. In bifurcation theory it is called an imperfection parameter. The resulting bifurcation diagram of Figure 4.6 is no longer symmetric about a horizontal line and possesses an S-shape, see Wang (1994) and Section 3.6 of Strogatz (2018). The orange curve in this figure has a lower and an upper bifurcation point, $s_{0,l}/L \simeq 0.3$ and $s_{0,u}/L \simeq 0.7$, respectively. This S-shaped bifurcation curve can be thought of as the composition of two saddle-node bifurcation curves (these sort of bifurcations will appear in Chapter 5), the lower (upper) one with its bifurcation point at $s_0 = s_{0,l}$ ($s_0 = s_{0,u}$). The black curve of Figure 4.6 is a special case of S-shaped bifurcation curve because the lower and upper bifurcation points are outside the range of validity of the

parameter s_0. Therefore, the system always supports three solutions.

4.4 Linear stability analysis

We have intuitively described the nature of stable and unstable solutions in the previous section that has been complemented with known results from bifurcation theory in mathematics. In the present section we provide a precise stability analysis based on linear theory but using physical grounds. We derive an expression for the oscillatory frequency of the thread, ω, as a function of the equilibrium parameters. The sign of ω^2 renders estimable knowledge about the stability properties of the configuration.

4.4.1 Thread initially at the tube apex

We start with the trivial solution at the tube apex. We consider a small longitudinal displacement, δs, of the centre of the plasma thread. We assume that $\delta s \ll L$ because we are interested in the linear regime. The restoring forces acting on the plasma thread are the pressure gradient and the projected gravity force. Let us write the pressure at both sides of the thread as a function of the displacement with respect to $L/2$, the equilibrium position. Using again the adiabatic assumption, the pressure on the left and right parts of the tube is

$$\begin{aligned} p_1(\delta s) &= p_0 \left(\frac{L/2 - l_t/2}{L/2 - l_t/2 + \delta s} \right)^{\gamma}, \\ p_2(\delta s) &= p_0 \left(\frac{L/2 - l_t/2}{L/2 - l_t/2 - \delta s} \right)^{\gamma}. \end{aligned} \tag{4.25}$$

The terms in parenthesis are

$$\begin{aligned} \left(\frac{L/2 - l_t/2}{L/2 - l_t/2 \pm \delta s} \right)^{\gamma} = \left(\frac{1}{1 \pm 2\delta s/(L - l_t)} \right)^{\gamma} &= (1 \pm 2\delta s/(L - l_t))^{-\gamma} \\ &\simeq 1 \mp 2\gamma \delta s/(L - l_t), \end{aligned} \tag{4.26}$$

where in the last step we have used the Maclaurin series approximation for small arguments (because $\delta s/L \ll 1$). This approximation is crucial to find the linear result we are looking for, since pressure fluctuations are now linearly proportional to δs. We have that

$$\begin{aligned} p_1(\delta s) &\simeq p_0 \left[1 - 2\gamma \, \delta s/(L - l_t) \right], \\ p_2(\delta s) &\simeq p_0 \left[1 + 2\gamma \, \delta s/(L - l_t) \right], \end{aligned} \tag{4.27}$$

and the pressure gradient is

$$\frac{dp}{ds}(\delta s) \simeq \frac{\Delta p}{\Delta s}(\delta s) = \frac{p_2 - p_1}{l_t} = \frac{4 \, p_0 \, \gamma \, \delta s}{l_t \, (L - l_t)}. \tag{4.28}$$

For the projected gravity around $s = L/2$ it is not difficult to see that Equation (4.1) reduces to a sinus of δs,

$$g_{\parallel}(L/2 + \delta s) = g \, \sin\left(\pi \frac{\delta s}{L} \right) \simeq g \frac{\pi}{L} \delta s, \tag{4.29}$$

where we have used again the approximation for small arguments in the last step.

We have expressions for all the terms that appear in the momentum equation, i.e. Equation (4.6) for $s = L/2 + \delta s$, which is now

$$\rho_{\mathrm{t}} \frac{d^2 \delta s}{dt^2} = -\frac{4\, p_0\, \gamma}{l_{\mathrm{t}}\,(L - l_{\mathrm{t}})} \delta s + \rho_{\mathrm{t}}\, g\, \frac{\pi}{L} \delta s = \delta s \left[-\frac{4\, p_0\, \gamma}{l_{\mathrm{t}}(L - l_{\mathrm{t}})} + \rho_{\mathrm{t}}\, g\, \frac{\pi}{L} \right]. \tag{4.30}$$

The right-hand side term of this equation is proportional to δs only. The solution to the differential equation is of the form $\exp(i\omega t)$ and we have that

$$\omega^2 = \frac{4\, c_{\mathrm{s0}}^2}{l_{\mathrm{t}}\,(L - l_{\mathrm{t}})\rho_{\mathrm{t}}/\rho_0} - g\, \frac{\pi}{L}, \tag{4.31}$$

where the sound speed of the background has been used. According to Equation (4.31) we realise that we can have the following situations: $\omega^2 > 0$ (ω real) meaning that the motion is purely oscillatory around a stable equilibrium, $\omega^2 < 0$ (ω purely imaginary) indicating that the system is unstable, and $\omega^2 = 0$. This is the expected situation based on the results of Section 4.3 about the equilibrium. Interestingly, it is not difficult to see that growth rates and frequencies derived from the dispersion relation in Equation (4.31) are exactly the same τ and ω found in Section 4.3.1 and derived from the mathematical point of view.

The transition between the two regimes ($\omega^2 = 0$) provides helpful information because it corresponds to a bifurcation point, where, as we have seen, the number of solutions and/or their stability can change. This transition takes place when the following condition for the density contrast is satisfied,

$$\rho_{\mathrm{tb}}/\rho_0 = \frac{4\, c_{\mathrm{s0}}^2\, L}{g\pi\, l_{\mathrm{t}}\,(L - l_{\mathrm{t}})}, \tag{4.32}$$

density contrasts below this bifurcation value correspond to a stable solution, whereas for $\rho_{\mathrm{t}} > \rho_{\mathrm{tb}}$ the stable solution turns unstable. This behaviour is shown in Figure 4.7 (top panel) where ω^2 is plotted as a function of ρ_{t}/ρ_0 for different values of L and for the three possible equilibrium positions $s_{\mathrm{e}}^{\mathscr{A}}$, $s_{\mathrm{e}}^{\mathscr{L}}$, and $s_{\mathrm{e}}^{\mathscr{R}}$. Since the initial position of the thread is at the apex of the structure, $s_{\mathrm{e}}^{\mathscr{L}}$ and $s_{\mathrm{e}}^{\mathscr{R}}$ are symmetric and have the same frequency, so only one solid curve with $\omega^2 > 0$ is visible to the right of the bifurcation point. Frequencies associated to $s_{\mathrm{e}}^{\mathscr{A}}$ are found at the left of the bifurcation point and below zero in Figure 4.7. We see that the bifurcation density, that delimits stable solutions (solid curves) with unstable (dashed curves), does not strongly depend on L. This behaviour agrees with Equation (4.32) that simplifies to $\rho_{\mathrm{tb}}/\rho_0 = \frac{4\, c_{\mathrm{s0}}^2}{g\pi\, l_{\mathrm{t}}}$ when l_{t} is neglected with respect to L.

Assuming that ρ_{t}/ρ_0 and L are fixed then we have a bifurcation length for the thread that determines if the solution is stable or unstable,

$$l_{\mathrm{tb}} = \frac{L}{2} \left(1 - \sqrt{1 - \frac{16\, c_{\mathrm{s0}}^2}{g\pi\, L \rho_{\mathrm{t}}/\rho_0}} \right), \tag{4.33}$$

(see middle panel of Figure 4.7). For typical prominence values the term inside the square root is always positive and the square root of this term is smaller than one, providing a

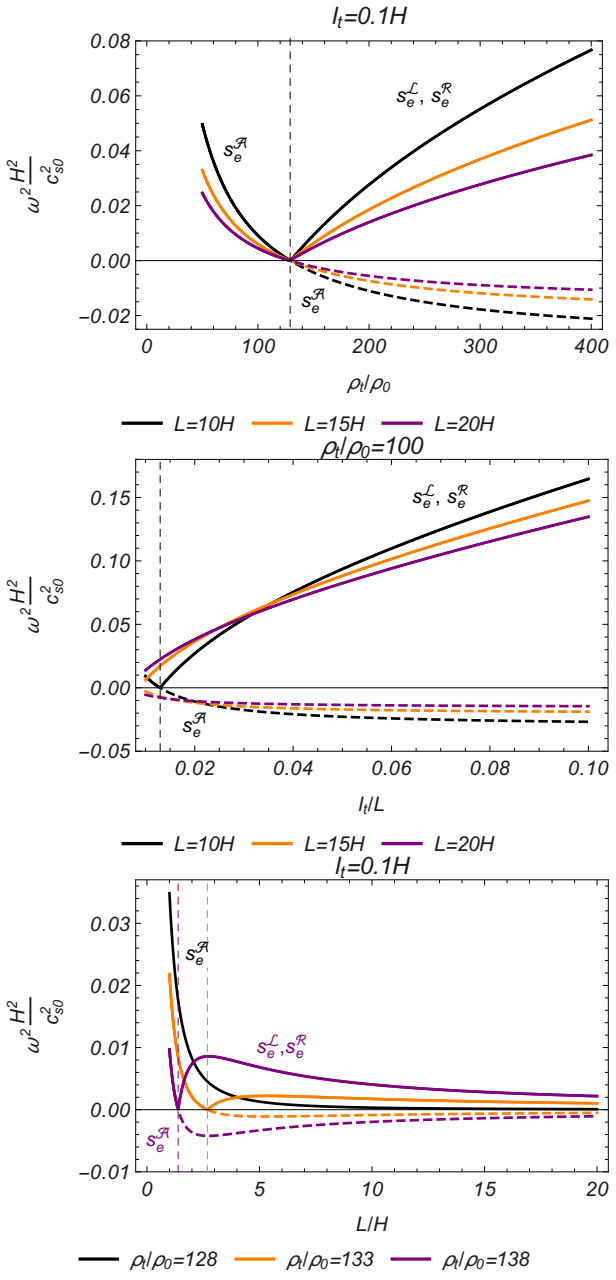

Figure 4.7: ω^2 as a function of ρ_t/ρ_0 (top panel), l_t/L (middle panel), and L/H (bottom panel) for $s_e = s_e^{\mathcal{A}}$ (below bifurcation points and lower branch curves, Equation (4.31)) and $s_e = s_e^{\mathcal{L}} = s_e^{\mathcal{R}}$ (upper branch curves, Equation (4.40)). In these plots $s_0 = L/2$. The bifurcation values (thin dashed vertical lines) have been calculated using the analytical expressions given by Equations (4.32), (4.33), and (4.34).

physically acceptable value ($l_{tb} > 0$). The equilibrium positions of threads with lengths shorter than l_{tb} are always stable.

Finally, from Equation (4.31) we find that the bifurcation length of the magnetic field lines

is

$$L_{\rm b} = \frac{l_{\rm t}}{1 - \frac{4\,c_{\rm s0}^2}{g\pi\,l_{\rm t}\,\rho_{\rm t}/\rho_0}}, \tag{4.34}$$

and the term in the denominator is not necessarily positive. A negative bifurcation length is non-physical, meaning that in this situation it is not possible to find a transition from the stable to the unstable regime. Therefore, when

$$\frac{4\,c_{\rm s0}^2}{g\pi\,l_{\rm t}\,\rho_{\rm t}/\rho_0} > 1, \tag{4.35}$$

the bifurcation length is negative implying in our case that the solution is always stable ($\omega^2 > 0$) independently of the length L (this is easy to check introducing the condition given by Equation (4.35) into Equation (4.31)). Figure 4.7 (bottom panel) shows ω^2 as a function of L for different values of $\rho_{\rm t}$ and we find a case where Equation (4.35) is satisfied (black solid curve) and ω^2 is always positive. For values of the parameters that make the left-hand side of Equation (4.35) less than one, the solution is either stable or unstable depending on the length of the field lines, if $L < L_{\rm b}$ the system, that only develops $s_{\rm e}^{\mathscr{A}}$, is stable, and if $L > L_{\rm b}$ it is unstable (see lower branch curves in bottom panel of Figure 4.7). Interestingly, the bifurcation length $L_{\rm b}$ depends strongly on the density contrast (see the short range of $\rho_{\rm t}/\rho_0$ in Figure 4.7 bottom panel). Note that to have a stable solution the three criteria ($\rho_{\rm t} < \rho_{\rm tb}$, $l_{\rm t} < l_{\rm tb}$, and $L < L_{\rm b}$ or equivalently Equation (4.35) for the length of the field lines) must be simultaneously satisfied. This is an interesting result that provides useful information about the behaviour of the system depending on the parameters.

It is worthly to note that the first term on the right-hand side of Equation (4.31) is the frequency squared of a slow mode in a slab model of length $l_{\rm t}$ inside a field line with a length of L (Joarder & Roberts 1992b; Díaz et al. 2010; Soler et al. 2010). Interestingly, Luna et al. (2012a) derived a similar expression for the frequency but for a magnetic field with a dip at the location of the thread. In their formula the sign in front of the gravitational term is positive and therefore the instability is not present in their configuration, their system is always (linearly) stable because they consider a concave upwards geometry for the magnetic field.

Now we generalise the frequency of oscillation for any equilibrium position, $s_{\rm e}$, along the tube and hence we do not restrict to the equilibrium solution at the tube apex. But note that the thread is still initially located at $s = L/2$. Under these conditions we have that

$$\begin{aligned} p_1(\delta s) &= p_{10}\left(\frac{s_{\rm e} - l_{\rm t}/2}{s_{\rm e} - l_{\rm t}/2 + \delta s}\right)^{\gamma}, \\ p_2(\delta s) &= p_{20}\left(\frac{s_{\rm e} - l_{\rm t}/2}{L - s_{\rm e} - l_{\rm t}/2 - \delta s}\right)^{\gamma}, \end{aligned} \tag{4.36}$$

where p_{10} and p_{20} correspond to the equilibrium pressures that satisfy Equation (4.15). We rewrite p_1 as

$$p_1(\delta s) \simeq p_{10}\left[1 - \gamma\delta s/(s_{\rm e} - l_{\rm t}/2)\right], \tag{4.37}$$

where we have used the Maclaurin series approximation for small arguments but note that if s_e is similar to $l_t/2$ the approximation is not valid. An analogous expression is derived for p_2. The pressure gradient using the previous equations is approximated by

$$\frac{dp}{ds}(\delta s) \simeq \frac{p_2(\delta s) - p_1(\delta s)}{l_t} = \frac{1}{l_t}\left(p_{20} - p_{10} + \frac{p_{20}\,\gamma\,\delta s}{L - s_e - l_t/2} + \frac{p_{10}\,\gamma\,\delta s}{s_e - l_t/2}\right). \tag{4.38}$$

For the projected gravity we need to perform a Taylor expansion of the cosine around the equilibrium position which is now s_e,

$$\cos\left(\pi\frac{s}{L}\right) = \cos\left(\pi\frac{s_e}{L}\right) - \frac{\pi}{L}\sin\left(\pi\frac{s_e}{L}\right)(s - s_e) + ..., \tag{4.39}$$

where we only retain up to linear terms in $s - s_e$. We have that $\delta s = s - s_e$ according to our notation.

In the momentum equation, using Equations (4.38) and (4.39), we find two terms that are not proportional to δs but that cancel because they correspond to the equilibrium condition given by Equation (4.19). After some algebra it is not difficult to derive that the square of the frequency is

$$\omega^2 = \frac{c_{s0}^2}{l_t\rho_t/\rho_0}\left[\frac{(L/2 - l_t/2)^\gamma}{(L - s_e - l_t/2)^{\gamma+1}} + \frac{(L/2 - l_t/2)^\gamma}{(s_e - l_t/2)^{\gamma+1}}\right] - g\,\frac{\pi}{L}\sin\left(\pi\frac{s_e}{L}\right). \tag{4.40}$$

When $s_e = L/2$, i.e., the trivial solution, Equation (4.40) is exactly the same as Equation (4.31), recovering the previous situation. The solutions of Equation (4.40) are shown in Figure 4.7. Below the bifurcation values ρ_{tb}, l_{tb}, and L_b, the equilibrium solution is $s_e^{\mathscr{A}}$. When the bifurcation values are reached, $s_e^{\mathscr{A}}$ becomes unstable ($\omega^2 < 0$), and as expected, $s_e^{\mathscr{L}}$ is stable ($\omega^2 > 0$). For $s_e^{\mathscr{R}}$ the value of frequency is exactly the same as that for $s_e^{\mathscr{L}}$ and therefore only one curve is visible in the plot. It is interesting to mention that for $s_e^{\mathscr{L}}$ and $s_e^{\mathscr{R}}$ (upper branch curves) the frequency squared monotonically increases with ρ_t and l_t, but it increases with L until a maximum and then it starts decreasing with L. It is important to mention that all the results shown in Figure 4.7 are the solutions of the configurations shown in Figure 4.3 and the stability analysis done in Section 4.3.1 agrees with the results in the present section.

4.4.2 Thread initially at any location along the tube

Finally, using the same procedure as before we derive an expression for the oscillation frequency of a thread around the final equilibrium position s_e, that has been achieved from an initial location of the thread at $s_0 \neq L/2$. The corresponding pressures at the edge of the thread due to a small displacement δs from the equilibrium position are expressed as Equation (4.36), but now p_{10} and p_{20} correspond to the equilibrium pressures that satisfy Equation (4.22). Using similar approximations to those in Equation (4.37) and cancelling the equilibrium terms according to Equation (4.23), we eventually find that the frequency squared is

$$\omega^2 = \frac{c_{s0}^2}{l_t\rho_t/\rho_0}\left[\frac{(L - s_0 - l_t/2)^\gamma}{(L - s_e - l_t/2)^{\gamma+1}} + \frac{(s_0 - l_t/2)^\gamma}{(s_e - l_t/2)^{\gamma+1}}\right] - g\,\frac{\pi}{L}\sin\left(\pi\frac{s_e}{L}\right). \tag{4.41}$$

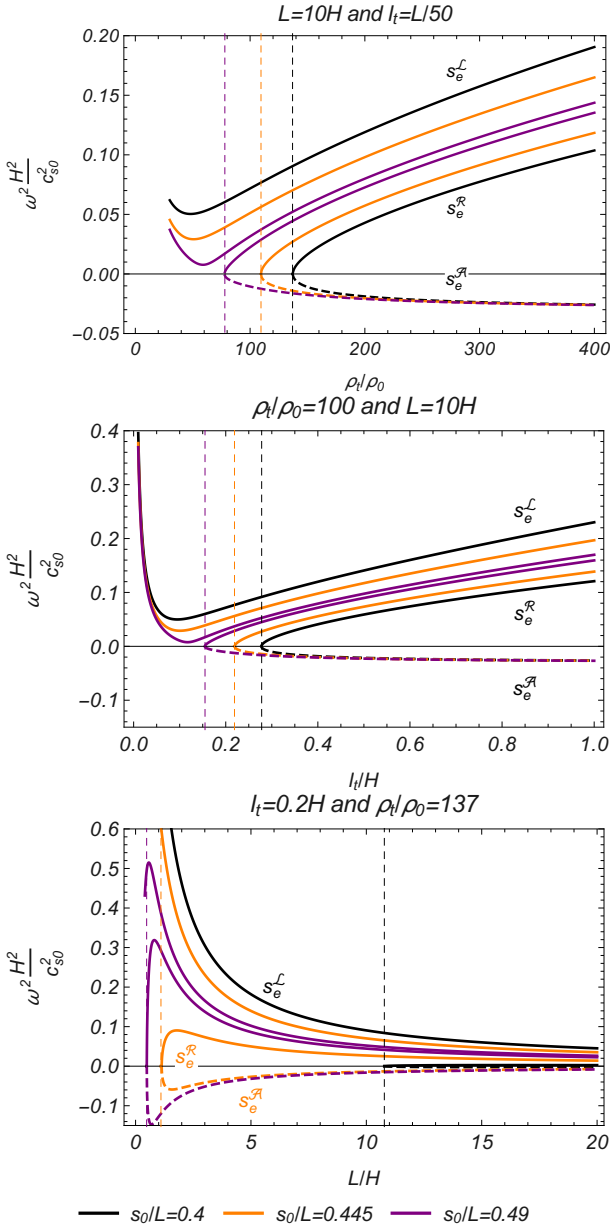

Figure 4.8: ω^2 as function of different equilibrium parameters (Equation (4.41)) for three initial positions of the thread, when its initial position is not at the magnetic tube apex. The vertical lines correspond to the bifurcation points and are calculated imposing that $\omega^2 = 0$.

The previous frequency expressions given in Equation (4.31) when $s_0 = s_e = L/2$ and Equation (4.40) when $s_0 = L/2$, $s_e \neq L/2$ are recovered in Equation (4.41). In this equation s_e must be a solution to Equation (4.23). Obtaining analytical bifurcation values, except for the trivial case ($s_0 = s_e = L/2$), is much more difficult now and it is only possible for the bifurcation density contrast. The rest of bifurcation values are determined numerically. As expected from bifurcation theory, imposing the condition for a bifurcation value, i.e., $\omega^2 = 0$ in Equation (4.41), is completely equivalent to the condition given by Equation (4.24) that determines the bifurcation point based only on the equilibrium configuration. This is confirmed by the comparison of the bifurcation values in Figure 4.8 and the respective results

in Figure 4.5. This is also a solid indication that the performed eigenfrequency analysis in this section is coherent.

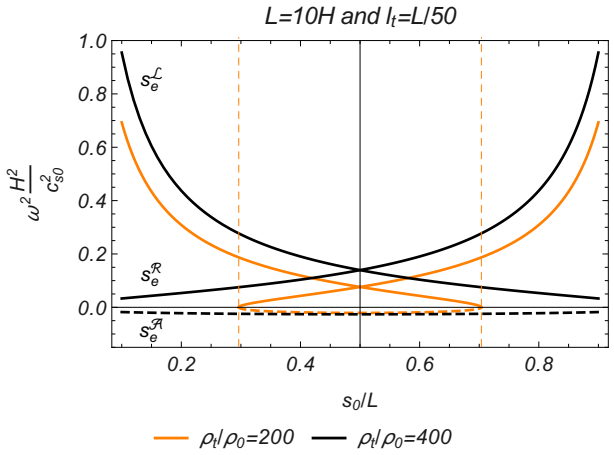

Figure 4.9: ω^2 as a function of s_0/L (Equation (4.41)) for the three solutions obtained in Figure 4.6. The solid lines correspond to $s_{\mathrm{e}}^{\mathscr{L}}$ (lines decreasing from left to right) and $s_{\mathrm{e}}^{\mathscr{R}}$ (lines increasing from left to right), and the dashed lines to $s_{\mathrm{e}}^{\mathscr{A}}$. The horizontal line represents $\omega = 0$ and divides the plot into stable and unstable solutions. In this plot the left and right solutions are stable while the near apex solution is unstable. The bifurcation points (vertical dashed lines) have been calculated by solving Equations (4.23) and (4.24) simultaneously, and it is equivalent to impose $\omega^2 = 0$ in Equation (4.41) once s_{e} is known.

Now, the break of symmetry due to the imperfection parameter s_0 causes the difference between the frequency squared of $s_{\mathrm{e}}^{\mathscr{L}}$ and $s_{\mathrm{e}}^{\mathscr{R}}$. This is visible in the plotted upper curves of Figure 4.8 (solid curves). Beyond the bifurcation values two branches corresponding to $s_{\mathrm{e}}^{\mathscr{R}}$ and $s_{\mathrm{e}}^{\mathscr{A}}$ appear, being positive for $s_{\mathrm{e}}^{\mathscr{R}}$ (solid curves) and negative for $s_{\mathrm{e}}^{\mathscr{A}}$ (dashed curves). Logically, when s_0/L tends to 0.5 (purple curves), ω^2 for $s_{\mathrm{e}}^{\mathscr{R}}$ tends to the same value as for $s_{\mathrm{e}}^{\mathscr{L}}$. For $s_{\mathrm{e}}^{\mathscr{R}}$ (emerging at the bifurcation point), ω^2 increases with ρ_{t}/ρ_0 (top panel) and l_{t}/H (middle panel). For $s_{\mathrm{e}}^{\mathscr{L}}$, stable in the whole parameter range, ω^2 decreases with ρ_{t}/ρ_0 and l_{t}/H until it reaches a minimum located before the bifurcation point from where it starts increasing. On the contrary, in the bottom panel of Figure 4.8 we see that for $s_{\mathrm{e}}^{\mathscr{L}}$ the frequency decreases for large values of L.

In Figure 4.9 the three square of the frequencies corresponding to the solutions in Figure 4.6 are plotted as a function of the initial position of the thread, s_0. To calculate these frequencies the values of s_{e} that satisfy Equation (4.23) have been used. It is interesting to see that $s_{\mathrm{e}}^{\mathscr{L}}$ and $s_{\mathrm{e}}^{\mathscr{R}}$ are always stable while $s_{\mathrm{e}}^{\mathscr{A}}$ is always unstable. As expected from physical grounds the left and right side solutions converge to the same value when there is symmetry in the system, i.e., for $s_0 = L/2$ (note that beyond this point the meaning of $s_{\mathrm{e}}^{\mathscr{L}}$ and $s_{\mathrm{e}}^{\mathscr{R}}$ has to be inverted). We also observe the transition between one and three solutions for a specific choice of parameters ($\rho_{\mathrm{t}}/\rho_0 = 200$, orange curves). At the bifurcation point two solutions emerge from $\omega = 0$, one representing a stable solution ($s_{\mathrm{e}}^{\mathscr{R}}$) and another one corresponding to an unstable solution ($s_{\mathrm{e}}^{\mathscr{A}}$). We also see that ω^2 significantly varies with s_0/L for stable solutions but it is essentially independent of s_0/L for unstable solutions.

4.5 Conclusions and discussion

The thread-like structures studied in this work appear to be present in filaments everywhere (Lin et al. 2008), along the horizontal spines or the quasi-vertical barbs. High-resolution observations of the solar corona show that the fine structure of prominences is very dynamic. Even during the prominence formation we observe plasma flows along the magnetic fields. The localised heating above the flux tube footpoints produces a cyclic pattern of evaporation of the chromospheric plasma, which condenses in the coronal part of the tube and produces the plasma flows. During the process, the pressure imbalance between the chromosphere and the condensation region would push upwards the chromospheric plasma to supply mass to the corona in the form of siphon flows (Xia et al. 2011; Zhou et al. 2014) In spite of the complicated dynamics of prominence threads, it is interesting to perform the stability analysis of these structures. For this reason, we have developed a very idealised model that provides the basic physics to understand the evolution of a density enhancement or thread that moves along a curved concave magnetic field, a very common situation in the solar corona. The main assumption in the model is that the behaviour of the thread is essentially that of a piston that in our case is governed by gas pressure and gravity. Our model allows the existence of a suspended mass in the absence of magnetic dips.

We have derived two equations for the equilibrium of a thread initially located at any position along the tube (Equation (4.23)) and the corresponding eigenfrequency of oscillation (Equation (4.41)) that have revealed useful knowledge about the stability properties of the system. In spite of the simplicity of our model the equilibrium equation is quite rich from the mathematical point of view and leads to significant physical interpretations. Different scenarios are possible, a density enhancement initially located at the apex is always in equilibrium in our model but this equilibrium is either stable or unstable. We have derived analytical expressions for the bifurcation values of the different parameters when a transition between a stable and unstable regime is produced. If the thread near the apex is unstable then the system allows two additional symmetric equilibria at lower heights that are stable. Under these circumstances a thread situated at the apex of the tube will move along the magnetic field until it reaches the lower state energy associated to the new equilibrium. When the density enhancement is not initially at the apex we have in essence a similar behaviour: a single stable solution or three solutions, two of them stable and the other unstable. In this last case, the mathematical behaviour of the system is characterised by the appearance of a S-shaped bifurcation, well known in bifurcation theory.

Our analysis reveals the presence of bifurcation points, obtained analytically when the thread is initially located at the apex. For example, when the condition given by Equation (4.35) is satisfied, the system is stable, independently of the length of the magnetic field lines where the thread is suspended. Otherwise, a thread with a fixed density contrast and length, can be stable when it is located along short magnetic field lines but unstable on long magnetic field lines, i.e., higher up in the magnetic arcade. This can have some implications regarding the finite height of observed solar prominences but also concerning the stability of unbounded models with height like those of Hood & Anzer (1990). However, the presence of magnetic dips, missing in our model, can have important consequences regarding stability.

The length of the magnetic tubes plays a key role in the equilibrium and stability of the

threads. The physical interpretation of the dependence of the instability on the length of the field lines can be connected with the travel time of sound waves (pressure restoring timescale) from the thread to the footpoints and the return time due to the reflection produced by the line-tying condition. A small lateral displacement of the thread induces a pressure wave whose total travel time depends on the length of the magnetic field line. On short magnetic field lines the pressure will be adjusted quickly, while for long field lines it is possible that the regulation of the pressure is not fast enough to maintain the thread around its initial equilibrium state before it has reached a high enough velocity that sends it to another equilibrium position.

A natural extension of the model presented here is the inclusion of magnetic dips through the straight forward modification of the projected gravity along the field. This will have most likely relevant consequences regarding stability and will affect the eventual bifurcation points that may appear in the system. This work is addressed in Chapter 5 as a continuation of the present chapter. Another future improvement to the model is the implementation of the variation of the cross-sectional area along the tube, allowing to incorporate a truly 3D effect in the calculation of the equilibrium and the corresponding eigenfrequencies (see Luna et al. 2016a).

An et al. (1988); Wu et al. (1990) investigated the effects of plasma injection on the formation of Kippenhahn-Schlüter model of prominence in optimum conditions. They found that for high values of the plasma-β parameter (the ratio of plasma pressure to magnetic pressure) the magnetic arcade develops a magnetic dip at the centre of the structure that supports the prominence plasma. However, comparing with our study, in the low plasma-β regime (or under others injection conditions) they found that the dip is less deep and the system develops two additional plasma enhancements located at the lateral edges of the magnetic arcade. It is interesting to mention that in recent works, it is suggested that the deformation of the magnetic field lines is determined by the parameter δ (the ratio of the gravity to the magnetic pressure) (Zhou et al. 2018; Zhang et al. 2019). An et al. (1988) suggested that the steady lateral plasma accumulates because of both the injection process and because the field lines do not geometrically contain the injected plasma, but Wu et al. (1990) proposed that the prominence mass is also supported by an increase in the pressure gradient. Since in this study we consider that magnetic field lines do not change due to the presence of the dense thread we will investigate in detail the results of An et al. (1988); Wu et al. (1990) in the next chapter. On the contrary, Zhang et al. (2013) investigated the formation of one-dimensional filament threads by chromospheric heating in the presence of non-adiabatic effects, i.e., radiative losses and thermal conduction. They obtained that for magnetic loops without a dip, the plasma condenses but it streams along the magnetic field and disappears after falling to the footpoints (Antiochos et al. 2000; Karpen et al. 2006). Moreover, when the thread is initially in a thermal and force-balance equilibrium state but it is disturbed by a strong velocity perturbation, the prominence mass drains down to the chromosphere. Dense blobs of falling plasma have been habitually observed (Schrijver 2001; de Groof et al. 2005) so that it seems that threads cannot be held static along vertical magnetic flux tubes in the corona. The coronal part of the tube can only slow down the falling blobs. Müller et al. (2004) proposed that the acceleration reduces because the pressure of the cooling plasma underneath the radiating blobs slows down the descent, and Oliver et al. (2014, 2016) and Martínez-Gómez et al. (2020) argued that pressure gradient is the main force

that opposes the action of gravity. Our study proposes that the pressure gradient can cause the equilibrium of threads in quasi-vertical flux tubes without dips even though it has not been corroborated by observations. Regardless, our model is relatively simple to study the observed down-flows, and other mechanisms such as radiation and heat conduction must be considered.

Our model also demonstrates that when the mass of the thread is high enough the position of the equilibrium is near the footpoints. This allows us to constrain the parameters to find solutions that do not represent suspended threads but correspond to threads that travel down the tube until they essentially settle down into a new equilibrium around the base of the corona. This last situation is applicable, for example, to coronal rain falling along magnetic field lines. In this regard, our study can be relevant to explain some results of 2D and 2.5D numerical simulations of dense blobs released in the solar atmosphere (e.g. Mackay & Galsgaard 2001; Kohutova & Verwichte 2017a,b). These simulations have in common with our work a dense blob (akin to our thread) that is released in a gravitationally stratified background atmosphere with a closed bottom boundary at the base of the corona. This setup allows the dense material falling along the magnetic tube to act as a piston. For this reason, Mackay & Galsgaard (2001) and Kohutova & Verwichte (2017a,b) find, as we do, that when the blob density is large enough this cold material falls down to the surface because the increased pressure that builds underneath it cannot counteract the blob weight. On the contrary, blobs with smaller mass can find an equilibrium position before reaching the surface and so they oscillate around this position. In addition to the relevance of the blob density, ρ_t, we have also noted that the length of magnetic field lines and the blob length are important parameters that control the system dynamics.

Chapter 5

Curved magnetic fields with dips [3]

5.1 Introduction

In Chapter 4 we have investigated the gravitational instability of a curved magnetic field without dips. We have found that the line-tying effect at the photosphere produces a pressure increment along the magnetic field lines that sustains the prominence mass at different equilibrium points, even in the absence of magnetic dips. The instability of the system was analysed by both linear stability analysis and bifurcation theory. A parametric survey was carried out to understand the occurrence of stable/unstable regimes.

Most of the magnetic models of prominences consider that plasma is hosted by a magnetic dip (e.g., Hillier & van Ballegooijen 2013). For this reason, in this final chapter of the Thesis, we extend the findings of Chapter 4 by introducing a magnetic dip into the curved flux tube model. Moreover, we apply a different approach in the gravity term to derive an equilibrium equation based on the average gravity on the thread which is more realistic. Finally, we study the equilibrium and stability of this new thread model with a dip that is shifted with respect to the apex of the structure.

5.2 Model and equations

5.2.1 Basic model

We model the magnetic flux tube as three curved segments: two lateral concave downwards circles with a radius of $R_{\rm L} < 0$ and arc lengths of $s_1 = s_2 = L/2 - l_{\rm d}/2$, and a curved dip with a radius of $R_{\rm d} = R_{\rm d}(s)$ and length $l_{\rm d}$ (see top panel of Figure 5.1). In this model s is the coordinate along the tube, starting from the left foot, while L is the total length of the magnetic tube. We start with the description of a magnetic structure that is symmetric around the midpoint located at $s = L/2$. For a symmetric tube the bottom of the dip coincides with the midpoint. We assume that the cross-section of the tube is constant. The shape of the structure is determined by the definition of the projected gravity along the

[3] This chapter is based on: Adrover-González, A., Terradas, J., Oliver, R., Carbonell, M.; *Gravitational instability of solar prominence threads: II. Curved magnetic fields with dips*, in preparation.

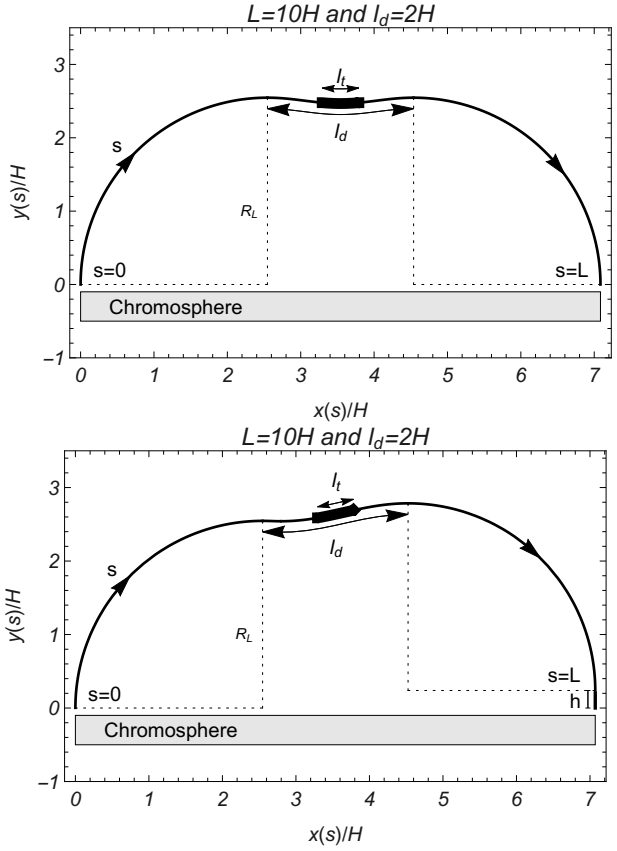

Figure 5.1: Top panel: Sketch of the magnetic structure and the prominence thread for a total tube length $L = 10\,H$ and a dip length $l_{\rm d} = 2\,H$. The thread length is $l_{\rm t} = 0.5\,H$. The radius of the two lateral circles is $R_{\rm L} = -(L - l_{\rm d})/\pi$. s is the coordinate along the tube, starting from the left foot. Spatial dimensions are scaled to $H = 10\,{\rm Mm}$. Bottom panel: Same as top panel but for a non-symmetric dip. We include a vertical leg of length h at the right foot.

magnetic field line, expressed as follows:

$$g_{\parallel}(s) = \begin{cases} -g\,\cos\left(\pi\frac{s}{L-l_{\rm d}}\right) & 0 < s < s_1, \\ \frac{g\,l_{\rm d}}{2\,(L-l_{\rm d})}\sin\left(2\pi\,\frac{s-s_1}{l_{\rm d}}\right) & s_1 < s < s_1 + l_{\rm d}, \\ g\sin\left(\pi\,\frac{s-s_1-l_{\rm d}}{L-l_{\rm d}}\right) & s_1 + l_{\rm d} < s < L, \end{cases} \tag{5.1}$$

with $g = 0.274\,{\rm km\,s^{-2}}$ being the gravity acceleration. The expression of the gravity is defined to have its derivative continuous at the borders of the dip, $s = L/2 \pm l_{\rm d}/2$, i.e.,

$$g'_{\parallel}(s) = \begin{cases} \frac{g\,\pi}{L-l_{\rm d}}\sin\left(\pi\frac{s}{L-l_{\rm d}}\right) & 0 < s < s_1, \\ \frac{g\,\pi}{L-l_{\rm d}}\cos\left(2\pi\,\frac{s-s_1}{l_{\rm d}}\right) & s_1 < s < s_1 + l_{\rm d}, \\ \frac{g\,\pi}{L-l_{\rm d}}\cos\left(\pi\,\frac{s-s_1-l_{\rm d}}{L-l_{\rm d}}\right) & s_1 + l_{\rm d} < s < L. \end{cases} \tag{5.2}$$

Under this condition, the radius for the external segments of the tube is $R_{\rm L} = -\left(L - l_{\rm d}\right)/\pi$. If s is the distance along the loop from the left foot, then the lateral extension, $x(s)$, and

the height of the structure, $y(s)$, are given by

$$dx = \sin\phi \; ds \tag{5.3}$$

and

$$dy = -\cos\phi \; ds, \tag{5.4}$$

being ϕ the angle of the slope of the magnetic structure. ϕ can be expressed in terms of the projected gravity along the tube as

$$g_{\parallel}(s) = g \; \cos\phi. \tag{5.5}$$

Introducing Equation (5.5) into Equations (5.3) and (5.4), and integrating along the dip we obtain an expression for $x(s)$ and $y(s)$ in terms of the gravity profile,

$$\int_{R_{\mathrm{L}}}^{x} dx = \int_{s_1}^{s} \sqrt{1 - \left(\frac{g_{\parallel}(s)}{g}\right)^2} \, ds, \tag{5.6}$$

$$\int_{R_{\mathrm{L}}}^{y} dy = -\int_{s_1}^{s} \frac{g_{\parallel}(s)}{g} \, ds. \tag{5.7}$$

The radius of the dip as a function of s can be derived directly from $x(s)$ and $y(s)$ according to

$$R_{\mathrm{d}}(s) = \frac{\left[\left(\frac{dx}{ds}\right)^2 + \left(\frac{dy}{ds}\right)^2\right]^{3/2}}{\frac{dx}{ds}\frac{d^2y}{ds^2} - \frac{dy}{ds}\frac{d^2x}{ds^2}}. \tag{5.8}$$

We are interested in obtaining the radius of the dip at the midpoint of the structure. After some calculations we obtain that

$$R_{\mathrm{d}}(s = L/2) = \frac{L - l_{\mathrm{d}}}{\pi} = -R_{\mathrm{L}}. \tag{5.9}$$

This means that the radius of curvature at the bottom of the dip coincides with the radius of the two lateral circular segments but for opposed sign. Moreover, we can obtain an expression for a minimum tube length (L_{min}) when l_{d} is fixed, imposing that $y(s = L/2) = 0$,

$$L_{\mathrm{min}} = \left(1 + \frac{1}{\sqrt{2}}\right) l_{\mathrm{d}}. \tag{5.10}$$

On the other hand, when we set L, we obtain that the maximum dip length is

$$l_{\mathrm{dmax}} = \left(2 - \sqrt{2}\right) L. \tag{5.11}$$

The expression for the gravity is equivalent to Equation (4) of Zhang et al. (2013) when we define the depth of the dip as $D = |R_{\mathrm{L}}| - y(s = L/2) = \frac{l_{\mathrm{d}}^2}{2\pi\,(L - l_{\mathrm{d}})}$. Unlike Zhang et al. (2013), we do not have the vertical legs of their model.

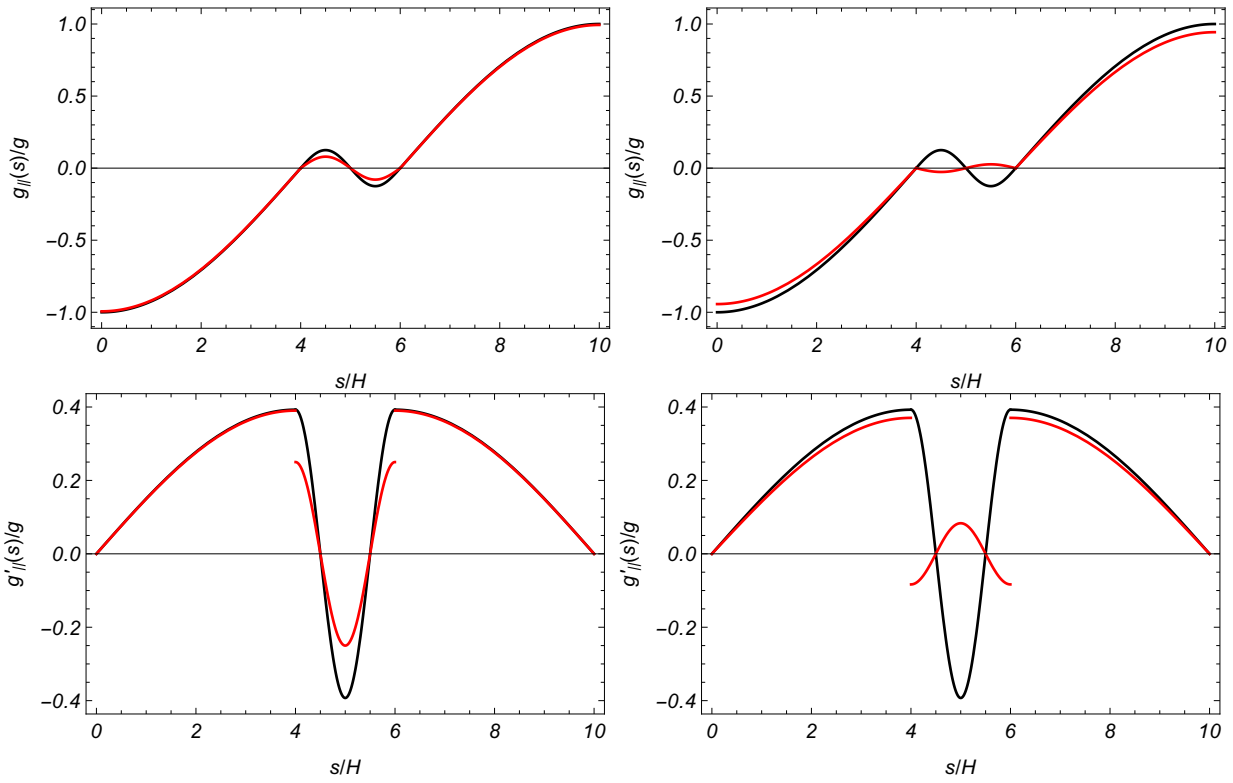

Figure 5.2: Gravity profile (top panels) and derivative of gravity profile (bottom panels) for $L = 10\,H$. $l_\mathrm{t} = 1\,H$ and $l_\mathrm{d} = 2\,H$ ($l_\mathrm{t} < l_\mathrm{d}$) in left column; $l_\mathrm{t} = 3\,H$ and $l_\mathrm{d} = 2\,H$ ($l_\mathrm{t} > l_\mathrm{d}$) in the right column. The black curves correspond to Equations (5.1) and (5.2), respectively. The red curves correspond to the average gravity (Equations (5.12) and (5.13)). Note the discontinuity in the derivative of the average gravity.

Since the thread has a finite length, gravity changes along it, and under the presence of dips it is more convenient to use the average gravity on the thread already introduced in the previous chapter,

$$\begin{aligned}\bar{g}_\parallel(s) &= \frac{1}{l_\mathrm{t}}\int_{s-l_\mathrm{t}/2}^{s+l_\mathrm{t}/2} g_\parallel(s)ds \\ &= \begin{cases} \frac{-2\,g\,(L-l_\mathrm{d})}{\pi\,l_\mathrm{t}}\cos\left(\pi\frac{s}{L-l_\mathrm{d}}\right)\sin\left(\frac{\pi}{2}\frac{l_\mathrm{t}}{L-l_\mathrm{d}}\right) & 0<s<s_1, \\ \frac{g\,l_\mathrm{d}^2}{2\pi\,l_\mathrm{t}\,(L-l_\mathrm{d})}\sin\left(2\pi\,\frac{s-s_1}{l_\mathrm{d}}\right)\sin\left(\pi\frac{l_\mathrm{t}}{l_\mathrm{d}}\right) & s_1<s<s_1+l_\mathrm{d}, \\ \frac{2\,g\,(L-l_\mathrm{d})}{\pi\,l_\mathrm{t}}\sin\left(\pi\,\frac{s-s_1-l_\mathrm{d}}{L-l_\mathrm{d}}\right)\sin\left(\frac{\pi}{2}\frac{l_\mathrm{t}}{L-l_\mathrm{d}}\right) & s_1+l_\mathrm{d}<s<L, \end{cases}\end{aligned} \tag{5.12}$$

being its derivative

$$\bar{g}'_\parallel(s) = \begin{cases} \frac{2\,g}{l_\mathrm{t}}\,\sin\left(\pi\frac{s}{L-l_\mathrm{d}}\right)\sin\left(\frac{\pi}{2}\frac{l_\mathrm{t}}{L-l_\mathrm{d}}\right) & 0<s<s_1, \\ \frac{g\,l_\mathrm{d}}{l_\mathrm{t}\,(L-l_\mathrm{d})}\,\cos\left(2\pi\,\frac{s-s_1}{l_\mathrm{d}}\right)\sin\left(\pi\frac{l_\mathrm{t}}{l_\mathrm{d}}\right) & s_1<s<s_1+l_\mathrm{d}, \\ \frac{2\,g}{l_\mathrm{t}}\,\cos\left(\pi\,\frac{s-s_1-l_\mathrm{d}}{L-l_\mathrm{d}}\right)\sin\left(\frac{\pi}{2}\frac{l_\mathrm{t}}{L-l_\mathrm{d}}\right) & s_1+l_\mathrm{d}<s<L. \end{cases} \tag{5.13}$$

l_t is the longitude of the thread. In Chapter 4 it has been shown that the differences between the average gravity and the local gravity are very small because the geometry of the field is very smooth. However, the presence of a dip in the structure enhances the differences between these two magnitudes. When $l_t \ll l_d \ll L$, Equation (5.12) reduces to Equation (5.1) and Equations (5.9) - (5.11) are valid approximations. However, when $l_t \geq l_d$, the behaviour of the structure around the dip will change significantly so that it is convenient to study the cases $l_t < l_d$ and $l_t > l_d$ separately. Figure 5.2 shows the gravity profile (top panels) and its derivative (bottom panels) for $l_t < l_d$ (left column) and $l_t > l_d$ (right column), respectively. The black curves correspond to the local gravity projected along the magnetic field line (Equations (5.1) and (5.2)) while the red curves represent the average gravity (Equations (5.12) and (5.13)). The local gravity and its derivative do not depend on the thread length so that the black curves are the same in both figures. According to their definitions, $g_\parallel(s)$ and $g'_\parallel(s)$ are continuous functions. However, when we average $g_\parallel(s)$ on the thread, we see that $\bar{g}_\parallel(s)$ remains continuous but $\bar{g}'_\parallel(s)$ develops a discontinuity at the borders of the dip. The jump grows when l_t increases. We see that at the lateral edges of the loop $g_\parallel(s)$ and $g'_\parallel(s)$ strongly match with $\bar{g}_\parallel(s)$ and $\bar{g}'_\parallel(s)$, respectively, but differ at the dip. A second important feature of the average gravity is that at the centre of the structure, when $l_t > l_d$, $\bar{g}'_\parallel(s)$ can be positive (as in the right bottom panel of Figure 5.2). This fact has important consequences regarding the gravitational stability of the equilibrium points since this change in sign can invert the stability of the system. The sign of $\bar{g}'_\parallel(s = L/2)$ oscillates depending on the sign of the term $\sin\left(\pi \frac{l_t}{l_d}\right)$ in Equation (5.13). When $l_t = n\, l_d$ $(n = 1, 2, 3 \cdots)$ the average gravity along the dip is zero.

5.2.2 Equilibrium equation

In Chapter 4 we obtained two expressions for the equilibrium equation, one for $s_0 = L/2$ representing a thread initially located at the centre of the dip, and another expression for $s_0 \neq L/2$ for a shifted thread (see Equations (4.19) and (4.23), respectively). We do not repeat the derivation here. The general expression for the equilibrium points is

$$\left(\frac{L - s_0 - l_t/2}{L - s - l_t/2}\right)^\gamma - \left(\frac{s_0 - l_t/2}{s - l_t/2}\right)^\gamma = \frac{\gamma}{c_{s0}^2}\frac{\rho_t}{\rho_0}\, l_t\, \bar{g}_\parallel(s), \tag{5.14}$$

where s_0 and ρ_t are the initial position and the density of the thread, respectively. ρ_0 and c_{s0} correspond to the density and the sound speed at the coronal part $s = L/2 - l_t/2$, and γ is the adiabatic index. Solving Equation (5.14) we obtain the equilibrium points $s = s_e$. Note that the equilibrium equation is expressed in terms of the average gravity now. As in the previous chapter we have assumed that the evolution of the thread during the motion is adiabatic and that the geometry of the loop is not modified by the presence of the dense plasma. Thus, the problem is reduced to a one dimensional model and therefore only forces along the flux tube are taken into account.

Figure 5.3 shows the left- (black curve) and right- (red curve) hand sides of Equation (5.14) as a function of s/L for $s_0/L = 0.5$, $L = 10\, H$, $\rho_t/\rho_0 = 200$, and $l_t = 0.2\, H$, when the dip length is $l_d = 2\, H$. Now we see that the system develops five possible equilibrium points (see circles) instead of the three possible solutions in the absence of a dip. As we explained in

Chapter 4, we can anticipate that the system develops bifurcation points. We remind that the bifurcation points are calculated by imposing that the spatial derivatives of the left- and right-hand sides of Equation (5.14) are equal,

$$\frac{(L - s_0 - l_t/2)^\gamma}{(L - s - l_t/2)^{\gamma+1}} + \frac{(s_0 - l_t/2)^\gamma}{(s - l_t/2)^{\gamma+1}} = \frac{l_t}{c_{s0}^2}\frac{\rho_t}{\rho_0}\,\bar{g}_\parallel'(s). \tag{5.15}$$

We know that when $s_0 = L/2$ the structure of the system is symmetric about the midpoint

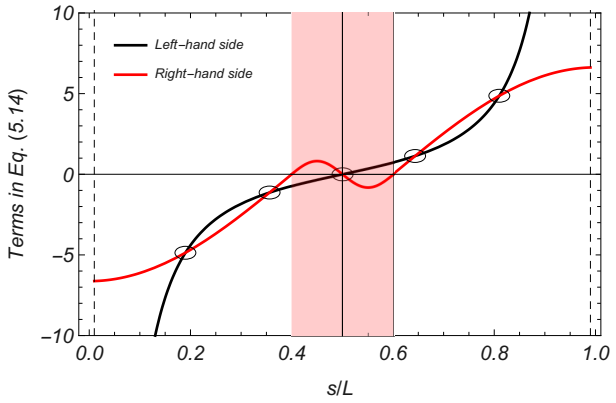

Figure 5.3: Left- (black curve) and right- (red curve) hand sides of Equation (5.14) as a function of s/L for $s_0/L = 0.5$, $L = 10\,H$, $\rho_t/\rho_0 = 200$, and $l_t = 0.2\,H$. The length of the magnetic dip is $l_d = 2\,H$. The vertical dashed lines represent the edges of the domain for the variable s, namely $s = l_t/2$ and $s = L - l_t/2$. The filled area delimits the magnetic dip.

so that the equilibrium points are also left-right symmetric. In this case we obtain that the system develops an equilibrium point at the centre of the structure, or in other words, at the bottom of the dip. Unlike Chapter 4, now we will see that this solution is always stable when $l_t < l_d$. The rest of solutions are located at the lateral sides of the flux tube, out of the dip. The four lateral fixed points are distributed in two pairs, one pair at each side of the tube. We will obtain that each pair of solutions has one stable and one unstable fixed point, with the one located at lower heights being stable. Now we imagine that we increase or decrease one of the following parameters of the structure: L, l_t, ρ_t, or l_d. The left- and right-hand side curves of Figure 5.3 slide past each other and the fixed points approach or separate each other. At some point the left-hand curve becomes tangent to the right-hand curve and the lateral equilibrium points merges in a bifurcation point, creating or destroying solutions. At this point the system only develops three solutions, the central one and the two lateral ones that vanish as soon as the bifurcation point is overtaken. When these solutions are destroyed, the system only holds the central solution up, that exists for all values of the parameters. The last parameter we can vary is the initial position of the thread s_0. The behaviour of the system changes according to the location of s_0 with respect to the dip. Thus, we can study four possible scenarios: when the initial thread position is located at the centre of the structure (Figure 5.3), when it is shifted with respect to the centre but is still inside the dip, when it is placed at the border of the dip, and finally, when it is located outside the dip. A detailed analysis of the instability of the equilibrium points as a function of the parameters of the structure is given in Sections 5.3 and 5.4.

5.2.3 Frequency equation

In Section 4.4 we performed a stability analysis based on linear theory and we derived an expression for the oscillatory frequency of the fixed points of the thread as a function of the equilibrium parameters. Specifically we obtained three formulas starting from the simplest case $s_0 = s_e = L/2$ and generalising first to $s_e \neq L/2$ and finally to $s_0 \neq L/2$ (see Equations (4.31), (4.40), and (4.41), respectively). For the general case we obtain that the square of the frequency is

$$\omega^2 = \frac{c_{s0}^2}{l_t\,\rho_t/\rho_0}\left[\frac{(L-s_0-l_t/2)^\gamma}{(L-s_e-l_t/2)^{\gamma+1}} + \frac{(s_0-l_t/2)^\gamma}{(s_e-l_t/2)^{\gamma+1}}\right] - \bar{g}'_\parallel(s=s_e), \tag{5.16}$$

expressed in terms of the average gravity now. It is not difficult to see that for $l_t \ll l_d$ and $s_0 = s_e = L/2$, the frequency squared reduces to

$$\begin{aligned}\omega^2 &= \frac{4\,c_{s0}^2}{l_t\,(L-l_t)\,\rho_t/\rho_0} + \frac{g\,\pi}{L-l_d} \\ &= \frac{4\,c_{s0}^2}{l_t\,(L-l_t)\,\rho_t/\rho_0} + \frac{g}{|R_L|}.\end{aligned} \tag{5.17}$$

Equation (5.17) is the same expression as Equation (25) of Luna et al. (2012a), considering that they defined L as the half of the total length of the structure and l_t the half of the thread length, and knowing that in our study ρ_t/ρ_0 is the density contrast at the corona-thread interface initially located at $s = L/2 - l_t/2$. Equation (5.17) is always positive for valid values of the parameters, i.e. $L > l_t$, so that we obtain that for $s_0/L = s_e/L = 0.5$ the fixed point is always stable when $l_t < l_d$. Another significant aspect of the derivative of the average gravity (for $l_t < l_d$), Equation (5.13), is that $\bar{g}'_\parallel(s) < 0$ for $L/2 - l_d/4 < s < L/2 + l_d/4$ and $\bar{g}'_\parallel(s) > 0$ anywhere else. Consequently, while the fixed point s_e ranges between $L/2 \pm l_d/4$, ω^2 will always be positive since the first term of the right-hand side of Equation (5.16) is always grater than zero. This means that equilibrium points located around the centre of the magnetic field line, i.e., around the bottom of the dip, are always stable, independently of the parameters of the structure. This is different to the results without dips presented in Chapter 4. We obtained that for equilibrium points located at the apex of the loop when $s_0 = L/2$, ω^2 could be positive or negative depending on the parameters of the structure. Imagine that we have a configuration without dips that develops an unstable fixed point at $s_e = L/2$ (see dashed curves of Figure 4.3). If the loop develops a central dip, according to Equation (5.17), the fixed point at the apex would automatically change to stable, without any type of transition. However, if we use the average gravity it results that, when $l_t > l_d$, $\bar{g}'_\parallel(s = L/2)$ can be positive so that from Equation (5.16) we obtain that ω^2 can be negative and the fixed point would preserve the condition of being unstable.

5.3 Equilibrium and frequency analysis for a symmetric dip

To study the equilibrium of a thread embedded in a curved magnetic field with dips we have to solve Equation (5.14). We distinguish between the two cases $l_t \gg l_d$ and $l_t \ll l_d$. First, we

carry out the study for a symmetric dip (see top panel of Figure 5.1). Then in Section 5.4, we analyse the case for a non-symmetric dip (see bottom panel of Figure 5.1).

5.3.1 Case $l_t \ll l_d$

In Section 5.2 we briefly described how the equilibrium points behave when the initial position of the thread is located at the centre of the symmetric dip. However, if we shift s_0 along the flux tube, the symmetry around $s = L/2$ is lost and the distribution of the fixed points changes. In general, we find that different equilibrium points can be created or destroyed, or their stability can change depending on the parameters of the structure. These changes in the dynamics of the system occur at the bifurcation points (see Section 3 of Strogatz 2018). To understand the gravitational instability of our model we construct bifurcation diagrams that represent the equilibrium points of the system (s_e) as a function of a parameter of the structure. Since not all of the fixed points exist for all parameter values, we have to obtain the parameter range computing the bifurcation points by solving Equations (5.14) and (5.15) simultaneously. To label the bifurcation points in the text we use the subscript b and a thin dashed vertical line in the different bifurcation diagrams. To distinguish between stable and unstable fixed points we use a solid line for stable points and a dashed line for unstable ones. Furthermore, in the diagrams we draw the borders of the magnetic dip as thin dotted lines.

Figure 5.4 shows s_e/L as a function of ρ_t/ρ_0 when the initial position of the thread changes. As we previously explained, four different cases are analysed and all of them show a different behaviour. For $s_0/L = 0.5$ (top panel, black curves) we see that the solution at the centre of the dip is valid for all values of ρ_t and, in contrast to the case without dip, it is always stable now (solid line). As ρ_t increases, when $\rho_t > \rho_{tb}$, the system is able to create two symmetric pair of solutions at the lateral sides of the tube. Beyond the bifurcation point $\rho_{tb}/\rho_0 = 143$, each pair of solutions splits into two branches, one stable (solid curve) and an unstable one (dashed curve). This type of bifurcation is called saddle-node bifurcation and it is the basic mechanism by which fixed points are created and destroyed (see Section 3.1 of Strogatz 2018). It is interesting that the inner branches (dashed lines), that are unstable, never fall into the dip when ρ_t increases, as if the dip would act as a barrier. This constraint causes an asymmetry between the two branches of each pair of solutions. This asymptotic characteristic is explained imposing in Equation (5.14) that ρ_t tends to infinity. In this limit we obtain five asymptotes: two at the limits of the structure $s = l_t/2$ and $s = L - l_t/2$; two at the borders of the dip $s = L/2 \pm l_d/2$; and one at the midpoint $s = L/2$. We highlight that in the range $\rho_t > \rho_{tb}$ two qualitative different stable states coexist, namely the central solution and the most external lateral fixed points. One consequence is that the central solution is stable to small perturbations, but not to large ones, in this sense the centre of the dip is locally stable, but not globally stable. A non-linear stability analysis is beyond the scope of the present study but should be investigated in the future.

When $s_0/L = 0.45$ (orange curves in top panel of Figure 5.4), the system still develops the 5 possible solutions, the central one located along the dip and two pairs of fixed points placed one at each side of the tube. Since the system has lost the left-right symmetry, the two saddle-node bifurcations occur at different bifurcation points, the left one at $\rho_{tb}/\rho_0 = 106$ and the right one at $\rho_{tb}/\rho_0 = 181$. As we expected, the central solution, that persists for all values of ρ_t, tends to the bottom of the dip $s_e/L = 0.5$ when ρ_t/ρ_0 increases. Moreover,

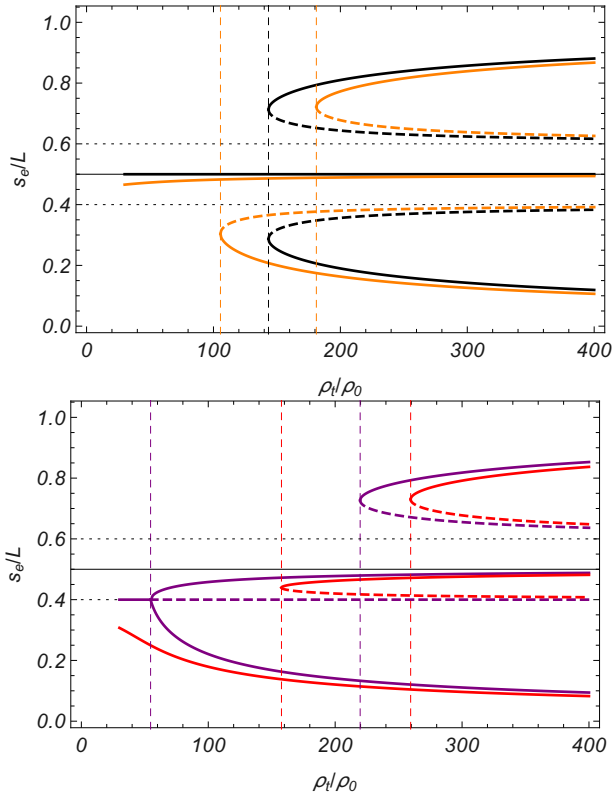

Figure 5.4: Solutions of Equation (5.14) as a function of ρ_t/ρ_0 for $s_0/L = 0.5$ (black curves top panel), $s_0/L = 0.45$ (orange curves top panel), $s_0/L = 0.4$ (purple curves bottom panel), and $s_0/L = 0.35$ (red curves bottom panel). $L = 10\,H$, $l_t = 0.2\,H$, and $l_d = 2\,H$. The thin dashed vertical lines correspond to the bifurcation values that have been calculated by solving Equations (5.14) and (5.15). The thin dotted horizontal lines correspond to the limits of the dip.

as for $s_0/L = 0.5$, we obtain that the inner branches never enter into the dip because of the asymptotes. For $s_0 = L/2 - l_d/2$ (bottom panel, purple curves) the system is characterised by a saddle-node bifurcation plus a pitchfork bifurcation (see Section 20.1 of Wiggins 2003, and Chapter 4), each of them with the corresponding bifurcation point. If we initially place the thread at the left border of the dip, the saddle-node appears at the right side of the tube. When the thread density is below the pitchfork point $\rho_{tb}/\rho_0 = 55$, the only fixed point is located at the left border of the thread and it is stable. For $\rho_t = \rho_{tb}$, $s_e = L/2 - l_d/2$ remains as an equilibrium point, but two new fixed points are created now. In the process, $s_e = L/2 - l_d/2$ becomes unstable and the two emerged branches are stable. Finally, if we shift the thread towards the left of the dip, in this case at $s_0/L = 0.35$ (bottom panel, red curves), the structure develops two saddle-nodes, one inside the dip, specifically restricted by the asymptotes at the left half of the dip, and a second one at the right side of the tube; plus a stable solution valid for all values of ρ_t located at the left side of the tube. It is known in bifurcation theory that pitchfork bifurcations are common in problems that have symmetry. When $s_0 = L/2 - l_d/2$ we have a certain symmetry around the left summit of the structure and therefore the pitchfork bifurcation appears. However, this symmetry is broken when the initial position of the thread moves from that point. We can say that

s_0 is an imperfection parameter (see Section 3.6 of Strogatz 2018, and Chapter 4). For $s_0/L = 0.45$ and $s_0/L = 0.35$ we can consider that the pitchfork bifurcation of the bottom panel disconnects into two pieces: the solitary branch consists entirely of stable fixed points, whereas the pair of equilibrium points has both stable and unstable branches. This is called an imperfect bifurcation.

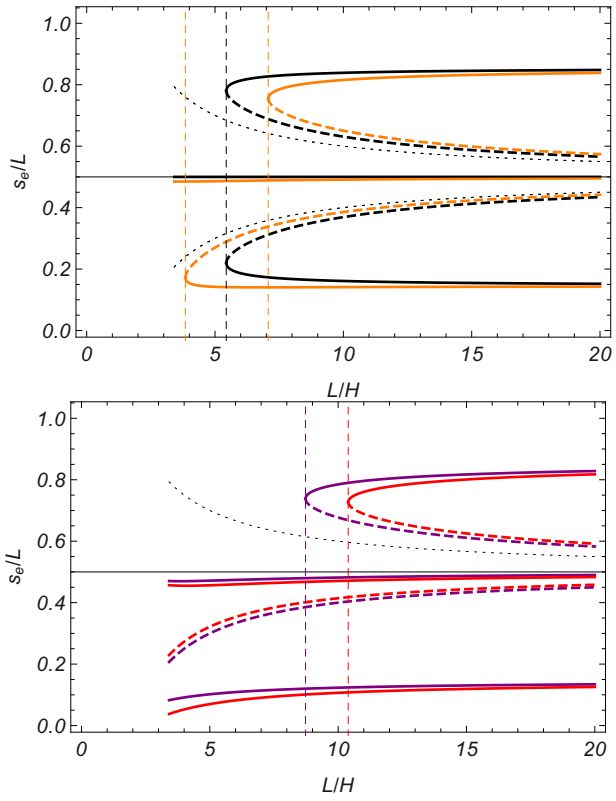

Figure 5.5: Solutions of Equation (5.14) as a function of L. Top panel: $s_0/L = 0.5$ (black curves) and $s_0/L = 0.5 - l_\mathrm{d}/(4\,L)$ (orange curves). Bottom panel: $s_0/L = 0.5 - l_\mathrm{d}/(2L)$ (purple curves) and $s_0/L = 0.5 - 3\,l_\mathrm{d}/(4\,L)$ (red curves). $\rho_\mathrm{t}/\rho_0 = 250$, $l_\mathrm{t} = 0.2\,H$, and $l_\mathrm{d} = 2\,H$. The thin dashed vertical lines correspond to the bifurcation values that have been calculated by solving Equations (5.14) and (5.15). The thin dotted curves correspond to the limits of the dip.

The bifurcation diagrams of s_e as a function of l_t (not shown here) are qualitatively the same as those when we vary ρ_t (for $l_\mathrm{t} \gg l_\mathrm{d}$). However, the diagrams of s_e/L as a function of L, displayed in Figure 5.5, show some peculiarities that must be explained. First, for a fixed l_d, the range of L has a minimum level (see Equation (5.10)), in particular for $l_\mathrm{d} = 2\,H$ we find that $L_\mathrm{min} = 3.4\,H$. In addition, the relative dip length l_d/L varies with L (see thin dotted curves of Figure 5.5), and so does s_0/L. For this reason, we have to set s_0 in terms of L. In the top panel, for $s_0 = L/2$ (black curves) and $s_0/L = 0.5 - l_\mathrm{d}/(4\,L)$ (orange curves) the behaviour of the bifurcation diagrams does not qualitatively change with respect to those in top panel of Figure 5.4. However, when we initially place the thread at the left border of the dip ($s_0/L = 0.5 - l_\mathrm{d}/(2L)$) (bottom panel, purple curves) the saddle-node bifurcation that appears in the $s_\mathrm{e} - \rho_\mathrm{t}$ diagram is still present, but the pitchfork bifurcation is not created, and the only bifurcation point is obtained at $L_\mathrm{b} = 8.7\,H$. Now we have, besides the two

fixed points of the bifurcation, three existing solutions that are valid for the whole range of L: one stable (solid curve) inside the dip around the bottom of the dip $s_e = L/2$, one unstable fixed point (dashed curve) that remains constant at the left border of the dip, and a second stable solution (solid curve) located at the left side of the tube. For the fourth case ($s_0 = L/2 - 3\,l_d/(4\,L)$, bottom panel, red curves) the bifurcation diagram is more or less the same as that for $s_0/L = 0.5 - l_d/(2L)$, but now, the unstable solution that was located at the border is shifted towards the dip.

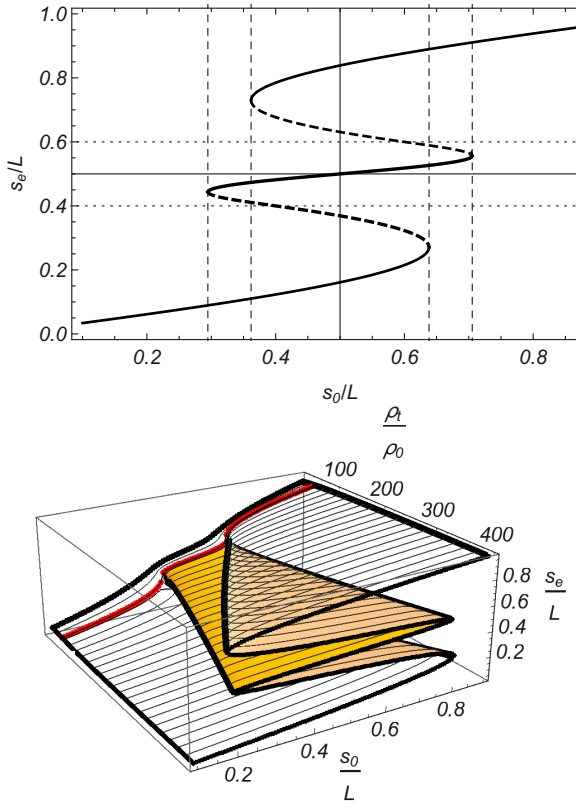

Figure 5.6: Top panel: Solutions s_e of Equation (5.14) as a function of s_0/L for $L = 10\,H$, $l_t = 0.2\,H$, $l_d = 2\,H$, and $\rho_t/\rho_0 = 250$. The thin vertical dashed lines correspond to the bifurcation points. Bottom panel: Three dimensional bifurcation diagrams of s_e as a function of s_0 and ρ_t. The other parameters are the same as those in top panel. The red curve denotes the cusp density ρ_{tc}.

The transition between the four different scenarios is clearer when we plot s_e as a function of the imperfection parameter s_0 (top panel of Figure 5.6). We vary the initial position of the thread from $s_0/L = 0.1$ to $s_0/L = 0.9$ so that we cover the two halves of the tube. The transition between the case $s_0 < L/2 - l_d/2$ (red curves in Figures 5.4 and 5.5) and $s_0 > L/2 - l_d/2$ (orange curves) takes place at $s_0 = L/2 - l_d/2$ (purple curves) where the unstable fixed point inside the dip crosses the border towards the left side of the tube. The bifurcation diagram is characterised by two S-shaped bifurcations (also called imperfect bifurcations) that share one of the branches. For each S-shaped bifurcation, the middle branch is unstable (dashed curve) and the upper and lower branches are stable (solid curves). All the turning points of the S-shaped diagram, four in total, take place at the corresponding bifurcation point. In Figure 5.6 (bottom panel) we plot a three dimensional diagram of s_e as

a function of the two independent parameters s_0 and ρ_t. We can see that when ρ_t decreases, the bifurcation curves $s_{0b}(\rho_t)$ meet at $s_{0b}(\rho_{tc})/L = 0.5 \pm l_d/(2\,L)$. ρ_{tc} (see red curve in the bottom panel) is called a cusp point and it has been calculated by solving Equations (5.14) and (5.15) simultaneously for $s_0/L = 0.5 \pm l_d/(2\,L)$. The cusp point $\rho_{tc}/\rho_0 = 55$ coincides with the pitchfork point of bottom panel of Figure 5.4. Below ρ_{tc} the system only develops one fixed point independently of s_0.

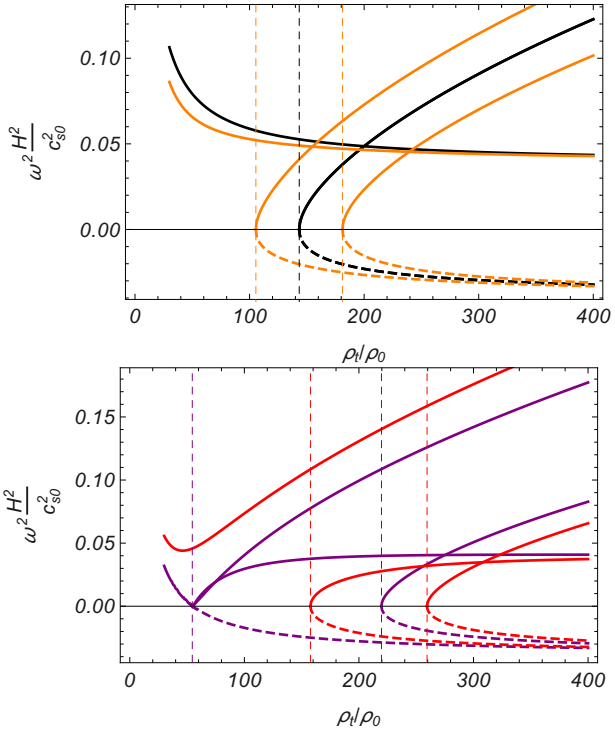

Figure 5.7: ω^2 as a function of ρ_t/ρ_0. Top panel: $s_0/L = 0.5$ (black curve) and $s_0/L = 0.45$ (orange). Bottom panel: $s_0/L = 0.4$ (purple curves) and $s_0/L = 0.35$ (red curves). $L = 10\,H$, $l_t = 0.2\,H$, and $l_d = 2\,H$. The thin dashed vertical lines correspond to the bifurcation points. The results shown here correspond to the equilibrium points of Figure 5.4.

Bifurcation theory explains the stability of the equilibrium solutions which is further confirmed by the following frequency analysis. To have a stable fixed point the condition $\omega^2 > 0$ must be satisfied. We saw in Section 5.2.3 that for $l_t \ll l_d$, the fixed points located around the centre of the dip ($L/2 - l_d/4 < s_e < L/2 + l_d/4$) will always be stable. However, when $s_e < L/2 - l_d/4$ or $s_e > L/2 + l_d/4$, the equilibrium points can be stable or unstable. Figure 5.7 shows ω^2 (Equation (5.16)) as a function of ρ_t/ρ_0 for the equilibrium points obtained in Figure 5.4. In the top panel, as we expected, we see that the frequency squared of the central solution for $s_0 = L/2$ (black curves) and $s_0/L = 0.45$ (orange curves) is always positive and it decreases with ρ_t. In addition, each pair of fixed points of the saddle-node bifurcation has a positive (stable) branch and a negative (unstable) one. This result agrees with what we expect from bifurcation theory. Furthermore, for the symmetric case $s_0 = L/2$ (black curves) we obtain that the frequency squared of each bifurcation is the same. For $s_0 = L/2 - l_d/2$ (bottom panel, purple curves) we see that ω^2 corresponding to the fixed point located at the border of the dip inverts the sign at the pitchfork point $\rho_{tb}/\rho_0 = 55$ so that the stability changes at this point. As bifurcation theory predicts, we obtain that

beyond the pitchfork point both emerged solutions have a positive ω^2. For the three saddle-node bifurcations obtained in the bottom panel of Figure 5.4 (one for $s_0/L = 0.4$ and two for $s_0/L = 0.35$) we obtain again that $\omega^2 > 0$ for one branch and $\omega^2 < 0$ for the other one.

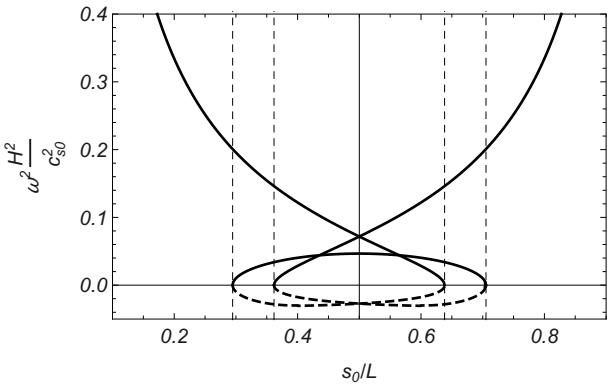

Figure 5.8: ω^2 as a function of s_0 for $L = 10\,H$, $l_\mathrm{t} = 0.2\,H$, $l_\mathrm{d} = 2\,H$, and $\rho_\mathrm{t}/\rho_0 = 250$. The thin dashed vertical lines correspond to the bifurcation points. The results shown here correspond to the equilibrium points of Figure 5.6.

The result of the calculation of ω^2 for the two S-shaped bifurcations of Figure 5.6 is a ribbon-like diagram, shown in Figure 5.8. The two curves corresponding to the most external fixed points cross each other at $s_0 = L/2$, meaning that for the symmetric case ω^2 is the same for mirrored solutions. At the four bifurcation points the stable branches (solid curves) join with the unstable ones (dashed curves) at $\omega^2 = 0$. The unstable branches also cross at $s_0 = L/2$ to close the ribbon.

We finish this section with a brief illustration using typical prominence parameters. We consider a magnetic flux tub of length $L = 100\,\mathrm{Mm}$ with a dip of length $l_\mathrm{d} = 20\,\mathrm{Mm}$ so that the radius at the midpoint of the structure (Equation (5.9)) is $R_\mathrm{d}\,(s = L/2) \approx -25.5\,\mathrm{Mm}$. The negative value of the radius means that the curvature of the flux tub at this point is concave upwards. We take a prominence thread of length $l_\mathrm{t} = 2\,\mathrm{Mm}$ and a density contrast $\rho_\mathrm{t}/\rho_0 = 100$. We consider that the thread is initially placed at the centre of the structure so that $s_0 = L/2$. Then we consider a coronal sound speed $c_{s0} = 166\,\mathrm{km\,s^{-1}}$ and a gravity acceleration $g = 0.274\,\mathrm{km\,s^{-2}}$. Under these conditions and using Equation (5.16), we obtain that the period of oscillation is $P = 2\pi/\omega \approx 25.9\,\mathrm{min}$. For larger flux tubes and heavier threads, e.g. $L = 200\,\mathrm{Mm}$ and $\rho_\mathrm{t}/\rho_0 = 250$, but keeping the rest of variables unchanged so that $R_\mathrm{d}\,(s = L/2) \approx -57.3\,\mathrm{Mm}$, the oscillatory period is $P \approx 43.2\mathrm{min}$. According to the study of Luna et al. (2018), the period for longitudinal oscillations ranges from 30 min to 110 min, with a strong peak centred at 58 min, so that the theoretical periods obtained by our model underestimate the observed periods although they are of the same order of magnitude.

5.3.2 Case $l_\mathrm{t} \gg l_\mathrm{d}$.

To study the transition between a magnetic configuration without dips and another one with dips we simply consider an initial configuration where $l_\mathrm{t} \gg l_\mathrm{d}$ and then we increase l_d.

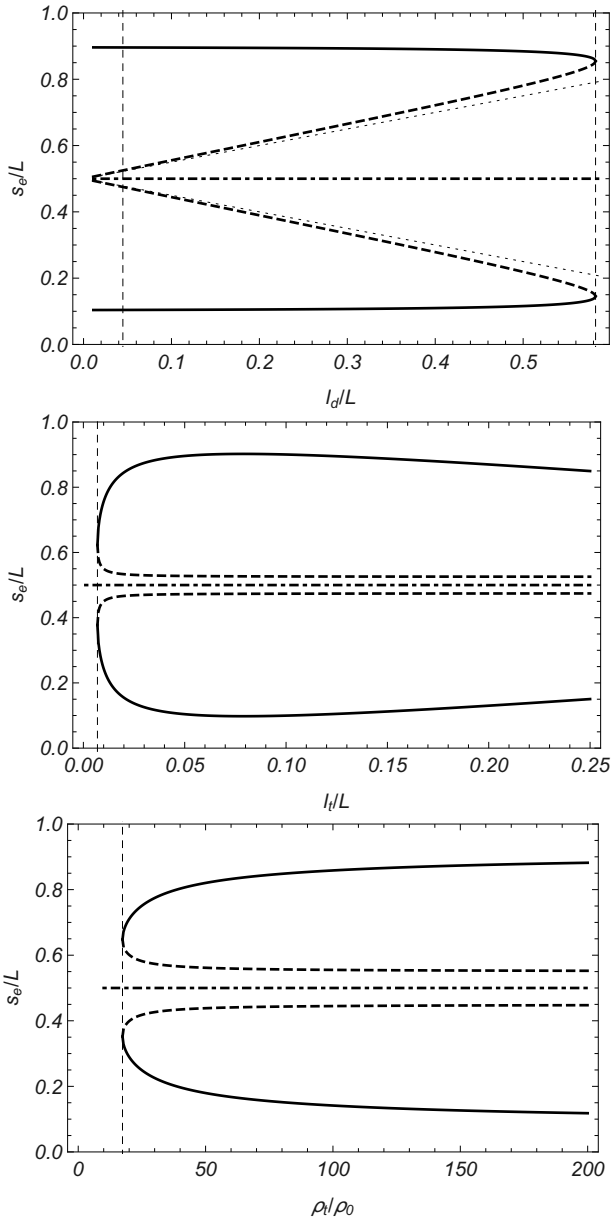

Figure 5.9: Top panel: bifurcation diagram of s_e/L as a function of l_d/L for $L = 10\,H$, $\rho_\mathrm{t}/\rho_0 = 250$, and $l_\mathrm{t} = 0.5\,H$. Middle panel: s_e/L as a function of l_t/L for $L = 10\,H$, $\rho_\mathrm{t}/\rho_0 = 250$, and $l_\mathrm{d} = 0.5\,H$. Bottom panel: s_e/L as a function of ρ_t/ρ_0 for $L = 10\,H$, $l_\mathrm{t} = 1.5\,H$, and $l_\mathrm{d} = H$. In the three panels $s_0/L = 0.5$. The thin dashed vertical lines correspond to the bifurcation points.

We focus on the case $s_0 = L/2$ so that we will have left-right symmetry. The top panel of Figure 5.9 shows the bifurcation diagram of s_e as a function of l_d. We vary l_d from $0.1\,H$ to l_dmax (see Equation (5.11)), being $l_\mathrm{t} = 0.5\,H$, $L = 10\,H$, and $\rho_\mathrm{t}/\rho_0 = 250$. For $L = H$, $l_\mathrm{dmax} = 5.9\,H$. For $l_\mathrm{d} = 0.1\,H$, the bifurcation system develops five equilibrium points: one around each loop foot (solid curves), one at the centre of the structure (solid curve) and two solutions that tend to $s_\mathrm{e} = L/2$ (dashed curves). As in Section 5.3, the dotted thin lines represent the borders of the dip. When the length of the dip increases,

the fixed point $s_e = L/2$ remains constant at the bottom of the dip. The solutions around the feet do not change much. However, the other two equilibrium points move away from the centre as l_d increases, always staying outside of the dip. When the bifurcation point $l_{db} = 5.8\,H$ is reached, the two branches of each pair of external solutions merge, destroying the fixed points. The diagram qualitatively describes two inverted saddle-node bifurcations plus a central fixed point valid for all values of l_d. From bifurcation theory we know that one branch of the saddle-node is stable (the most external one) and that the second one is unstable. However, while the stability of the central fixed point for $l_t \ll l_d$ was clearly stable, now the stability of $s_e = L/2$ needs a detailed analysis.

In general, the top panel of Figure 5.9 describes a modified subcritical pitchfork bifurcation (see Figure 3.4.7 of Strogatz 2018). This type of bifurcation is characterised by a locally stable central fixed point for values beyond a first bifurcation point (three-branches bifurcation) plus two forward-bending branches of unstable fixed points that bifurcate from the midpoint at the bifurcation point. The unstable branches reverse and become stable at a second saddle-node bifurcation point. From bifurcation theory we would obtain that the central solution is stable for all values of l_d. However, due to the characteristics of our model, from the frequency analysis we will see that below $l_d = 0.5\,H$, i.e., when $l_d < l_t$, the system develops 'critical' points that change the stability of the system. These critical points are obtained by the same method used for bifurcation points, but now at these points the system does not bifurcate and does not create new fixed points. One of these critical points is plotted as a thin dashed vertical line in the top panel of Figure 5.9 ($l_{dc} = 0.45\,H$). We call this fixed point a 'fitful' point and it is displayed in the bifurcation diagram as a dot-dashed curve. Middle and bottom panels of Figure 5.9 show the bifurcation diagram of s_e as a function of l_t and ρ_t, respectively, for values of the thread length longer than the dip length. The diagrams are visually equivalent to that in the top panel of Figure 5.4 for $s_0 = L/2$. However, when we analyse the frequency squared, we again obtain that the central fixed point is a fitful point.

Now, we analyse ω^2 as a function of l_d for the equilibrium points shown in the top panel of Figure 5.9 by solving Equation (5.16). The top panel of Figure 5.10 shows that the two branches of the saddle-node bifurcations merge at $\omega^2 = 0$ for $l_{db} = 5.8\,H$. As we expected from bifurcation theory, one branch is negative and the other one is positive. For the central solution $s_e = L/2$, we obtain that for large values of l_d ($l_d > l_t$), $\omega^2 > 0$ so that the fixed point is stable. Up to this point there is no contradiction between the frequency analysis and bifurcation theory. However, when $l_d < l_t$, we obtain that ω^2 oscillates around zero. For the parameters we are using, ω^2 only takes negative values for one range of values, namely from $l_{db} = 0.28\,H$ to $l_{db} = 0.45\,H$ (see left thin dashed vertical line); however, if for example we increase the value of ρ_t (not shown here) more than one zero-cross is found. The result is called the fitful fixed point and it is a consequence of using the average gravity. As we explained in Section 5.2.1, the term $\sin\left(\pi \frac{l_t}{l_d}\right)$ in Equation (5.13) may invert periodically the sign of $\bar{g}'_{\parallel}(s)$ that, in turn, changes the stability of the structure. The oscillatory pattern in the stability of $s_e = L/2$ is also shown in the middle panel of Figure 5.10, where ω^2 is presented as a function of l_t. Now the fitful point has more than one unstable region when $l_t > l_d$.

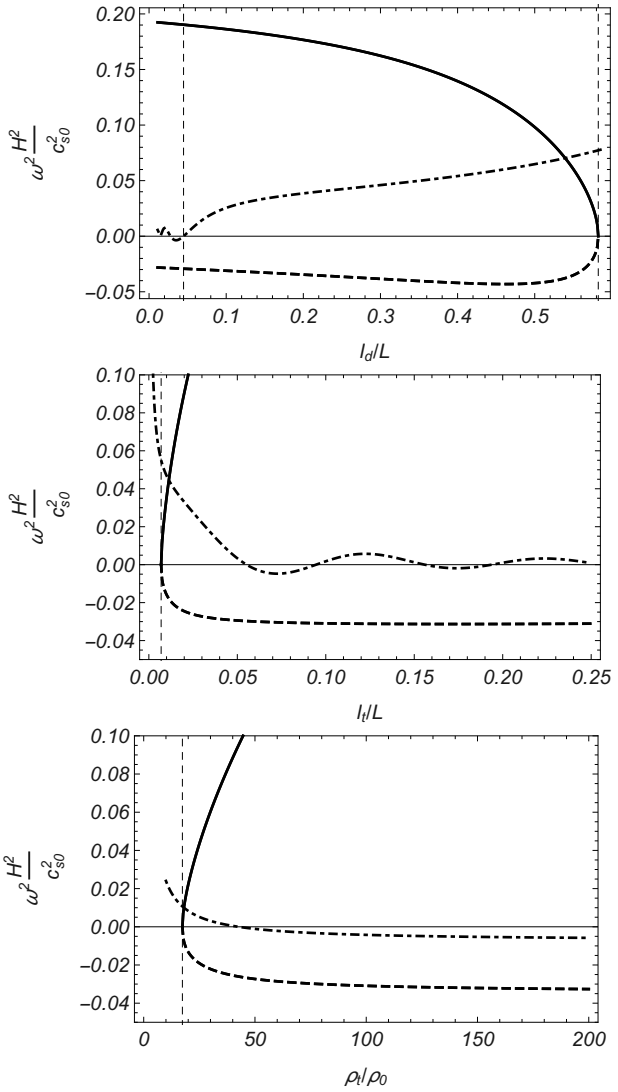

Figure 5.10: ω^2 corresponding to the fixed points of Figure 5.9.

Finally, when we fix $l_\mathrm{d} = 1\,H$ and $l_\mathrm{t} = 1.5\,H$, the term $\sin\left(\pi\frac{l_\mathrm{t}}{l_\mathrm{d}}\right)$ is constant so that $\bar{g}'_\parallel(s)$ loses the periodic feature. In this way, when we vary ρ_t (bottom panel of Figure 5.10), the fitfully nature of the fixed point $s_\mathrm{e} = L/2$ disappears and only one change in the stability for $\rho_{\mathrm{t}c}/\rho_0 = 43$ occurs. While $\rho_\mathrm{t} < \rho_{\mathrm{t}c}$, the fixed point $s_\mathrm{e} = L/2$ is stable, but as the thread becomes heavier, the equilibrium point changes to being unstable. This finding is important because we have found that a heavy plasma thread located in a short magnetic dip can be unstable and this result is a direct consequence of using the average gravity.

5.4 Equilibrium and frequency analysis for a non-symmetric dip

All previous figures correspond to a magnetic dip located at the centre of the structure. However, we can shift the bottom of the dip imposing that $g_\parallel(s = s_\mathrm{B}) = 0$, being s_B its

position. In order to do this, we have to define four different regions of $g_{\parallel}(s)$ instead of the three utilised in Equation (5.1) by imposing continuity in its derivative. The external regions are the same as those when the dip is centred. The two dip regions are defined by two sine functions separated at $s_{\rm B}$, that ranges between $s = L/2 \mp l_{\rm d}/2$. When we move $s_{\rm B}$ towards left, the right circular segment rises so that we have to impose a vertical leg of length $h = y(L)$ that joins the loop with the chromosphere. In this way, $g_{\parallel}(s)$ is given by

$$g_{\parallel}(s) = \begin{cases} -g\,\cos\left(\pi\frac{s}{L-l_{\rm d}}\right) & 0 < s < s_1, \\ g\frac{s_{\rm b}}{2\,(L-l_{\rm d})}\,\sin\left(\frac{2\,\pi}{s_{\rm b}}\,(s - s_1 + s_{\rm b})\right) & s_1 < s < s_1 + \frac{s_{\rm b}}{2}, \\ -g\frac{2\,l_{\rm d}-s_{\rm b}}{2\,(L-l_{\rm d})}\,\sin\left(\frac{2\,\pi\left(s-s_1-2\,l_{\rm d}+\frac{s_{\rm b}}{2}\right)}{2\,l_{\rm d}-s_{\rm b}}\right) & s_1 + \frac{s_{\rm b}}{2} < s < s_1 + l_{\rm d}, \\ g\,\sin\left(\pi\frac{s-s_1-l_{\rm d}}{L-l_{\rm d}}\right) & s_1 + l_{\rm d} < s < L, \\ g & L < s < L + h, \end{cases} \tag{5.18}$$

being $s_{\rm B} = s_1 + \frac{s_{\rm b}}{2}$. A sketch of the non-symmetric model is plotted in bottom panel of Figure 5.1.

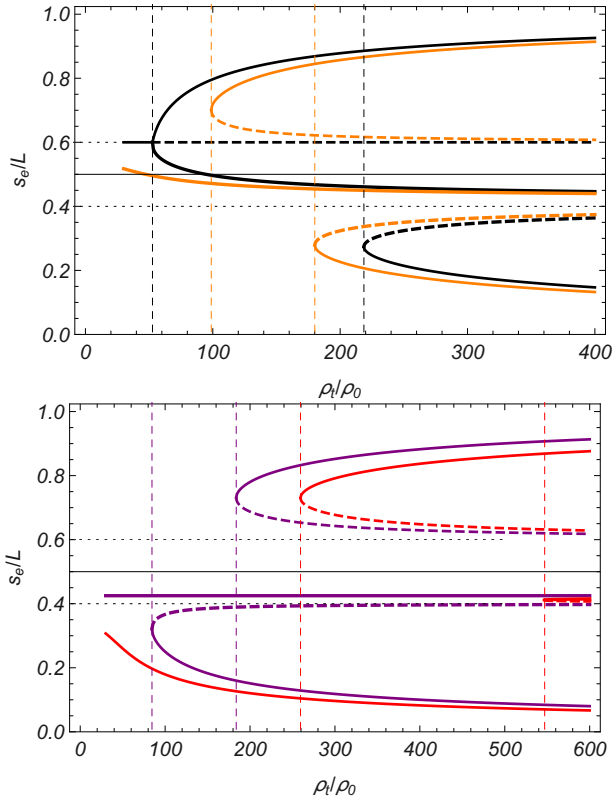

Figure 5.11: $s_{\rm e}$ as a function of $\rho_{\rm t}$ for $L = 10\,H$, $l_{\rm d} = 2\,H$, $l_{\rm t} = 0.2\,H$, and $s_{\rm B} = 4.25\,H$. $s_0/L = 0.6$ (black curves top panel), $s_0/L = 0.55$ (orange curves top panel), $s_0/L = s_{\rm B}/L$ (purple curves bottom panel), and $s_0/L = 0.35$ (red curves bottom panel).

Now when the equation of the equilibrium points, Equation (5.14), is solved, we have to take into account that the total length of the tube is $L + h$. We focus on the case $l_{\rm d} \gg l_{\rm t}$ and we

only study the dependence of the system on the density of the thread. Figure 5.11 shows s_e as a function of ρ_t for different values of s_0 when $L = 10\,H$, $l_d = 2\,H$, $l_t = 0.2\,H$, and $s_B = 4.25\,H$. For this set of parameters, we obtain that $h \approx 0.24\,H$. First of all, we set s_0 at the right border of the dip (top panel, black curves). As in the bottom panel of Figure 5.4, when we initially place the thread at some border of the dip, the system develops a pitchfork bifurcation plus a saddle-node bifurcation. However, since we have changed the position of the bottom of the dip, the inner branch of the pitchfork bifurcation tends to $s_e = s_B$ when ρ_t increases instead of $s_e = L/2$ as in the symmetric case. Since we initially place the thread at the right of the tube, and the bottom of dip is located at the left side of the dip, the central fixed point has to cross through $L/2$, meaning that now the asymptote is not placed at the centre of the structure but at s_B. When we move the initial thread position towards the dip, at $s_0/L = 0.55$ (see orange curves top panel), the pitchfork bifurcation disconnects into two parts, one saddle-node bifurcation plus a fully stable fixed point valid for all values of ρ_t. The central solitary branch also tends to s_B with increasing ρ_t. The bottom panel purple curves show the bifurcation diagram for an initial position of the thread located at the bottom of the dip. As in the top panel of Figure 5.4 we have that the central fixed point remains located at its original position, but now, since we lost symmetry, the two saddle-node bifurcations have a different bifurcation point. Finally, we set $s_0/L = 0.35$. The system develops two saddle-node bifurcations plus a fixed point at the left side of the tube that exists for all values of ρ_t. The greatest difference between the symmetric and the non-symmetric dip for $s_0/L = 0.35$ is that the saddle-node bifurcation located inside the dip is tighter because it is close to the two asymptotes.

An important aspect of the new structure is the role played by the vertical leg. We obtained that the vertical leg we inserted in the structure of the non-symmetric dip hardly contributes to the behaviour of the system. Basically, it slightly modifies the position of the bifurcation points and disrupts the curve of the fixed point closest to the right foot. Finally, we have to mention that the frequency analysis (not shown here) shows the same behaviour as the one in Section 5.3.1.

5.5 Conclusions and discussion

Solar prominences are composed of collections of individual cold plasma threads embedded in magnetic flux tubes that support the heavy material against the gravity force which pulls the structure downwards. In principle, to counteract the gravity force, the plasma must be placed within concave upwards regions called magnetic dips. However, by means of numerical simulations we found that magnetic structures with dips do not guarantee the stability of prominences. Specifically, in Chaper 3 we found that the model of prominence developed by Hood & Anzer (1990) cannot support the dense plasma when it is longitudinally perturbed and that the magnetic shear does not stabilise the structure. On the contrary, we do not find this instability linked to lateral displacements in plasma structures embedded in an isothermal stratified atmosphere permeated by unsheared dipped magnetic arcades (Terradas et al. 2013; Luna et al. 2016b; Adrover-González & Terradas 2020) or by sheared magnetic flux ropes (Zhou et al. 2018; Liakh et al. 2020). In the present chapter we have tried to clarify whether prominence threads can be stable at regions without magnetic dips. We solved the most elementary hydrostatic equations which include the gas pressure force together with the gravity force to obtain an expression for the equilibrium points and their frequency in a simple circular model of a thread in a magnetic dip. We have not included thermal processes or ionisation effects in the equations.

First, we considered a magnetic structure with a well formed dip filled by a short thread initially placed at the midpoint of the structure. We found that the flux tube can develop five equilibrium points. One of the fixed points is located inside the dip and it exists for the whole range of parameters. For this central fixed point or equilibrium point the thread is stable and can oscillate under the presence of perturbations. We obtained an analytical expression, Equation (5.17), that provides its frequency. This result coincides with the finding of Luna et al. (2012a). They proposed that the two terms of Equation (5.17) contribute to oscillations by different mechanisms. The term

$$\omega_s^2 = \frac{4\, c_{\rm s0}^2}{l_{\rm t}\ (L - l_{\rm t})\ \rho_{\rm t}/\rho_0}, \tag{5.19}$$

is the pressure-driven slow oscillation frequency, and

$$\omega_g^2 = \frac{g}{|R_{\rm L}|}, \tag{5.20}$$

is the gravity-driven frequency. Equation (5.20) is the frequency of the pendulum model (see Equation (1.2)). Luna et al. (2012a) suggested that for a large curvature radius, which occurs in large flux tubes with short dips (Equation (5.9)), the primary contribution to the restoring forces is the pressure gradient, while for a small radius it is mainly the solar gravity force. From the physical point of view, the concave upwards shape of the magnetic field leads to a magnetic tension force that counteracts the gravity force.

Apart from the trivial solution hosted by the dip, the system can develop four more equilibrium points at the lateral edges of the tube. When we have symmetry regarding the midpoint the existing fixed points are also symmetric and we can group them by pairs. Only one solution of each pair (those located at lower heights) is stable. Now, the force that can support the dense plasma against the gravity is the pressure gradient. We obtained

that along the flux tube three qualitatively different stable equilibrium points can coexist, meaning that the trivial one is stable to small perturbations but not to large ones. In this sense, the dip holds up locally stable threads but not globally stable ones. The result of having multiple static thread structures has been studied by other authors. Terradas et al. (2021, in preparation) studied the equilibrium of a one-dimensional model of thread subject to hydrostatic and thermal balance. They found, under some selection of parameters, the existence of a secondary thread-like structure not necessarily located at the dips of the magnetic fields. In addition, An et al. (1988) and Wu et al. (1990) studied the formation of solar prominences by mass injection in a Kippenhahn-Schlüter model of prominence. While An et al. (1988) considered ideal MHD equations, Wu et al. (1990) introduced radiation and thermal conduction. In their studies the initial magnetic field does not have dips but when the plasma is injected the system is able to develop central dips. For strong fields, the plasma hardly bends the lines so that the plasma falls down and accumulates at both legs of the arcade as well as at the apex, forming a loop-like prominence. On the other hand, when the dip is well formed plasma is suspended there. It is also shown that the formation process by mass injection is sensitive to the amount of density and flux velocity. In Wu et al. (1990), when they increase the amount of mass or the injection velocity, plasma condenses before it reaches the apex so that it accumulates at both legs of the loop structure. Since the prominence formation is a dynamic process in a way that the density and the dimensions of the cold plasma or the magnetic dip change with time, there are obvious difficulties in comparing the results of An et al. (1988) and Wu et al. (1990) with our static solutions. However, under specific conditions, the support of prominence mass does not only occur due to the magnetic tension of the dip but also due to an increase in the pressure gradient.

When the thread is not initially placed at the bottom of the dip, the system still develops five different fixed points. In summary, the equilibrium points distribute among three stable solutions and two unstable ones in diverse bifurcation diagrams. The different diagrams have in common that, when $\rho_{\rm t}$ increases, the five fixed points tend asymptotically to the bottom of the dip $s_{\rm e} = L/2$, to the borders of the dip $s_{\rm e} = L/2 \pm l_{\rm d}/2$, and to the limits of the structure $s_{\rm e} = l_{\rm t}/2$ and $s_{\rm e} = L - l_{\rm t}/2$, respectively. When the structure has a non-symmetric dip, it has, in essence, a similar behaviour but now the central fixed point tends to $s_{\rm e} = s_{\rm B}$.

A second aim of this chapter was to investigate the gravitational instability for the transition between a thread embedded in curved magnetic fields without dips and a structure with dips. We considered threads longer than the length of the dip ($l_{\rm t} > l_{\rm d}$) and we obtained that the fixed point located at the bottom of the dip is stable for low densities but becomes unstable for densities larger than a critical value. This critical point, where the stability changes, does not behave as a bifurcation point in the sense that no new branches appear or disappear as it occurs for the saddle-node or the pitchfork bifurcations. On the contrary, for the other fixed points which are located at the lateral edges of the tube, the bifurcation theory results remain valid. This critical point is more exceptional when we fix the density but vary the thread or dip length. Now, the central fixed point develops more than one critical point and the stability of the thread oscillates between stable and unstable states. We called this fixed point a fitful point. This finding is a direct consequence of using the average gravity instead of the projected gravity along the thread. However, the use of $\bar{g}_{\parallel}(s)$ is necessary to explain the transition between an unstable fixed point placed at the apex of a curved magnetic field without dip and another one with dips.

Conclusions and future work

In this Thesis we have investigated three-dimensional numerical simulations of oscillations in solar prominences and gravitational instabilities in threads. The manuscript is divided into five main chapters, of which the first one contains a general introduction into the physics of solar prominences, with a special focus on oscillations in prominences. A short overview about numerical simulations of oscillations in general as well as the description and a first analysis of the simulations performed in the frame of this Thesis is presented in Chapter 2. The unexpected numerical results of unstable prominences have led to a theoretical study of their equilibrium which is conducted in Chapter 3. An investigation of gravitational instabilities in threads is carried out in the Chapters 4 and 5. Initially, the main objective of this Thesis was to study, by means of 3D MHD simulations, the excitation by external agents of large amplitude oscillations in prominences, and specifically, to analyse the dynamics depending on the impact angle of the passing wave, its energy, the distance from its origin and the features of the coronal atmosphere, such as the magnetic field or the density background. Unfortunately, several of these goals had to remain unanswered or could only be partially solved. Nevertheless, we have advanced regarding the knowledge of other important questions.

In Chapter 2, oscillations in solar prominences have been numerically analysed with regard to a wide range of parameters as well as different polarisation of motions. First of all, it is important to mention that the ideal MHD equations, despite being a simple model, provide a good approximation that describes many of the dynamical properties of hot, strongly magnetised plasma. Our model represents a good approximation of a prominence body that nearly reproduces the observed oscillations. We have succeeded in inducing oscillations on highly dense plasma with very steep profiles. We have analysed the periods and damping times of the oscillations that reflect the physics responsible for driving and attenuating the motions. We found that the main restoring force of longitudinal oscillations is the field-aligned component of gravity, following the pendulum model, even though other mechanisms such as pressure gradients may contribute to the movement too. On the other hand, transverse oscillations are subject to magnetic forces. The periodicity of the oscillations is sensitive to the parameters of the system in such a way that each prominence oscillates at its own frequency. The analysis of the parametric survey in Chapter 2 shows, in agreement with observational studies, that the oscillation period increases with the prominence width. For transverse oscillations we obtained that P increases with density and decreases with B. For longitudinal oscillations we also found that P increases with ρ_{p0}, but there are no variations with B. A sort of novelty, being described in Chapter 2, is the treatment of the attenuation mechanism for transverse oscillations. The Alfvén continuum modes of the MHD equations

were computed for different field lines in order to provide a map of the arrangement of the characteristic period of the system. Our method compares the global oscillatory mode inferred from the time dependent simulations with the accumulated kinetic energy due to the energy conversion of the resonant absorption process. We found that the resonance surface of the transverse motions matches in space the location where the kinetic energy increases. The evidence from this study suggests that the main process of attenuation of transverse oscillations is resonant absorption. Finally, the insights gained from this chapter might be useful to determine the polarisation of motion for observed oscillatory events in solar prominences.

In Chapter 3, we have shown that the investigation of 3D numerical simulations of oscillations triggered by external perturbations in highly sheared magnetic fields has not been completed. The principal limitation of the numerical experiment is the magnetic field model we utilised. There is evidence that magnetic dips play a crucial role in supporting and confining the dense plasma. Unfortunately, when we impose a strong shear in the magnetic arcade, the distribution of dips changes. Such behaviour has made it impossible that our model of prominences remains stable during the oscillations. Oscillations perpendicular to the magnetic fields trigger flows of dense plasma along the field lines falling to the chromosphere, and the dips in this case do not allow a prominence suspended in the corona. In addition, the periodic nature of the arcades prevents placing the external disturbance pulses far from the prominence body. Something similar happens when we use the prominence model of Hood and Anzer. However, in this chapter we have presented a method capable of simulating non-linear shock waves strong enough to activate oscillations in filaments. The pressure, the density and the magnetic variations in the wave are related to the velocity disturbance through the continuity, the momentum and the induction equations. In terms of future work, we think that these preliminary results will be helpful in the near future to perform highly non-linear simulations in solar prominences. It would be an interesting task to repeat the numerical experiments described in the first part of the Thesis using magnetic field models capable to hold up the dense plasma. A good candidate for such a study might be 3D magnetic flux ropes (see Terradas et al. 2016; Zhou et al. 2018). We have proposed a new methodology for simulating external perturbations that could improve the knowledge about the dependence of the impact angle on the excitation of different modes in 3D simulations.

In the second part of this Thesis the gravitational instability of solar threads has been investigated using curved magnetic fields with and without magnetic dips. Based on purely hydrodynamic equations in one spatial dimension, and applying line-tying conditions at the footpoints of the magnetic field lines, we derived analytical expressions for the different feasible equilibria and the corresponding frequencies of oscillation. In Chapter 4 we assumed that the shape of the magnetic field is circular, with no dips. We have found that the system allows stable and unstable equilibrium solutions subject to the initial position of the thread, its density contrast and its length, and the total length of the magnetic field lines. Interestingly, the transition between the two types of solutions is produced at specific bifurcation points that have been determined analytically in some particular cases. When the thread is initially at the top of the concave magnetic field, i.e., at the apex, we find a supercritical pitchfork bifurcation, while for a shifted initial thread position with respect to this point the symmetry is broken, and the system is characterised by an S-shaped bifurcation. These findings are completely novel results in the field of prominence stability and oscillations.

The gravitational instability analysis for curved magnetic fields including a magnetic dip has been presented in Chapter 5. We have investigated structures with symmetric magnetic dips and others with shifted dips. Now the system allows up to five equilibrium points whose stability can be explained by bifurcation theory. In Chapter 4 we used the projected gravity along the magnetic field lines. However, since the thread has a finite length, gravity changes along it, and under the presence of dips we have found it to be more convenient to use the average gravity on the thread. The first approximation is valid only for structures with long dip and short thread lengths. In a well formed prominence, where the cold plasma is hosted by a large dip, we found that the system develops an equilibrium solution at the bottom of the dip that is stable for the whole range of parameters. On the other hand, in order to investigate transitions between one flux tube without dip to another one with dip, we considered a thread larger than the dip. In this case, the central solution develops critical points changing the stability of the thread. The nature of the so-called fitful points remains unclear but they make the existence of unstable equilibria possible, when the dip begins to form. However, further research regarding this topic needs to be performed in the future.

The study carried out in the second part of this Thesis is elementary in the sense that the physics we have utilised is quite basic and we have omitted important processes such as radiation, thermal conduction and heating. This fact makes it difficult to reliably compare the results obtained in our study with actual prominence observations. Nevertheless, in spite of the simplifications of our model, we think that the results presented here shed new light on the behaviour of threads in curved magnetic fields under the presence of gravity and help to interpret more complex numerical MHD simulations about similar structures. However, in order to confirm and validate these findings, including numerical simulations in curved magnetic fields, with and without dips, is an important issue for future research.

Bibliography

Adrover-González, A. & Terradas, J. 2020, Astronomy and Astrophysics, 633, A113

Alfvén, H. 1942, Nature, 150, 405

An, C. H., Bao, J. J., Wu, S. T., & Suess, S. T. 1988, Solar Physics, 115, 93

Antiochos, S. K., MacNeice, P. J., & Spicer, D. S. 2000, Astrophysical Journal, 536, 494

Antolin, P., Okamoto, T. J., De Pontieu, B., et al. 2015, Astrophysical Journal, 809, 72

Antolin, P. & Rouppe van der Voort, L. 2012, Astrophysical Journal, 745, 152

Antolin, P., Vissers, G., & Rouppe van der Voort, L. 2012, Solar Physics, 280, 457

Arregui, I. & Ballester, J. L. 2011, Space Science Reviews, 158, 169

Arregui, I., Oliver, R., & Ballester, J. L. 2018, Living Reviews in Solar Physics, 15, 3

Arregui, I., Terradas, J., Oliver, R., & Ballester, J. L. 2008, Astrophysical Journal, Letters, 682, L141

Ballester, J. L. 2014, in IAU Symposium, Vol. 300, Nature of Prominences and their Role in Space Weather, ed. B. Schmieder, J.-M. Malherbe, & S. T. Wu, 30–39

Ballester, J. L. 2015, Magnetism and Dynamics of Prominences: MHD Waves, ed. J.-C. Vial & O. Engvold, Vol. 415, 259

Ballester, J. L., Alexeev, I., Collados, M., et al. 2018, Space Science Reviews, 214, 58

Berger, T. E., Shine, R. A., Slater, G. L., et al. 2008, Astrophysical Journal, Letters, 676, L89

Bernasconi, P. N., Rust, D. M., & Hakim, D. 2005, Solar Physics, 228, 97

Bhatnagar, A. & Livingston, W. 2005, Fundamentals of Solar Astronomy

Bi, Y., Jiang, Y., Yang, J., et al. 2014, Astrophysical Journal, 790, 100

Blanco, S., Bocchialini, K., Costa, A., et al. 1999, Solar Physics, 186, 281

Blokland, J. W. S. & Keppens, R. 2011, Astronomy and Astrophysics, 532, A93

Bommier, V., Leroy, J. L., & Sahal-Brechot, S. 1986, Astrophysical Journal, 156, 90

Bona, C., Bona-Casas, C., & Terradas, J. 2009, Journal of Computational Physics, 228, 2266

Brandenburg, A. 2003, Computational aspects of astrophysical MHD and turbulence, ed. A. Ferriz-Mas & M. Núñez, 269

Brown, D. S. & Priest, E. R. 2001, Astronomy and Astrophysics, 367, 339

Dahlburg, R. B., Antiochos, S. K., & Klimchuk, J. A. 1998, Astrophysical Journal, 495, 485

de Bruyne, P. & Hood, A. W. 1993, Solar Physics, 147, 97

de Groof, A., Bastiaensen, C., Müller, D. A. N., Berghmans, D., & Poedts, S. 2005, Astronomy and Astrophysics, 443, 319

De Groof, A., Berghmans, D., van Driel-Gesztelyi, L., & Poedts, S. 2004, Astronomy and Astrophysics, 415, 1141

Demoulin, P. & Priest, E. R. 1993, Solar Physics, 144, 283

Díaz, A. J., Oliver, R., & Ballester, J. L. 2002, Astrophysical Journal, 580, 550

Díaz, A. J., Oliver, R., & Ballester, J. L. 2003, Astronomy and Astrophysics, 402, 781

Díaz, A. J., Oliver, R., & Ballester, J. L. 2010, Astrophysical Journal, 725, 1742

Díaz, A. J., Oliver, R., Erdélyi, R., & Ballester, J. L. 2001, Astronomy and Astrophysics, 379, 1083

Dodson, H. W. 1949, Astrophysical Journal, 110, 382

Dodson, H. W. & Hedeman, E. R. 1964, Moving Material Accompanying the Flare of 1959 July $16^d21^h14^m$ UT, Vol. 50, 15

Dymova, M. V. & Ruderman, M. S. 2005, Solar Physics, 229, 79

Elsden, T. & Wright, A. N. 2017, Journal of Geophysical Research (Space Physics), 122, 3247

Engvold, O. 2015, Astrophysics and Space Science Library, Vol. 415, Description and Classification of Prominences, ed. J.-C. Vial & O. Engvold, 31

Eto, S., Isobe, H., Narukage, N., et al. 2002, Publications of the ASJ, 54, 481

Fiedler, R. A. S. & Hood, A. W. 1992, Solar Physics, 141, 75

Forteza, P., Oliver, R., Ballester, J. L., & Khodachenko, M. L. 2007, Astronomy and Astrophysics, 461, 731

Gilbert, H. R., Daou, A. G., Young, D., Tripathi, D., & Alexander, D. 2008, Astrophysical Journal, 685, 629

Goossens, M. 2003, An introduction to plasma astrophysics and magnetohydrodynamics, Vol. 294

Goossens, M., Andries, J., & Aschwanden, M. J. 2002, in ESA Special Publication, Vol. 506, Solar Variability: From Core to Outer Frontiers, ed. A. Wilson, 629–632

Goossens, M., Arregui, I., Ballester, J. L., & Wang, T. J. 2008, Astronomy and Astrophysics, 484, 851

Goossens, M., Hollweg, J. V., & Sakurai, T. 1992, Solar Physics, 138, 233

Goossens, M., Poedts, S., & Hermans, D. 1985, Solar Physics, 102, 51

Hale, G. E. 1908, Astrophysical Journal, 28, 315

Haugen, N. E. L. & Brandenburg, A. 2004, Physical Review E, 70, 026405

Hershaw, J., Foullon, C., Nakariakov, V. M., & Verwichte, E. 2011, Astronomy and Astrophysics, 531, A53

Hillier, A., Berger, T., Isobe, H., & Shibata, K. 2012a, Astrophysical Journal, 746, 120

Hillier, A., Isobe, H., Shibata, K., & Berger, T. 2012b, Astrophysical Journal, 756, 110

Hillier, A. & van Ballegooijen, A. 2013, Astrophysical Journal, 766, 126

Hirayama, T. 1971, Solar Physics, 17, 50

Hirayama, T. 1986, in NASA Conference Publication, Vol. 2442, NASA Conference Publication, 149–153

Hollweg, J. V. & Yang, G. 1988, Journal of Geophysics Research, 93, 5423

Hood, A. W. & Anzer, U. 1990, Solar Physics, 126, 117

Hyder, C. L. 1966, Zeitschrift fuer Astrophysik, 63, 78

Isobe, H. & Tripathi, D. 2006, Astronomy and Astrophysics, 449, L17

Isobe, H., Tripathi, D., Asai, A., & Jain, R. 2007, Solar Physics, 246, 89

Janssen, M. 1869, Astronomical register, 7, 131

Jing, J., Lee, J., Spirock, T. J., & Wang, H. 2006, Solar Physics, 236, 97

Jing, J., Lee, J., Spirock, T. J., et al. 2003, Astrophysical Journal, Letters, 584, L103

Joarder, P. S. & Roberts, B. 1992a, Astronomy and Astrophysics, 256, 264

Joarder, P. S. & Roberts, B. 1992b, Astronomy and Astrophysics, 261, 625

Joarder, P. S. & Roberts, B. 1993, Astronomy and Astrophysics, 277, 225

Jones, F. S. 1958, Journal of the RAS of Canada, 52, 149

Jordan, D. W. & Smith, P. 1987, Nonlinear Ordinary Differential Equations (2nd Ed.) (USA: Oxford University Press, Inc.)

Karpen, J. T. 2015, Astrophysics and Space Science Library, Vol. 415, Plasma Structure and Dynamics, ed. J.-C. Vial & O. Engvold, 237

Karpen, J. T., Antiochos, S. K., & Klimchuk, J. A. 2006, Astrophysical Journal, 637, 531

Khodachenko, M. L., Arber, T. D., Rucker, H. O., & Hanslmeier, A. 2004, Astronomy and Astrophysics, 422, 1073

Khodachenko, M. L., Rucker, H. O., Oliver, R., Arber, T. D., & Hanslmeier, A. 2006, Advances in Space Research, 37, 447

Khomenko, E. & Collados, M. 2012, Astrophysical Journal, 747, 87

Khomenko, E., Collados, M., Díaz, A., & Vitas, N. 2014a, Physics of Plasmas, 21, 092901

Khomenko, E., Díaz, A., de Vicente, A., Collados, M., & Luna, M. 2014b, Astronomy and Astrophysics, 565, A45

Kippenhahn, R. & Schlüter, A. 1957, Zeitschrift fuer Astrophysik, 43, 36

Kleczek, J. & Kuperus, M. 1969, Solar Physics, 6, 72

Knizhnik, K., Luna, M., Muglach, K., et al. 2014, in Nature of Prominences and their Role in Space Weather, ed. B. Schmieder, J.-M. Malherbe, & S. T. Wu, Vol. 300, 428–429

Kohutova, P. & Verwichte, E. 2017a, Astronomy and Astrophysics, 602, A23

Kohutova, P. & Verwichte, E. 2017b, Astronomy and Astrophysics, 606, A120

Kraśkiewicz, J., Murawski, K., Solov'ev, A., & Srivastava, A. K. 2016, Solar Physics, 291, 429

Kuperus, M. & Raadu, M. A. 1974, Astronomy and Astrophysics, 31, 189

Labrosse, N., Heinzel, P., Vial, J. C., et al. 2010, Space Science Reviews, 151, 243

Lee, M. A. & Roberts, B. 1986, Astrophysical Journal, 301, 430

Leroy, J. L., Bommier, V., & Sahal-Brechot, S. 1983, Solar Physics, 83, 135

Li, K., Schmieder, B., Malherbe, J. M., Roudier, T., & Wiik, J. E. 1998, Solar Physics, 183, 323

Li, T. & Zhang, J. 2012, Astrophysical Journal, Letters, 760, L10

Liakh, V., Luna, M., & Khomenko, E. 2020, Astronomy and Astrophysics, 637, A75

Lin, Y., Engvold, O., Rouppe van der Voort, L., Wiik, J. E., & Berger, T. E. 2005, Solar Physics, 226, 239

Lin, Y., Martin, S. F., & Engvold, O. 2008, in Astronomical Society of the Pacific Conference Series, Vol. 383, Subsurface and Atmospheric Influences on Solar Activity, ed. R. Howe, R. W. Komm, K. S. Balasubramaniam, & G. J. D. Petrie, 235

Liu, W., Ofman, L., Nitta, N. V., et al. 2012, Astrophysical Journal, 753, 52

Lockyer, J. N. 1868, Proceedings of the Royal Society of London Series I, 17, 91

Longbottom, A. W. & Hood, A. W. 1994, Solar Physics, 155, 267

Low, B. C. & Zhang, M. 2004, Astrophysical Journal, 609, 1098

Luna, M., Díaz, A. J., & Karpen, J. 2012a, Astrophysical Journal, 757, 98

Luna, M., Díaz, A. J., Oliver, R., Terradas, J., & Karpen, J. 2016a, Astronomy and Astrophysics, 593, A64

Luna, M. & Karpen, J. 2012, Astrophysical Journal, Letters, 750, L1

Luna, M., Karpen, J., Ballester, J. L., et al. 2018, Astrophysical Journal, 236, 35

Luna, M., Karpen, J. T., & DeVore, C. R. 2012b, Astrophysical Journal, 746, 30

Luna, M., Knizhnik, K., Muglach, K., et al. 2014, Astrophysical Journal, 785, 79

Luna, M., Terradas, J., Khomenko, E., Collados, M., & de Vicente, A. 2016b, Astrophysical Journal, 817, 157

Lyot. 1930, Bulletin Astronomique, 6, 305

Lyot, B. 1939, Monthly Notices of the RAS, 99, 538

Mackay, D. H. & Galsgaard, K. 2001, Solar Physics, 198, 289

Mackay, D. H., Karpen, J. T., Ballester, J. L., Schmieder, B., & Aulanier, G. 2010, Space Science Reviews, 151, 333

Malherbe, J. M. & Priest, E. R. 1983, Astronomy and Astrophysics, 123, 80

Martínez-Gómez, D., Oliver, R., Khomenko, E., & Collados, M. 2020, Astronomy and Astrophysics, 634, A36

Mazumder, R., Pant, V., Luna, M., & Banerjee, D. 2020, Astronomy and Astrophysics, 633, A12

Menzel, D. H. & Evans, J. W. 1953, Convegno Volta. Rome: Academia Lincei, 11, 119

Müller, D. A. N., Peter, H., & Hansteen, V. H. 2004, Astronomy and Astrophysics, 424, 289

Newton, H. W. 1935, Monthly Notices of the RAS, 95, 650

Ohman, Y. 1953, The Observatory, 73, 203

Okamoto, T. J., Antolin, P., De Pontieu, B., et al. 2015, Astrophysical Journal, 809, 71

Okamoto, T. J., Nakai, H., Keiyama, A., et al. 2004, Astrophysical Journal, 608, 1124

Okamoto, T. J., Tsuneta, S., Berger, T. E., et al. 2007, Science, 318, 1577

Oliver, R. 1999, in ESA Special Publication, Vol. 9, Magnetic Fields and Solar Processes, ed. A. Wilson & et al., 425

Oliver, R. 2009, Space Science Reviews, 149, 175

Oliver, R. & Ballester, J. L. 1995, Astrophysical Journal, 448, 444

Oliver, R., Ballester, J. L., Hood, A. W., & Priest, E. R. 1992, Astrophysical Journal, 400, 369

Oliver, R., Ballester, J. L., Hood, A. W., & Priest, E. R. 1993, Astrophysical Journal, 409, 809

Oliver, R., Soler, R., Terradas, J., & Zaqarashvili, T. V. 2016, Astrophysical Journal, 818, 128

Oliver, R., Soler, R., Terradas, J., Zaqarashvili, T. V., & Khodachenko, M. L. 2014, Astrophysical Journal, 784, 21

Pant, V., Srivastava, A. K., Banerjee, D., et al. 2015, Research in Astronomy and Astrophysics, 15, 1713

Parenti, S. 2014, Living Reviews in Solar Physics, 11, 1

Parenti, S. 2015, Astrophysics and Space Science Library, Vol. 415, Spectral Diagnostics of Cool Prominence and PCTR Optically Thin Plasmas, ed. J.-C. Vial & O. Engvold, 61

Parenti, S., Lemaire, P., & Vial, J. C. 2005, Astronomy and Astrophysics, 443, 685

Parker, E. N. 1979, Cosmical magnetic fields. Their origin and their activity (Clarendon Press)

Petrie, G. J. D., Blokland, J. W. S., & Keppens, R. 2007, Astrophysical Journal, 665, 830

Pettit, E. 1932, Astrophysical Journal, 76, 9

Piantschitsch, I., Terradas, J., & Temmer, M. 2020, Astronomy and Astrophysics, 641, A21

Pintér, B., Jain, R., Tripathi, D., & Isobe, H. 2008, Astrophysical Journal, 680, 1560

Popescu Braileanu, B., Lukin, V. S., Khomenko, E., & de Vicente, Á. 2021a, Astronomy and Astrophysics, 646, A93

Popescu Braileanu, B., Lukin, V. S., Khomenko, E., & de Vicente, A. 2021b, arXiv e-prints, arXiv:2101.12731

Priest, E. 2014, Magnetohydrodynamics of the Sun

Priest, E. R. 1989, Dynamics and structure of quiescent solar prominences, Vol. 150

Priest, E. R., Bungey, T. N., & Titov, V. S. 1997, Geophysical and Astrophysical Fluid Dynamics, 84, 127

Priest, E. R., Lonie, D. P., & Titov, V. S. 1996, Journal of Plasma Physics, 56, 507

Rae, I. C. & Roberts, B. 1981, Geophysical and Astrophysical Fluid Dynamics, 18, 197

Ramsey, H. E. & Smith, S. F. 1966, Astronomical Journal, 71, 197

Roberts, B. 2019, MHD Waves in the Solar Atmosphere (Cambridge University Press)

Roe, P. L. 1985, in Large-Scale Computations in Fluid Mechanics, 163–193

Ruderman, M. S. & Luna, M. 2016, Astronomy and Astrophysics, 591, A131

Ruderman, M. S. & Roberts, B. 2002, Astrophysical Journal, 577, 475

Sakurai, T., Goossens, M., & Hollweg, J. V. 1991, Solar Physics, 133, 227

Schnack, D. D. 2009, Lectures in Magnetohydrodynamics

Schrijver, C. J. 2001, Solar Physics, 198, 325

Schutgens, N. A. J. & Tóth, G. 1999, Astronomy and Astrophysics, 345, 1038

Secchi, A. 1875, Le Soleil

Sedláček, Z. 1971, Journal of Plasma Physics, 5, 239

Shen, Y., Ichimoto, K., Ishii, T. T., et al. 2014a, Astrophysical Journal, 786, 151

Shen, Y., Liu, Y. D., Chen, P. F., & Ichimoto, K. 2014b, Astrophysical Journal, 795, 130

Soler, R., Arregui, I., Oliver, R., & Ballester, J. L. 2010, Astrophysical Journal, 722, 1778

Soler, R., Oliver, R., & Ballester, J. L. 2007, Astronomy and Astrophysics, 471, 1023

Soler, R., Oliver, R., & Ballester, J. L. 2008, Astrophysical Journal, 684, 725

Soler, R., Oliver, R., & Ballester, J. L. 2009a, Astrophysical Journal, 707, 662

Soler, R., Oliver, R., & Ballester, J. L. 2011, Astrophysical Journal, 726, 102

Soler, R., Oliver, R., Ballester, J. L., & Goossens, M. 2009b, Astrophysical Journal, Letters, 695, L166

Soler, R. & Terradas, J. 2015, Astrophysical Journal, 803, 43

Stellmacher, G., Wiehr, E., & Dammasch, I. E. 2003, Solar Physics, 217, 133

Strogatz, S. 2018, Nonlinear Dynamics and Chaos: With Applications to Physics, Biology, Chemistry, and Engineering (CRC Press)

Tandberg-Hanssen, E. 1995, The nature of solar prominences, Vol. 199

Terradas, J., Arregui, I., Oliver, R., et al. 2008a, Astrophysical Journal, 679, 1611

Terradas, J., Luna, M., Soler, R., Carbonell, M., & Ballester, J. L. 2021, in preparation, Astronomy and Astrophysics

Terradas, J., Oliver, R., & Ballester, J. L. 2001, Astronomy and Astrophysics, 378, 635

Terradas, J., Oliver, R., & Ballester, J. L. 2004, Astrophysical Journal, 614, 435

Terradas, J., Oliver, R., Ballester, J. L., & Keppens, R. 2008b, Astrophysical Journal, 675, 875

Terradas, J., Soler, R., Díaz, A. J., Oliver, R., & Ballester, J. L. 2013, Astrophysical Journal, 778, 49

Terradas, J., Soler, R., Luna, M., Oliver, R., & Ballester, J. L. 2015a, Astrophysical Journal, 799, 94

Terradas, J., Soler, R., Luna, M., et al. 2016, Astrophysical Journal, 820, 125

Terradas, J., Soler, R., Oliver, R., & Ballester, J. L. 2015b, Astrophysical Journal, Letters, 802, L28

Titov, V. S. & Démoulin, P. 1999, Astronomy and Astrophysics, 351, 707

Tripathi, D., Isobe, H., & Jain, R. 2009, Space Science Reviews, 149, 283

Tsubaki, T., Ohnishi, Y., & Suematsu, Y. 1987, Publications of the ASJ, 39, 179

Uchida, Y. 1968, Solar Physics, 4, 30

van Tend, W. & Kuperus, M. 1978, Solar Physics, 59, 115

Vial, J.-C. 2015, Historical Background and Introduction, ed. J.-C. Vial & O. Engvold, Vol. 415, 1

Vrsnak, B. 1984, Solar Physics, 94, 289

Vrsnak, B., Ruzdjak, V., Brajsa, R., & Zloch, F. 1990, Solar Physics, 127, 119

Vršnak, B., Veronig, A. M., Thalmann, J. K., & Žic, T. 2007, Astronomy and Astrophysics, 471, 295

Wang, S.-H. 1994, Nonlinear Analysis: Theory, Methods & Applications, 22, 1475

Wang, Y., Cao, H., Chen, J., et al. 2010, Astrophysical Journal, 717, 973

Wiggins, S. 2003, Introduction to Applied Nonlinear Dynamical Systems and Chaos (Springer-Verlag New York)

Wolfram Research, I. 2020, Mathematica, Version 12.1, champaign, IL, 2020

Wright, A. N. & Elsden, T. 2016, Astrophysical Journal, 833, 230

Wu, S. T., Bao, J. J., An, C. H., & Tandberg-Hanssen, E. 1990, Solar Physics, 125, 277

Xia, C., Chen, P. F., Keppens, R., & van Marle, A. J. 2011, Astrophysical Journal, 737, 27

Xue, Z. K., Yan, X. L., Qu, Z. Q., & Zhao, L. 2014, in Astronomical Society of the Pacific Conference Series, Vol. 489, Solar Polarization 7, ed. K. N. Nagendra, J. O. Stenflo, Z. Q. Qu, & M. Sampoorna, 53

Zhang, L. Y., Fang, C., & Chen, P. F. 2019, Astrophysical Journal, 884, 74

Zhang, Q. M., Chen, P. F., Xia, C., & Keppens, R. 2012, Astronomy and Astrophysics, 542, A52

Zhang, Q. M., Chen, P. F., Xia, C., Keppens, R., & Ji, H. S. 2013, Astronomy and Astrophysics, 554, A124

Zhang, Q. M., Guo, J. H., Tam, K. V., & Xu, A. A. 2020, Astronomy and Astrophysics, 635, A132

Zhang, Q. M., Li, T., Zheng, R. S., Su, Y. N., & Ji, H. S. 2017, Astrophysical Journal, 842, 27

Zhou, Y.-H., Chen, P.-F., Zhang, Q.-M., & Fang, C. 2014, Research in Astronomy and Astrophysics, 14, 581

Zhou, Y.-H., Xia, C., Keppens, R., Fang, C., & Chen, P. F. 2018, Astrophysical Journal, 856, 179

Zirin, H. 1998, The Astrophysics of the Sun

Zirin, H. & Severny, A. 1961, The Observatory, 81, 155

Zirker, J. B., Engvold, O., & Martin, S. F. 1998, Nature, 396, 440